Determination of the magnetic octupole moment of ^{173}Yb and a design towards laser - double resonance methods in an MR - ToF device

Master's Thesis, 20.6.2020

Author:

SONJA KUJANPÄÄ

Supervisor:

RUBEN DE GROOTE

UNIVERSITY OF JYVÄSKYLÄ
DEPARTMENT OF PHYSICS

© 2020 Sonja Kujanpää
Julkaisu on tekijänoikeussäännösten alainen. Teosta voi lukea ja tulostaa henkilökohtaista käyttöä varten. Käyttö kaupallisiin tarkoituksiin on kielletty.
This publication is copyrighted. You may download, display and print it for Your own personal use. Commercial use is prohibited.

Abstract

Kujanpää, Sonja

Determination of the magnetic octupole moment of ^{173}Yb and a design towards laser-double resonance methods in an MR-ToF device

Master's thesis

Department of Physics, University of Jyväskylä, 2020, 77 pages.

This thesis consists of two parts.

In the first part, the magnetic octupole moment of stable ytterbium was determined using collinear laser spectroscopy (CLS) on a fast atomic beam in the Ion-Guide Isotope Separator On-Line (IGISOL) facility at Jyväskylä. The hyperfine constants of the metastable state in ^{173}Yb were measured using three different dipole transitions. From the resulting hyperfine spectra, can these constants A, B, and C for dipole, quadrupole, and octupole, respectively, be extracted. The corresponding nuclear moments μ, Q, and Ω are determined by combining these hyperfine constants with nuclear theory calculations. This measurement was performed to validate a previously observed abnormally large octupole splitting. From our measurement, the hyperfine octupole constant was determined to be $C = 0.02(6)$ MHz and the corresponding magnetic octupole moment $\Omega = -1.3(38)\ \mu_N$ b. These values are in significant disagreement with the previous experiment, but agree with the single-particle shell model estimate within the error bars. As C was zero within our precision, a future measurement using a higher-precision method, e.g.laser-radiofrequency double-resonance method (LRDR), is needed.

The second part of this thesis was done at CERN, in the Multi Ion Reflection Apparatus for CLS (MIRACLS) experiment located in the Isotope Separator On-Line Device (ISOLDE) facility. MIRACLS uses a Multi Reflection Time-of-Flight (MR-ToF) ion trap to extend the laser-ion interaction time. Using this method, the population of the hyperfine state of interest can be pumped out unintentionally, leading to less fluorescence. One way to overcome this could be to combine LRDR with MIRACLS: applying an RF field may repopulate that state, which increases fluorescence and boosts signal. A new design for the MR-ToF drift tube with an RF electrode was devised. A preliminary test was performed with a simple RF loop and no drift tube alterations. This test showed no enhancement due to the applied RF signal. A future design with a coaxial geometry is planned but not yet tested.

Keywords: collinear laser spectroscopy, ytterbium, magnetic octupole moment, IGISOL, laser-radiofrequency double-resonance, multi reflection time-of-flight, MR-ToF, CERN, ISOLDE, MIRACLS

Tiivistelmä

Kujanpää, Sonja

^{173}Yb:n magneettisen oktupolimomentin määritys ja laserkaksoisresonanssimenetelmän alustava suunnittelu MR-ToF -laitteeseen

Pro gradu -tutkielma

Fysiikan laitos, Jyväskylän yliopisto, 2020, 77 sivua.

Tämä pro gradu -tutkielma koostuu kahdesta osasta.

Ensimmäisessä osassa stabiilin ytterbiumin magneettinen oktupolimomentti määritetään kollineaarista laserspektroskopiaa (CLS) ja nopeaa atomisuihkua käyttäen. Mittaus suoritetaan IGISOL-laitteistolla (Ion-Guide Isotope Separator On-Line) Jyväskylän Yliopiston kiihdytinlaboratoriossa. ^{173}Yb:n metastabiilin tilan ylihienokertoimet mitataan käyttäen kolmea erilaista optista dipolisiirtymää. Mitatusta ylihienospektristä määritetään dipoli-, kvadrupoli- ja oktupolikertoimet A, B ja C, joista saadaan vastaavat ytimen momentit μ, Q ja Ω ydinteorian avulla. Tällä mittauksella pyritään todentamaan aikaisemmin havaittu epänormaalin suuri oktupolijakautuminen. Nyt tulokseksi saadaan ylihienolle oktupolikertoimelle $C = 0.02(6)$ MHz ja oktupolimomentille $\Omega = -1.3(38)$ μ_N b. Nämä arvot eroavat huomattavasti edellisestä mittauksesta mutta ovat virheiden rajoissa yhdenpitäviä yksihiukkasmallin arvion kanssa. Koska nyt C vastaa virherajoineen nollaa, tulevaisuudessa mittaus on toistettava tarkemmalla menetelmällä, kuten laser-radiotaajuuskaksoisresonanssilla (LRDR).

Tutkielman toinen osa tehdään CERN:issä ISOLDE:lla (Isotope Separator On-Line DEvice), jossa kehitetään moniheijastavan lentoaikamassaspektrometrin (MR-ToF) ja CLS:an yhdistävää Multi Ion Reflection Apparatus for CLS (MIRACLS) -laitteistoa. MIRACLS käyttää MR-ToF:ia ioniloukkuna laserin ja ionien välisen vuorovaikutusajan pidentämiseksi. Tästä aiheutuu populaation pumppautuminen pois kiinnostuksen kohteena olevalta ylihienotilalta, jolloin havaittu fluoresenssi vähenee. Ratkaisuna on yhdistää LRDR ja MIRACLS: radiotaajuuden (RF) avulla ajetaan siirtymiä, jotka täyttävät vajaan tilan uudelleen johtaen fluoresenssin ja signaalin palautumiseen. Tätä varten MR-ToF-laitteeseen suunnitellaan uusi keskielektrodi RF-elektrodin kera. Alustava koe tehtiin yksinkertaisella RF-silmukalla ilman muita muutoksia mutta siinä ei havaittu RF-signaalista johtuvaa parannusta. Seuraavaksi suunniteltiin koaksiaalista keskielektrodia mutta sitä ei kyetty kokeilemaan käytännössä.

Avainsanat: kollineaarinen laserspekroskopia, ytterbium, magneettinen oktupolimomentti, IGISOL, laser-radiotaajuuskaksoisresonanssi, moniheijastava lentoaikamassaspektrometri, MR-ToF, CERN, ISOLDE, MIRACLS

Preface

Firstly, I would like to express my thanks to my supervisor Ruben de Groote for his enthusiasm for this project, support, encouragement, and patience. It has been an educational experience, and I feel I have learned many new things, even my Python proficiency has advanced from non-existent to purely atrocious.

Secondly, I would like to express my gratitude to Stephan Malbrunot-Ettenauer for allowing me to continue working with the MIRACLS at ISOLDE-CERN regarding my thesis, as well all the team members - special thanks to Simon Sels for his invaluable help, optimism and efforts during the RF excitation tests and Varvara Lagaki for the much-appreciated help as well. Thanks also for Mark Bissell for sharing his knowledge and letting us once again borrow some COLLAPS equipment. Moreover, I want to thank the Faculty of Mathematics and Science of the University of Jyväskylä for awarding me the travel grant to go to CERN and complete a part of my thesis there.

I offer thanks also to Iain Moore and Paul Greenlees, without whose reference letters I sure would have not made it to the CERN Summer Student Programme 2019, which then lured me into laser spectroscopy and the chosen subject of this thesis (whether for good or for bad, I'll leave that to the reader). I am also grateful for Mikael Reponen for his help with the Finnish translation, which now turned out less badly. Thanks to Henna Joukainen for the insightful discussions, company, and constructive comments during these past five years. Thanks also to all my other friends, and family who supported me during my studies, and for my cat Viiru for always ignoring me when I came home to visit and then acting as nothing had happened.

Additionally, I acknowledge COVID-19 for making the long-awaited completion of this thesis possible as sometimes being self-quarantined in your house is all that is needed, and also unacknowledge it for ruining the other half of my MR-ToF tests. I am also grateful for the spell-check function of Microsoft Word, without whom the word 'frequency' would be misspelt differently exactly 93 times.

Kankaanpää, June 2020

Sonja Kujanpää

Contents

1 Introduction

Since the landmark experiments towards the comprehension of the atomic and nuclear structure were done, starting from the discovery of radioactivity by Henri Becquerel in 1896, the discovery of electron by Joseph Thomson in 1897 and the discovery of the atomic nucleus by observing the deflection of the alpha particles from gold foil by Ernest Rutherford, Hans Geiger and Ernest Marsden in 1911, understanding the exact structure of the nucleus has been of interest for many physicists. In 1913, just two years after the discovery of the nucleus, the first atomic model was built by Niels Bohr based on Planck's theory of quantization of energy, which then gave rise to the atomic shell model in 1949. Early works focused on studying stable or long-lived isotopes and resulted in enormous amounts of experimental data - leading to the development of the nuclear shell model to interpret the underlying nuclear structure. From the experimental data, it was noted that nuclei with a certain proton (Z) and/or neutron (N) number appeared more stable than others. These numbers were named the magic numbers (2, 8, 20, 28, 50, 82, and 126) and they define the number of nucleons that completely fill each shell. [1]

With the construction and development of modern radioactive ion beam (RIB) facilities, such as Ion-Guide Separator On-Line (IGISOL) at Jyväskylä and the Isotope Separator On-Line DEvice (ISOLDE) at CERN, it became possible to study short-lived and exotic radionuclides far from stability. This has led to the discovery of several new nuclear structure phenomena, some of which challenge the classical shell model picture, such as the disappearance and emergence of new shell closures [1].

To study the fundamental nuclear properties, one must gather information about the nucleus. Many methods have been invented over the years. This thesis deals with methods that investigate the hyperfine structure (HFS) of atoms or ions, which consists of tiny splittings and changes in the atomic energy levels due to nuclear electromagnetic properties. The invention of the laser in 1960 [2] and the subsequent laser spectroscopy techniques enabled the high resolution needed for examining these effects. The earliest experiment using spectroscopy based on the combination of fast ionic beams and lasers was done in 1975 by H. Andra [3]. One of the techniques that is nowadays routinely used in RIB-facilities is collinear laser spectroscopy (CLS), which originated from the theoretical and experimental efforts of W. H. Wing [4] and S. Kaufman [5] in 1976. In CLS, the laser beam is overlapped with an atom or ion beam to reduce unwanted Doppler broadening of the observed lineshapes. By scanning the laser frequency in the rest frame of the atoms or ions, it can be tuned into the resonance frequency of the electronic transition in the atomic shell. When the laser's frequency corresponds to the energy differences between the hyperfine levels, the atoms or ions will be excited. After being excited by the laser, the atoms or ions decay back to their corresponding ground-state, emitting fluorescence photons. These photons can be detected by a detection system, such as a

photomultiplier tube (PMT), placed perpendicularly to the laser/atom beam. By measuring the fluorescence counts as a function of the frequency, the hyperfine splitting and isotope shifts can be extracted. Since these properties arise from the interaction between the nucleus and its surrounding electron cloud, it is possible to gain information about the nuclear properties, such as the nuclear spin, the nuclear multipole moments, and the nuclear mean-square charge radius [1]. Some pioneering CLS experiments have been done at ISOLDE-CERN, where currently beamlines COLLAPS [6], CRIS [7], and MIRACLS [8] are in use, and e.g. at the collinear laser line at the IGISOL facility in Jyväskylä. Most of the measurements in this thesis, whose motivations are detailed in the following chapters, were done at the IGISOL, in addition to some work conducted at MIRACLS.

1.1 Motivation for ^{173}Yb magnetic octupole

The magnetic dipole moment μ and quadrupole moment Q have been measured in various different nuclei [9] from the atomic hyperfine structure, yet similar measurements for the next term in the multipolar expansion, the magnetic octupole constant C and the corresponding nuclear magnetic octupole moment Ω, have not been conducted nearly as much. According to the current knowledge, the magnetic octupole splitting has been previously measured for only 18 elements, such as ^{45}Sc, ^{83}Kr, ^{151}Eu, and ^{201}Hg, all of which are summarized in table 1.

Due to the lack of experimental data, interpretation of these octupole moments has been very challenging, and so no meaningful progress in the corresponding nuclear theory has been made in the past 50 years. For the octupole moments measured, often no uncertainty for values of Ω is provided in the original works. Especially, good estimates for theoretical uncertainties of C and Ω are often lacking and in some cases, important effects like second-order hyperfine mixing are not fully considered. From the experimental point of view, recent years have been very promising: highly precise octupole moment measurements were done using optical spectroscopy with the D_2 line in ^{133}Cs in 2003 [10], and the most accurately determined octupole moment to date was measured in 2012 using a single trapped $^{137}Ba^+$ ion [11].

In 2013 yet another octupole measurement was done with atomic ^{173}Yb using the hyperfine intervals in the metastable $^3P_2^\circ$ state [12]. This measurement was particularly interesting, as a surprisingly large octupole splitting was observed compared to the magnitudes observed for other elements. This large splitting is intriguing for a couple of reasons: an effect this large would be measurable with currently used spectroscopic methods at RIB-facilities [13], and the value of Ω acquired by [12] is significantly larger than the estimated value from the single-particle shell model calculations. This hints that our current understanding of the nuclear electromagnetic moments could be insufficient and more theoretical explorations may need to be conducted.

Table 1: Summary of some magnetic octupole hyperfine parameters C and the corresponding magnetic octupole moments Ω. Uncertainties of the C and Ω are as quoted in the literature where available, and μ_N is the nuclear magneton and b is barn.

Isotope	Z	N	State	C [Hz]	$\Omega[\mu_N$ b]	Ref.
^{35}Cl	17	18	$^2P^\circ_{3/2}$	-6.95(1.2)	-0.0188	[a]
^{37}Cl	17	20	$^2P^\circ_{3/2}$	-5.41(1.2)	-0.0146	[a]
^{45}Sc	21	23	$^2D_{5/2}$	-250(100)	1.6(8)	[14]
^{51}V	23	27	$^4D_{3/2}$	-1660(140)	–	[15] [b]
	23	27	$^4D_{5/2}$	-270(80)	–	[15] [b]
^{69}Ga	31	38	$^2P^\circ_{3/2}$	84(6)	0.107(20)	[16]
^{71}Ga	31	40	$^2P^\circ_{3/2}$	115(7)	0.146(20)	[16]
^{79}Br	35	44	$^2P^\circ_{3/2}$	388(8)	0.116	[17]
^{81}Br	35	46	$^2P^\circ_{3/2}$	430(8)	0.129	[17]
^{83}Kr	36	47	$^3P^\circ_2$	-790(250	-0.18(6)	[18]
^{113}In	49	64	$^2P^\circ_{3/2}$	1728(45)	0.565(12)	[19]
^{115}In	49	66	$^2P^\circ_{3/2}$	1702(35)	0.574(15)	[19]
^{127}I	53	74	$^2P^\circ_{3/2}$	2450(370)	0.167	[20, 21]
^{131}Xe	54	77	$^3P^\circ_2$	728(105)	0.048(12)	[22]
^{133}Cs	55	78	$^2P^\circ_{3/2}$	560(70)	0.8(1)	[23]
^{137}Ba	56	81	$^2D_{3/2}$	36.546	0.05057(54)	[11]
^{137}Ba	56	81	$^2D_{5/2}$	-12.41(77)	0.0496(37)	[24]
^{151}Eu	63	88	$^{8,10}D^\circ_J$	[c]	–	[25]
^{153}Eu	63	90	$^{8,10}D^\circ_J$	[c]	–	[25]
^{155}Gd	64	91	$^3D^\circ_3$	-1500(500)	-1.6(6)	[26]
^{173}Yb	70	103	$^3P^\circ_2$	$540(20)\cdot10^3$	-34.4(21)	[12]
^{175}Lu	71	104		-617(57)	–	[27]
^{176}Lu	71	105		-1377(302)	–	[27]
^{177}Hf	72	105	$^3F_2$	170(30)	–	[28]
	72	105	$^3F_3$	230(90)	–	[28]
	72	105	$^3F_4$	500(190)	–	[28]
^{179}Hf	72	107	$^3F_2$	-410(50)	–	[28]
	72	107	$^3F_3$	-600(250)	–	[28]
	72	107	$^3F_4$	-1190(500)	–	[28]
^{197}Au	79	118	$^2D_{3/2}$	212(14)	0.0098(7)	[29]
	79	118	$^4F^\circ_{9/2}$	326(10)	0.130	[29]
^{201}Hg	80	121	$^3P^\circ_2$	-1840(90)	-0.130(13)	[30]
^{209}Bi	83	126	$^2P^\circ_{3/2}$	19300(500)	0.55(3)[d]	[31]
	83	126	$^4S^\circ_{3/2}$	16500(100)	0.43	[32]
^{207}Po	84	123	$^3P_2$	-12(1)	0.11(1)	[33, 34]

[a] J. H. Holloway, unpublished Ph.D. thesis, Dept. of Phys., MIT, 1956. Values taken from [17].
[b] Only significantly non-zero C-values listed.
[c] Average ratio of C-parameters provided: C(^{151}Eu)/C(^{153}Eu) = 0.87(6).
[d] Value and uncertainty obtained as the average of several theoretical methods.

It is important to note that any interpretation of the absolute values of Ω depends essentially on the correct estimations of the associated uncertainties, which originate from both the experimental measurements and atomic-theory calculations. These theoretical calculations are required since the effects under study are very small, and corrections for the mixing of the state of interest with other close-lying states must be considered precisely. Another reason is the fact that the extraction of Ω from a measurement of C requires a calculation of the electronic wavefunctions.

In this work, a new measurement is done to validate the results obtained in [12], using collinear laser spectroscopy at the IGISOL-facility. If a non-zero magnetic octupole constant C is obtained with this method, this will prepare the way for similar measurements using radioactive ytterbium isotopes in the future.

1.2 Motivation for the development of RF spectroscopy in an MR-ToF

While the most experimental methods currently used in the RIB-facilities provide measurements of the hyperfine splittings with a 1 – 10 MHz precision [13], there are more precise measurement techniques such as the laser-radiofrequency double resonance (LRDR) method. LRDR is the descendant of the molecular-beam magnetic-resonance (MBMR) method, introduced in 1938 [35].

Initially, MBMR was aimed at the determination of the nuclear spins and moments, but soon after it was adapted to measuring the atomic and molecular hyperfine structure (HFS) and nuclear g-factors. When tunable single-frequency lasers became available in the 1970s, they had a massive impact on the development of general spectroscopy and especially the MRBR method. The most important features in this new laser were its spectral sharpness, tunability, and efficiency in causing detectable fluorescence. An important application for this was to use it in a pump-probe configuration to replace inhomogeneous fields inside the traditional MBMR apparatus. With this arrangement, the standard MBMR apparatus could be replaced with a shorter and much more efficient LRDR setup. [36]

The LRDR method relies on the use of radiofrequency (RF) photons to repopulate the lower hyperfine structure level that was previously depleted by exciting an optical transition. This repopulation results in a resonant increase in observed fluorescence. The ongoing progress in the development of the higher precision methods and theoretical tools has much potential to evolve our understanding of the atomic nucleus and its properties. The aim of this work is to combine the RF excitations from the LRDR method with in-trap laser spectroscopy technique used in MIRACLS at ISOLDE-CERN. MIRACLS, short for Multi Ion Reflection Apparatus for Collinear Laser Spectroscopy, relies on the use of a Multi Reflection Time-of-Flight (MR-ToF) ion trap to increase the laser-ion interaction

time. LRDR has been done previously using a Paul trap [37] and a Penning trap [38], but there is no record of it been done in an MR-ToF device. Thus, this opens new exciting possibilities for high precision spectroscopy if successful.

For example, Penning traps have been used for high precision Zeeman spectroscopy, providing long observation times under almost perturbation-free conditions. Normally resolution can be limited by the finite observation times and line broadening caused by collisions between particles but with the use of this method these sources can be eliminated. [38]

At MIRACLS the greatest motivation at this time was to overcome the unintentional population depletion in their setup, which is caused by optical pumping. Here the population is pumped out of the hyperfine state of interest, which leads to less fluorescence. By introducing an RF field, this state could be repopulated, leading to an increase in the fluorescence and a boosted signal during the measurements. These RF excitations are already familiar from the LRDR method, where they are routinely used. The optical detection region in the MIRACLS setup is located above the MR-ToF device's central drift tube, so a new design for the drift tube was also needed to house the desired RF electrodes to produce the field, along with a control program, and a switch for the RF signal. An initial investigation of the mechanical design for this modified drift tube was performed during this thesis and is discussed in chapter 4.2.

2 Theoretical background

2.1 Nuclear perturbations arising from the atomic structure

Measurable perturbations of the atomic structure are caused by the non-zero nuclear spin, the nuclear multipole moments, the radial extent of the charge distribution, and the distribution of magnetism. The interactions giving rise to these perturbations will be described in the following chapters.

2.1.1 Nuclear ground-state properties from the atomic spectra

In the absence of external fields, an atom can be depicted as a compact charged nucleus and an electron cloud arranged in the central Coulomb field produced by the nucleus. If the electrons have resultant angular momentum, $J > 0$, and the nucleus has a nuclear spin, $I > 0$, further interactions happen between these two systems. [39]

These interactions can be expanded into a multipolar expansion, in which the magnetic dipole μ, electric quadrupole Q, magnetic octupole Ω, and so on, are nonzero. In an atomic nucleus with an atomic spin J, a nuclear spin I, and a total angular momentum $F = I + J$, spectroscopic information on the corresponding nuclear moments can be obtained roughly in three ways: by observing the transitions between the fine structure states, or the magnetic transitions which happen within the same atomic state, or in presence of an external magnetic field, between the magnetic substates labelled with the projection quantum numbers m_J or m_F of these levels [13].

Visual representation of these observable nuclear ground-state properties is given in figure 1. As it will be detailed more computationally in the following chapters, the magnetic dipole moment can be simply defined as torque experienced by a current loop where the magnetic moment is a vector perpendicular to the current loop as stated by the right-hand rule, the electric quadrupole moment describes the effective shape of the nuclear charge distribution (negative value for oblate, zero for spherical, and positive value for prolate shape), and the magnetic octupole could be described as a more complicated version of the magnetic dipole moment

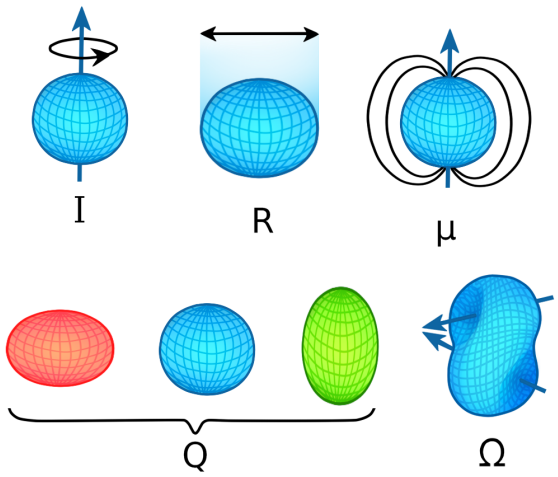

Figure 1: Illustration of the observable nuclear ground-state properties, which are the nuclear spin I, the nuclear mean-square charge radius R, the magnetic dipole moment μ, the electric quadrupole moment Q, and the magnetic octupole moment Ω.

where there are now two angled current loops instead of one, and the magnetic vectors are facing in- or outwards in the same general direction.

2.1.2 Fine and hyperfine structure

Relativistic effects lead to small splittings of the energy levels in the atom, called the fine structure. This effect arises when the total orbital momentum $\boldsymbol{L}$ and the spin angular momentum $\boldsymbol{S}$ of the electrons moving in the Coulomb field of a point-like nucleus couple to a new angular momentum (spin-orbit coupling) $\boldsymbol{J} = \boldsymbol{S} + \boldsymbol{L}$ [40]. Fine structure splittings are in the eV scale [13]. The coupling of the electron angular momentum $\hat{J}$ and nuclear angular momentum $\hat{I}$ results in a new angular momentum $\hat{F} = \hat{I} + \hat{J}$, from which occurs the splitting of a fine structure level to a hyperfine structure level.

The interaction between the nucleus and the surrounding electromagnetic fields is described by the perturbation Hamiltonian [41]

$$H = \sum_k T_e^{(k)} \otimes T_n^{(k)}, \tag{1}$$

where $T_n^{(k)}$ and $T_e^{(k)}$ are irreducible spherical tensors of rank k describing the electromagnetic properties of the nucleus and its electric surroundings, respectively. That is, $T_e^{(k)}$ operates in only electronic coordinates and its rank is defined by the interaction of the total angular momentum operator $\boldsymbol{J}$ of the same space. Similarly, $T_n^{(k)}$ operates only in the coordinates of the nucleons and the terms in the series in equation (1) are the scalar products of these two tensors, marked with $\otimes$, and thus invariant in the combined space. [39]

Consideration of the parity conservation of the strong and electromagnetic interactions dictate a general operator $T_{q=0}^{(k)}$, which consists of negative parity magnetic multipole operators and positive parity electric multipole operators. Thus, it follows that the nucleus can be described with a series of even-k electric (monopole, quadrupole, ...) and odd-k magnetic (dipole, octupole, ...) multipole moments up to order $k \leq 2I$. Laser spectroscopy techniques, theoretically sensitive to the entire multipole expansion, are typically limited to measuring moments of order $k \leq 2$. This stems from the rapid decrease in the size of the terms in the expansion compared to the experimental uncertainties. [13]

The atomic hyperfine structure (HFS) arises from the perturbation Hamiltonian in equation (1), where the electromagnetic tensor is derived from the field caused by the valence electrons, and the nuclear tensor from the multipole expansions of the nuclear moments.

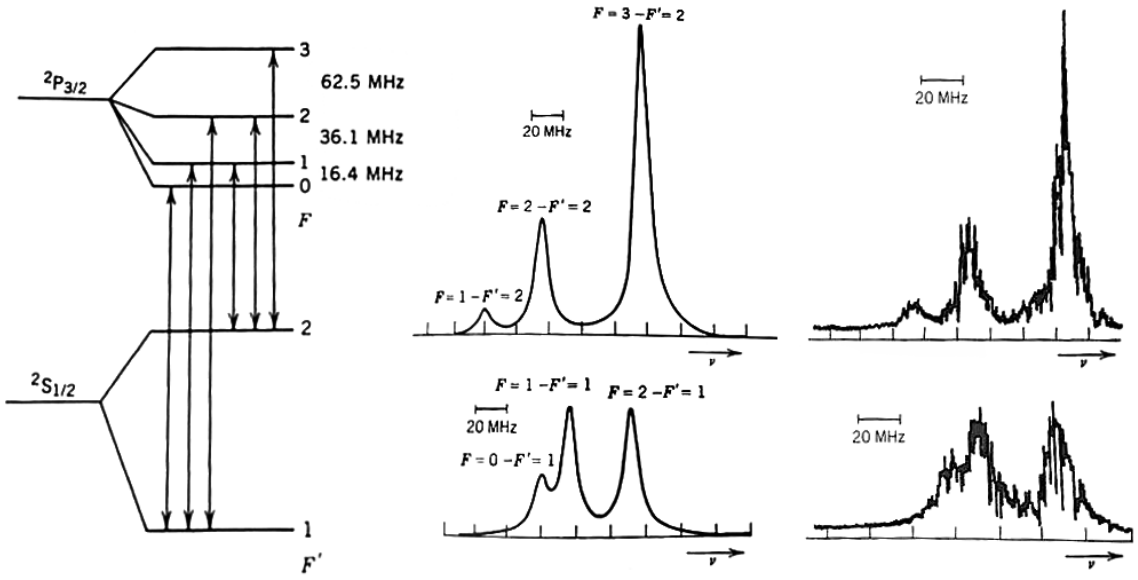

Figure 2: Hyperfine structure of sodium (measured with atomic-beam fluorescence spectroscopy), with hyperfine multiplets of $^2S_{1/2}$ and $^2P_{3/2}$ states and allowed $\Delta F = \pm 1, 0$ electric dipole transitions, is shown on the left side. When the frequency of the used laser is varied, a resonant absorption and re-emission occurs at frequencies that correspond to the energy difference between states $^2S_{1/2}$ and $^2P_{3/2}$ and resulting fluorescent radiation can be detected with a photomultiplier tube. In the middle, the calculated fluorescence spectrum is shown for these two sets of transitions originating from the $F' = 1$ and $F' = 2$ levels of the hyperfine multiplet. On the right is the actual measured spectrum. Figure edited from [1].

As the name suggests, HFS is smaller than the fine structure but observable in isotopes with a non-zero nuclear spin, as illustrated in figure 2. It is therefore usually treated as a perturbation to the electronic fine structure, with the magnetic and quadrupole terms having magnitudes of μeV [13]. In systems with small fine structure splittings, such as encountered in half-filled shells or Rydberg states, second-order perturbations may need to be considered like in [42]. When the splittings are comparable in magnitude, simultaneous diagonalization must be performed like in [43].

2.1.3 Spectroscopic notation for labelling the atomic states

Atomic states are typically labelled using a spectroscopic notation $\boldsymbol{n^{2S+1}L_J}$, where $\boldsymbol{n}$ is the principal quantum number (often omitted), $\boldsymbol{S}$ is the total spin quantum number, $\boldsymbol{L}$ refers to the orbital angular momentum quantum number $\boldsymbol{l}$ and is written as $\boldsymbol{S, P, D, F, \ldots}$ for $\boldsymbol{l} = 0, 1, 2, 3, \ldots$, and $\boldsymbol{j}$ is the total angular momentum quantum number. [1]

$\boldsymbol{I}$ is used to represent the total nuclear angular momentum (= nuclear spin) and $\boldsymbol{J}$ represents the total (= intrinsic + orbital) electronic angular momentum. When considering ideal hydrogenic atoms, the electron is moving in the nuclear Coulomb potential in the quantum states of well defined orbital angular momentum $\boldsymbol{L}$, where including the elec-

tronic spin gives a second label S. In principle, it should not matter whether the electronic states of an ideal atom are labelled using a set of quantum numbers $\boldsymbol{L}, m_L, S, m_S$ or a set of $\boldsymbol{L}, S, J, m_J$. Yet, the spin-orbit interaction which leads to the formation of the fine structure of the electronic levels, couples $\boldsymbol{L}$ and $\boldsymbol{S}$ in such a way that $\boldsymbol{m}_L$ and $\boldsymbol{m}_S$ are no longer well-defined and thus the coupling have to be used to identify the real states. The spin-orbit interaction can be explained simply by using a semiclassical picture in the reference frame of the electron, where the nucleus generates a current loop. This creates a magnetic field at the location of the electron, which interacts with the electrons' spin magnetic moment μ_S giving the spin-orbit contribution to the fine structure. In figure 3 the energy levels of sodium are illustrated with and without the spin-orbit interaction. [1]

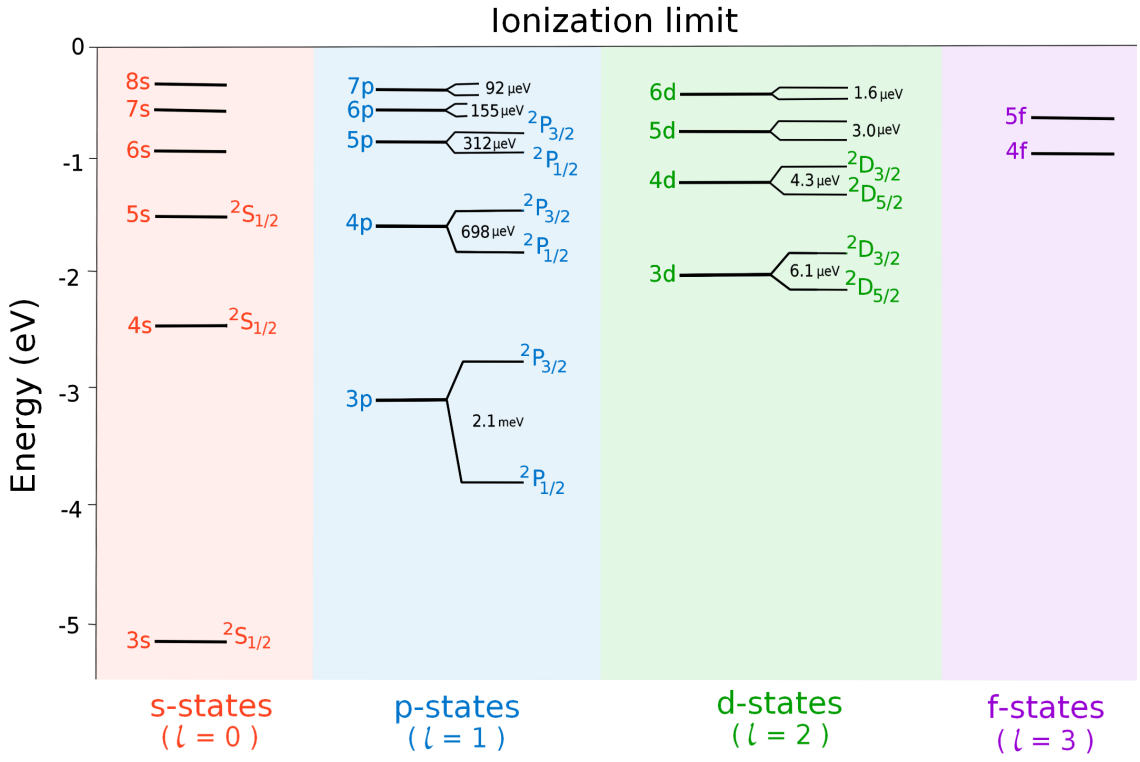

Figure 3: Pictured here are the energy levels in atomic sodium. On the left side of each level is the electronic configuration, and on the right side is the spectroscopic notation for the atomic state. The fine structure doublets are labelled with total angular momentum $j = l \pm 1/2$, the relative spacings between the doublets are only consistent for a particular l value i.e. the P- and D-state splittings are not in scale but the decrease of splittings within the P-states is in scale. Figure redrawn from [1].

2.1.4 Hyperfine structure shifts due to the nuclear multipole moments

Plenty of information about the magnetic dipole moment μ and the electric quadrupole moment Q exists for several atomic nuclei [9], but only a little is known about the next higher moments, i.e. the magnetic octupole Ω and the electric hexadecapole moments. All of these nuclear moments can be extracted from the atomic HFS measurements and they are independent of the used nuclear model. This chapter will focus on the nuclear multipole expansions up to the magnetic octupole moment, as it was of particular interest for this work.

The (hyper)fine structure of the atoms can be studied via various laser spectroscopy methods. An atom/ion is optically excited from a lower level $|IJ, Fm_F\rangle$ to an upper level $|I'J', F'm'_{F'}\rangle$ if the frequency of the laser corresponds to the energy difference of the transition between the HFS levels. The dipole selection rules dictate that only specific transitions between the hyperfine states are allowed:

$$\Delta F = 0, \pm 1 \qquad \text{and} \tag{2}$$

$$F = 0 \quad \nrightarrow \quad F' = 0, \tag{3}$$

where in equation (2) is the allowed transition while in equation (3) the transition is forbidden [1]. As every atomic state has hyperfine structure, with laser spectroscopic measurements the hyperfine structure constants A, B (and, potentially also C) are measured for two states at the same time. These different hyperfine constants will later be labelled as lower and upper hyperfine constants referring to the upper and lower states, i.e. $A_\mathrm{l}, B_\mathrm{l}, C_\mathrm{l}$ for the lower state and $A_\mathrm{u}, B_\mathrm{u}, C_\mathrm{u}$ for the upper state. These two states can be seen e.g. from figure 3.

When the terms arising from the interaction with the multipole moments are considered, the first-order expectation for the energy shift of each atomic hyperfine level with respect to the unperturbed fine structure level can be described by

$$\Delta E^{(1)}_\mathrm{HFS} = \sum_k M_k(I, J, F) \left\langle II \right| T^{(n)}_k \left| II \right\rangle \left\langle JJ \right| T^{(e)}_k \left| JJ \right\rangle, \tag{4}$$

where I, J, and F are the quantum numbers associated with the corresponding operators $\hat{I}$, $\hat{J}$, and $\hat{F}$, while M_k gives information about the relative alignment of the atomic and nuclear momenta and is defined as

$$M_k(I, J, F) = (-1)^{I+J+F} \frac{\begin{Bmatrix} I & J & F \\ J & I & k \end{Bmatrix}}{\begin{pmatrix} I & k & I \\ -I & 0 & I \end{pmatrix} \begin{pmatrix} J & k & J \\ -J & 0 & J \end{pmatrix}}, \tag{5}$$

where the factor in the curly brackets is the Wigner 6-j symbol. The different energy eigenvalues associated with the total angular momenta of the states are described by the quantum number $F = |I - J| \leq F \leq I + J$. Expanding the equation (4) to the octupole term ($k = 3$), it can be written as

$$\Delta E^{(1)}_{\mathrm{HFS}} = \frac{AK}{2} + \frac{3B}{4}\frac{K(K+1) - I(I+1)J(J+1)}{(2I(2I-1)J(2J-1)} \tag{6}$$

$$+ \frac{5C}{4}\frac{K^3 + 4K^2 + \frac{4}{5}K(-3I(I+1)J(J+1) + I(I+1) + J(J+1) + 3) - 4I(I+1)J(J+1)}{I(I-1)(2I-1)J(J-1)(2J-1)},$$

where the Wigner 3-j and Wigner 6-j symbols were fully written out in terms of the I, J and F, and A, B, and C are the hyperfine constants for dipole, quadrupole, and octupole, respectively, and $K = F(F+1) - I(I+1) - J(J+1)$. The hyperfine constants were defined in the following way:

$$A = \frac{1}{IJ}\left\langle II\right| T^{(n)}_2 \left|II\right\rangle \left\langle JJ\right| T^{(e)}_1 \left|JJ\right\rangle = \frac{\mu_I}{IJ}\left\langle JJ\right| T^{(e)}_1 \left|JJ\right\rangle, \tag{7}$$

$$B = 4\left\langle II\right| T^{(n)}_2 \left|II\right\rangle \left\langle JJ\right| T^{(e)}_2 \left|JJ\right\rangle = 2eQ\left\langle JJ\right| T^{(e)}_2 \left|JJ\right\rangle, \tag{8}$$

$$C = \left\langle II\right| T^{(n)}_3 \left|II\right\rangle \left\langle JJ\right| T^{(e)}_3 \left|JJ\right\rangle = -\Omega\left\langle JJ\right| T^{(e)}_3 \left|JJ\right\rangle, \tag{9}$$

where in the equation (8) e is the elementary charge and the negative sign for Ω in the equation (9) is selected to assure that μ and Ω are of the same sign in most cases. [39]

The nuclear magnetic dipole moment μ is then given by the relation

$$\mu = g_I \mu_N I, \tag{10}$$

where g_I is the nuclear g-factor and μ_N the nuclear magneton. Nuclei have smaller magnetic moments than electrons, as can be seen from how μ_N is related to the Bohr magneton μ_B:

$$\mu_N = \mu_B \frac{m_e}{m_p}, \tag{11}$$

where m_e is the mass of an electron and m_p mass of a proton. [40]

The absolute values of the magnetic dipole and electric quadrupole moments can be obtained from a measurement, where a precise calculation of the relevant electromagnetic fields is conducted. However, a way more prevalent practise is to instead extract the ratio of the nuclear isotopes from a pair of different isotopes of the same element using approximated relationships:

$$\frac{A}{A'} \simeq \frac{\mu}{\mu'}\frac{I'}{I} \quad \text{and} \quad \frac{B}{B'} \simeq \frac{Q}{Q'}, \tag{12}$$

where A', μ', I', B', and Q' are the properties related to the reference isotope. [13]

Thus, knowing the moments of a reference isotope, measured using another method, the moment of interest can be extracted. Note, however, that this procedure represents an approximation; the differential changes in the nuclear charge and magnetism, while small, do occur. For magnetic moments, these changes are referred to as anomalies. For an infinitely small nucleus, equation (12) is valid. In real and especially heavier nuclei, the finite nuclear extent and relativistic effects affect the electronic wavefunctions and give rise to corrections that must be considered. These effects are the Breit-Rosenthal (BR) effect [44] rising from the finite spatial distribution of the nuclear charge, and Bohr-Weisskopf (BW) effect [45] from the distribution of nuclear magnetism in the nucleus. These have only a small contribution so they are often accounted for by

$$A = A_{\mathrm{POINT}}(1+\epsilon_{\mathrm{BW}})(1+\epsilon_{\mathrm{BR}}), \tag{13}$$

where A_{POINT} is the hyperfine constant A for a theoretical point-like nucleus [13]. For quadrupole moments, no experimental reports of hyperfine anomalies exist [46].

So as it can be seen, the extraction of the nuclear moments μ, Q, and Ω from an HFS measurement requires either the use of a reference nucleus, where the moment was determined in some other way, or the use of atomic calculations to precisely evaluate the electronic matrix elements. For all moments beyond the quadrupole term ($k > 2$), only the latter option is presently applicable.

Additionally, the extraction of the hyperfine constants from the experimental spectra requires the evaluation of the second-order shifts due to the mixing of the close-lying states. This second-order approximation for the shift of a hyperfine level F due to mixing with another state that has electronic angular momentum J is defined as

$$\begin{aligned}\Delta E^{(2)}_{\mathrm{HFS}} \;=\; & \sum_{J'} \frac{1}{E_J - E_{J'}} \sum_{k_1,k_2} \begin{Bmatrix} F & J & I \\ k_1 & I & J' \end{Bmatrix} \begin{Bmatrix} F & J & I \\ k_2 & I & J' \end{Bmatrix} \\ \times\; \langle I||T^{(n)}_{k_1}||I\rangle\; & \langle I||T^{(n)}_{k_2}||I\rangle \;\times\; \langle J'||T^{(e)}_{k_1}||J\rangle\; \langle J'||T^{(e)}_{k_2}||J\rangle,\end{aligned} \tag{14}$$

where E_J is the energy of an atomic state having an angular momentum J, $k_1 = 1$ for magnetic dipole transition M1, and $k_1 = 2$ for electric quadrupole transition E2. Note that the reduced matrix elements (marked with $||$) can be related to the full matrix elements (marked with $|$) via the relation

$$\langle JJ|T_k|JJ\rangle = \begin{pmatrix} J & k & J \\ -J & 0 & J \end{pmatrix} \langle I||T_k||I\rangle. \tag{15}$$

When the expressions of equation (14) are restricted to M1-M1, M1-E2 and E2-E2 interactions, it can be expressed as follows:

$$\Delta E^{(2)}_{\mathrm{HFS}} = E^{M1-M1}_{\mathrm{HFS}} + E^{M1-E2}_{\mathrm{HFS}} + E^{E2-E2}_{\mathrm{HFS}} \tag{16}$$

$$= \sum_{J'} \left| \begin{Bmatrix} F & J & I \\ 1 & I & J' \end{Bmatrix} \right|^2 \eta + \begin{Bmatrix} F & J & I \\ 1 & I & J' \end{Bmatrix} \begin{Bmatrix} F & J & I \\ 2 & I & J' \end{Bmatrix} \zeta + \left| \begin{Bmatrix} F & J & I \\ 2 & I & J' \end{Bmatrix} \right|^2 \epsilon$$

where η, ζ, and ϵ are defined as

$$\eta = \frac{(I+1)(2I+1)}{I} \mu^2 \frac{|\langle J'||T^{(1)}_e||J\rangle|^2}{E_J - E_{J'}}, \tag{17}$$

$$\zeta = \frac{(I+1)(2I+1)}{I} \sqrt{\frac{2I+3}{2I-1}} \mu Q \frac{\langle J'||T^{(1)}_e||J\rangle \langle J'||T^{(2)}_e||J\rangle}{E_J - E_{J'}}, \tag{18}$$

and

$$\epsilon = \frac{(I+1)(2I+1)(2I+3)}{I(2I-1)} Q^2 \frac{|\langle J'||T^{(2)}_e||J\rangle|^2}{E_J - E_{J'}}. \tag{19}$$

In these final expressions, the reduced matrix elements have to be obtained from atomic theory calculations. [39]

2.2 Lasers and traps in nuclear physics studies

After the laser was first demonstrated in 1960, a wide range of laser applications has surfaced - many of which would not even be achievable in any other way. Lasers are the only man-made source that can generate pulses as short as $\leq 10^{-16}$ s and be used to measure absolute frequencies with an accuracy of $\sim 10^{-15}$. [2]

The use of lasers has made a major impact on nuclear structure studies since the monochromaticity of laser radiation provides excellent spectral resolution. They have a high power (in continuous waveform mW to W) which leads to enhanced sensitivity and thus opens possibilities for detecting low atomic densities. For example, 10 mW of laser power at 600 nm is equivalent 5 mA of photons (= 3×10^{15} photons/s). Lasers are nowadays also widely tunable: a wide range of the ultraviolet, visible and infrared spectrum can be continuously scanned with appropriate sources. Lasers' phase coherence results in beams that have narrow divergence so they can be focused to very small spot sizes, making remarkably large energy densities possible. Lasers can be applied effectively to almost any conventional hyperfine structure spectroscopy, allowing the measurement of nuclear moments, sizes, and shapes for nuclei far from stability. [47]

2.2.1 Basic operational principle of lasers

This chapter is adapted from the original text by R. Paschotta [2], which is suggested for further reading to obtain more detailed information about the basic operational principle of lasers.

The working principle of a laser is based on stimulated emission, which is the process where excited atoms convert stored energy into light. This usually starts when the excited atom first produces a photon by spontaneous emission. When this photon reaches another excited atom, the resulting interaction stimulates that atom to emit a photon as well. The photons generated from the process have identical properties: wavelength, direction, phase, and polarization. This ability to amplify light when enough excited atoms are present thus explains the acronym of Light Amplification by Stimulated Emission of Radiation (LASER).

The heart of the laser system is a laser cavity. A single pass through excited atoms or molecules is enough to initiate laser action in some high gain devices like excimer (= excited dimer) lasers, but for most lasers, it is necessary to have multiple passes through the lasing medium. This is implemented along an optical axis defined by a set of cavity mirrors producing feedback, and the lasing medium (e.g. crystal, semiconductor, enclosed gas) is placed on this axis. The axis has a high optical gain and it also becomes the direction of propagation of the produced laser beam. A very simple cavity has just two mirrors facing each other: total reflector and partial reflector (reflectance between 30% to almost 100%) as illustrated in figure 4.

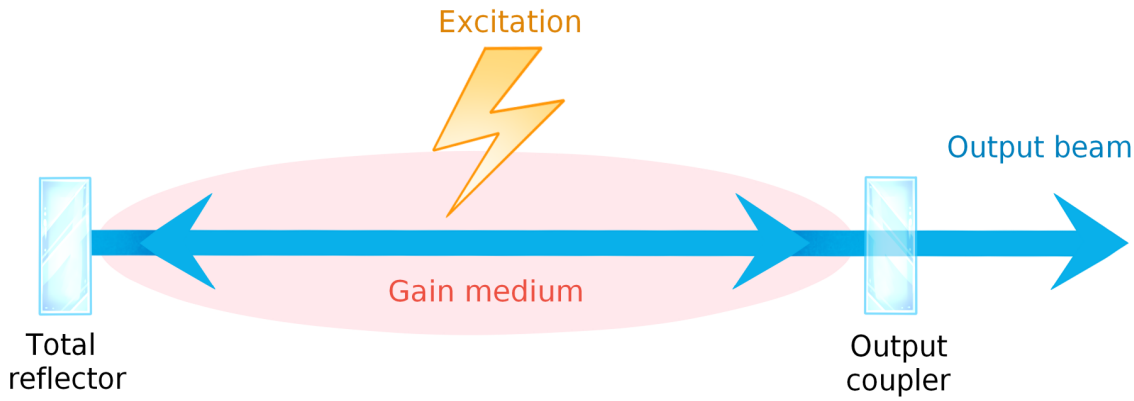

Figure 4: Simple illustration of a general laser, where the gain medium has a long, thin cylindrical shape and the cavity is defined by two mirrors with different reflectances. The gain medium excitation can be provided with e.g. a another pump laser, a flashlamp, or electric field.

Light bounces back and forth within these mirrors and gains intensity with each pass it makes through the gain medium. Photons that are not emitted into the direction of the axis are lost and do not contribute to the laser operation. As laser light amplifies, some of the light will escape the cavity through the partial reflector (called output coupler), but at the equilibrium state, these losses are fully compensated by the optical gain from the successive round trip of the photons inside the cavity.

For an ideal laser, all photons in the output beam are identical, which results in perfect directionality and monochromaticity. These determine the individual coherence and radiance of a laser source. A photon's energy is determined through relationship $E = hc/\lambda$, where h is Planck's constant, c is speed of light, and λ is wavelength. An ideal laser would emit photons with the same energy, thus the same wavelength and so be perfectly monochromatic. Many applications depend on monochromaticity even though real lasers are not perfectly monochromatic due to several broadening mechanisms that widen the frequency and energy of the emitted photons. The best known of these is the Doppler broadening, which is determined by the distribution of speeds in a collection of atoms that form a gas medium.

In addition to sharing the same wavelength, the photons forming the laser beam are in the same phase and thus coherent, which results in an electric field propagating with a uniform wavefront. In an ideal presentation, the plane wave propagates with a flat wavefront along a given direction and each plane that is perpendicular to this direction experiences the same electric and magnetic field amplitude and phase at a given time. However, real laser beams slightly deviate from this behaviour, but they remain the best approximate for a coherent plane wave.

Lasers can be dived into three categories: continuous wave (CW), pulsed, and ultrafast lasers. In this section, only CW lasers are discussed, as it was the type used in this thesis. CW lasers produce a continuous and uninterrupted beam of light which ideally has a very stable output power. The wavelengths or lines at which light is emitted depend on the characteristic of the laser medium. Each laser wavelength is associated with a linewidth that depends on several factors, such as the gain bandwidth of the lasing medium and the design of the optical resonator which can have elements such as filters and etalons to narrow the linewidth. Some solid-state lasers, like Titanium:Sapphire lasers, have remarkably broad bandwidth extending to hundreds of nanometres. This enables the design of tunable and ultrafast lasers.

2.2.2 Linear two-dimensional Paul traps

A quadrupole ion trap, also called a radiofrequency (RF) trap, or a Paul trap in honour of Wolfgang Paul who invented the device in the 1950s [48], uses dynamic electric fields for trapping charged particles. Earnshaw's theorem states that it is not possible to create a static configuration of electric fields to trap a charged particle in all three directions. However, it is possible to create an average confining force in all three directions by using time-dependent electric fields. This is done by switching the confining and non-confining directions at a rate faster than it takes for the particle to escape the trap. From this follows the name RF trap, as the switching is often done at a radiofrequency. The resulting field is inhomogenous and thus the average force acting on the particle is non-zero. If the frequency and amplitude of this quadrupolar electric field are configured precisely, the field converges towards the centre of the trap, as seen on the right side of figure 5. [49]

The simplest electric field geometry used is the quadrupole, and the electric fields are generated from the potential on the metal electrodes. A pure quadrupole is created using hyperbolic electrodes but cylindrical ones are often used since they are easier to manufacture. The electric field remains approximately quadrupolar in the middle of the cylindrical rods. Traps can be classified depending on whether the oscillating field confines the particles in two or three dimensions. The two-dimensional case, also called a linear Paul trap, provides confinement in the third direction by using static electric fields. The linear Paul trap has four quadrupole rods for the radial confinement of the charged particles and for the axial confinement a static electric potential is applied on the end-plate electrodes, as seen in figure 5, where a harmonically oscillating potential is applied between the adjacent electrodes [50].

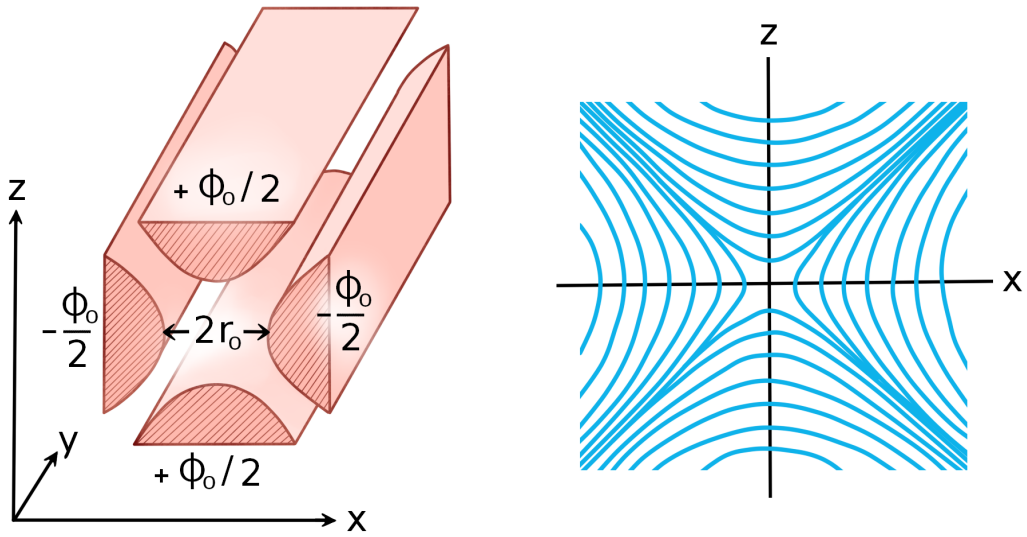

Figure 5: Illustrated on the left is the quadrupolar electrode structure of a typical Paul trap along with the field strengths corresponding to each electrode. On the right are the the equipotential lines for a planar quadrupolar electric field.

The particles are elastically bound to an axis if a force F which linearly increases with distance r acts on them:

$$F = -kr, \tag{20}$$

where k is a positive constant. Since the electric field is proportional to the force and equal to the divergence of the potential, we thus require a parabolic potential (in Cartesian coordinates) described by

$$\Phi \propto \alpha x^2 + \beta y^2 + \gamma z^2, \tag{21}$$

where α, β and γ are some constants. That is, we require an electric quadrupole field

$$\Phi = \frac{\Phi_0}{2r_0^2}(\alpha x^2 + \beta y^2 + \gamma z^2), \tag{22}$$

where r_0 is a normalization constant and Φ_0 a time dependent function. The equation (22) must fulfil the condition imposed on all potentials where there is no free charge distribution:

$$\nabla^2\Phi = 0 \quad \rightarrow \quad \alpha + \beta + \gamma = 0. \tag{23}$$

The equation (23) can be satisfied with two simple solutions which are the following:
1) $\alpha = 1 = -\gamma,\ \beta = 0$, which results in a two-dimensional field

$$\Phi_{2D} = \frac{\Phi_0}{2r_0^2}(x^2 - z^2) \tag{24}$$

2) $\alpha = \beta = 1,\ \gamma = -2$, which results in a three-dimensional configuration in cylindrical coordinates, which is explained in more detail in [51]. For hyperbolical electrodes that are linearly extended in the y-direction (see figure 5), the potential is $\pm\ \Phi_0/2$ if voltage Φ_0 is applied between the electrode pairs. The voltage Φ_0 is a superposition of a direct current (DC) voltage U and a radiofrequency voltage V:

$$\Phi_0(t) = U + V\cos(\omega t), \tag{25}$$

where ω is the driving frequency [50]. The field strengths are the following

$$E_x = -\frac{\Phi_0}{2r_0^2}x, \qquad E_y = 0, \qquad E_z = -\frac{\Phi_0}{2r_0^2}z \tag{26}$$

for the each of the three directions. [48]

The voltage confinement is obtained by segmenting the quadrupolar electrodes and applying static DC voltage to the outer segments. In addition, also alternating current (AC) voltage at a radiofrequency is applied for the quadrupolar field. This results in a potential minimum created along the y-axis which establishes the axial confinement, as seen in figure 6. In the MIRACLS setup, which was used in this work, the Paul trap consists of four pairwise coupled cylindrical electrode rods, each having five segments.

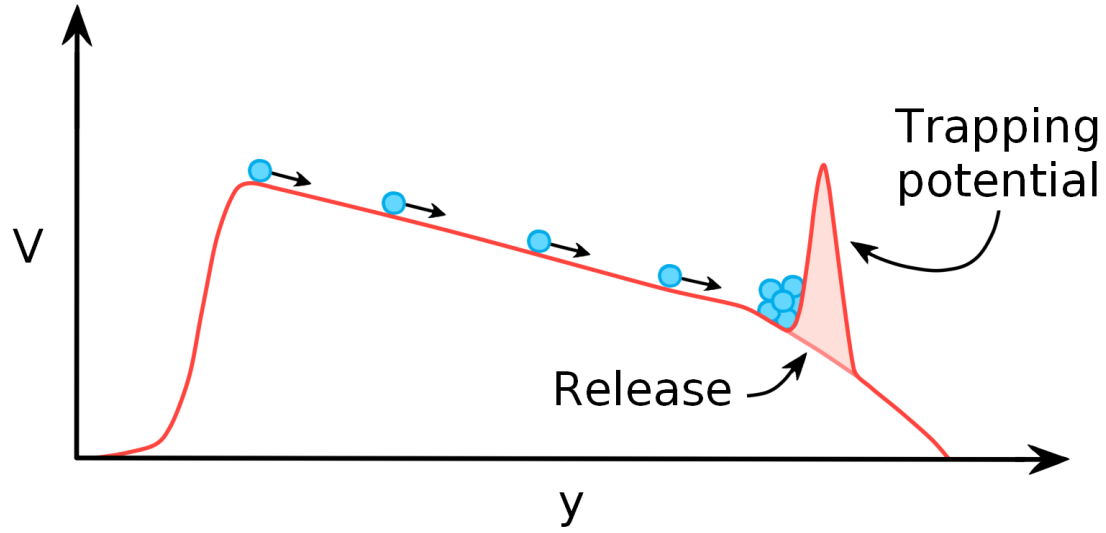

Figure 6: When a static DC voltage gradient is applied to the electrode segments, the particles become trapped at the potential minimum and are released when the trapping potential disappears.

The trapped particle experiences a harmonic oscillation along the longitudinal y-axis while having no transversal motion, so the expressions for E_x and E_z from equation (26) can be approximated as $E_x \approx \sin(t)$ and $E_z \approx \cos(t)$ as the radiofrequency field alters periodically in time. If the particles are injected in the y-direction, for a constant voltage Φ_0 they will experience harmonic oscillation in the xy-plane. Due to the opposite sign in E_z, their amplitude in the z-direction increases exponentially and the radial motion is different for each particle. The particles become defocused and will be lost when colliding with the electrodes. Thus the stability of a linear Paul trap depends on the applied axial DC potential. [48]

If a Paul trap is filled with a buffer-gas (e.g. helium), it can be operated as a cooler-buncher. The trap will collect the ions and cool them via collisions with the buffer-gas, resulting them to stay in the potential minimum until they are released in well-defined ion bunches. The potential of the last trap segment can be switched from high to low, meaning the trap will remain open from one side and the resulting axial potential ejects the ion bunch out of the trap. [49]

2.2.3 Multi Reflection Time-of-Flight devices

A Multi Reflection Time-of-Flight (MR-ToF) device is an electrostatic ion beam trap used for either storing ions or precision mass measurements and mass separation. A typical MR-ToF device, as seen in figure 7, is a low-energy electrostatic time-of-flight mass spectrometer, consisting of two electrostatic mirrors positioned at the end of a central drift

tube. Here the Earnshaw's theorem does not apply since the kinetic energy of the ions is not zero and hence in the ions' frame of reference, the electric field is not static [52].

The time-of-flight t of the ions is proportional to the square root of their mass-over-charge ratio:

$$t \propto \sqrt{\frac{m}{q}} \tag{27}$$

and also depends on the ions' initial conditions which have non-zero distributions for momentum and position. This initial phase-space spread results in time-spread Δt of the arrival times, which can be taken into account and reduced when designing the device - thus increasing its mass-resolving power which is defined as

$$R = \frac{m}{\Delta m} = \frac{t}{2\Delta t}. \tag{28}$$

To obtain higher mass resolving powers, the time-of-flight must be increased. This happens by either reducing the kinetic energy of the ions or increasing the length of their flight path [53]. Increasing the flight path can be done by trapping the ions between the MR-ToF device's electrostatic mirrors, leading to flight path lengths several times longer than the physical length of the device. In comparison with a single path spectrometer, an MR-ToF device can thus reach a mass-resolving power that is larger by several orders of magnitude (see [53] for more details).

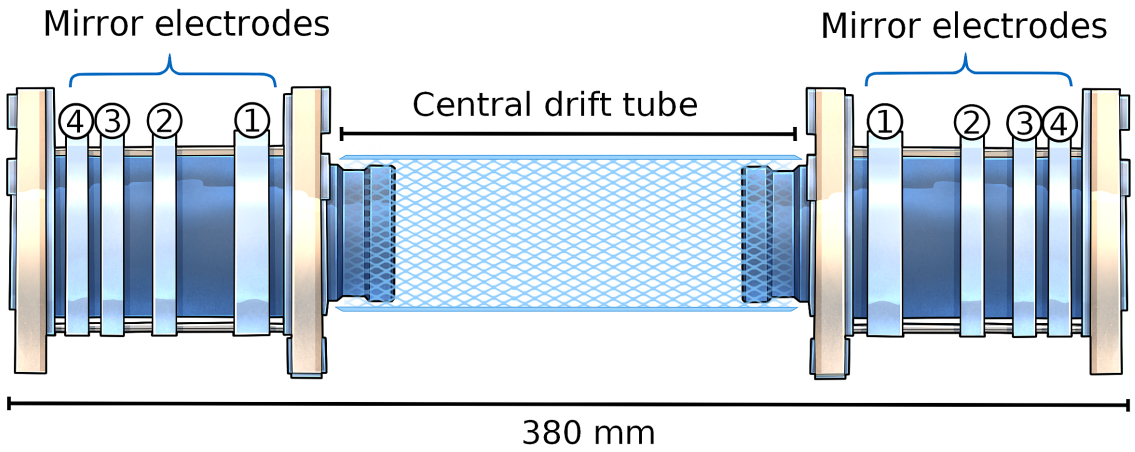

Figure 7: A schematic drawing of an MR-ToF device, where each electrostatic mirror is composed of four mirror electrodes and a conducting mesh covers the central drift tube located between the mirrors.

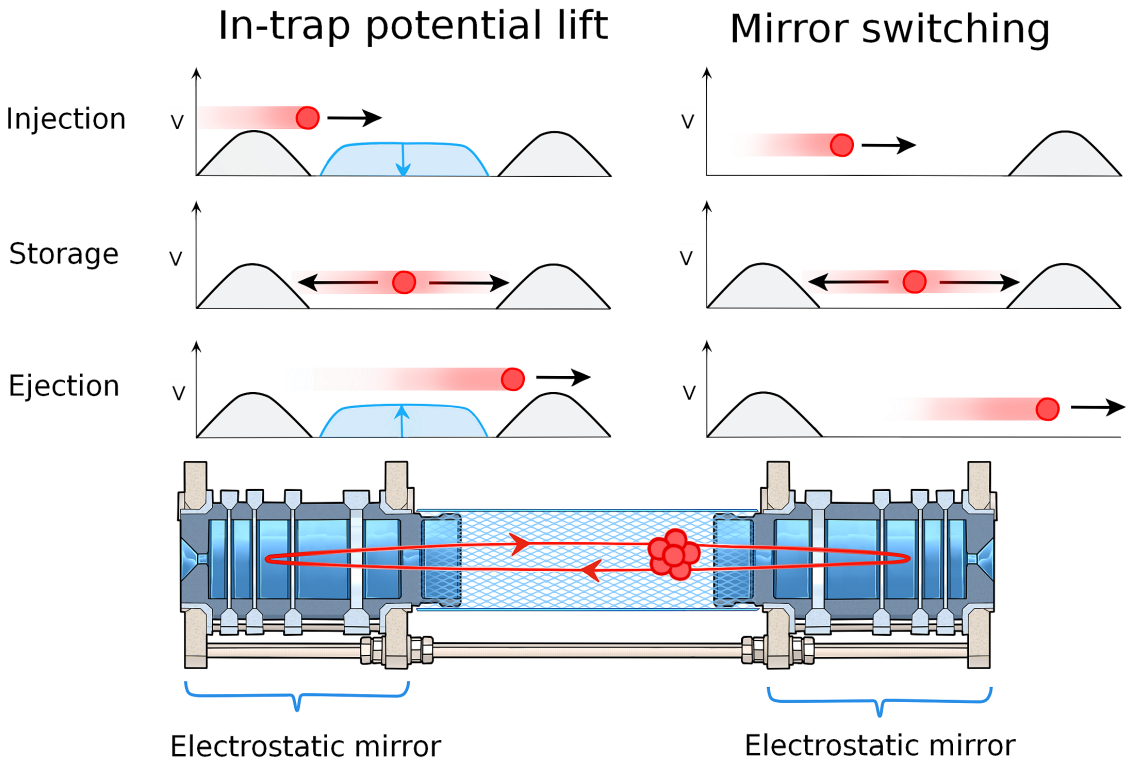

Figure 8: Above the MR-ToF cross-section are illustrated the two ejection methods, in-trap potential lift and mirror switching. The ion beam is depicted with red, in-trap potential with blue and the electrostatic mirrors' potentials with grey.

For the axial confinement of the ions, their kinetic energy in the drift tube must be smaller than the potential of the mirror electrodes. The confinement itself is done by the outermost electrodes while the innermost electrodes are used as ion lenses and provide radial refocusing. There are two techniques [54] to inject and eject the ions from the MR-ToF device , as illustrated in figure 8:

1. **In-trap potential lift**, where the mirror potentials stay constant but the ions are injected with kinetic energy high enough to overcome the mirror potentials. Right upon the moment when the ions enter the MR-ToF's drift tube, the lift potential is switched to the ground so the ions become trapped between the mirror potentials. The ejection process is similar and includes switching the lift potential back to eject the ions from the trap.

2. **Mirror switching**, where the injection mirror is switched down when the ion bunch reaches the MR-ToF so it can pass into the device. The ejection happens similarly by switching the ejection mirror down.

The in-trap potential lift is usually a favoured technique as it avoids the switching of sensitive mirror electrode potentials and so the electric noise and potential fluctuations remain minimal.

2.3 Collinear laser spectroscopy

As illustrated in figure 9, collinear laser spectroscopy (CLS) is performed by overlapping a narrow-band CW laser beam with a fast ion/neutral atom beam. When the wavelength of the laser is tuned to match the energy difference of the selected electric transition between the energy levels, the laser will provide resonant excitation of the ions. After this they spontaneously decay back to their ground-state, emitting fluorescence photons in the process.

Depending on the application, a charge-exchange cell (CEC) can be used to neutralize the ions before they enter the light collection region, where the photons are detected by photomultiplier tubes (PMTs). The hyperfine structure of the two states involved in the excitation is obtained by counting the number of observed fluorescence photons as a function of the scanned laser frequency.

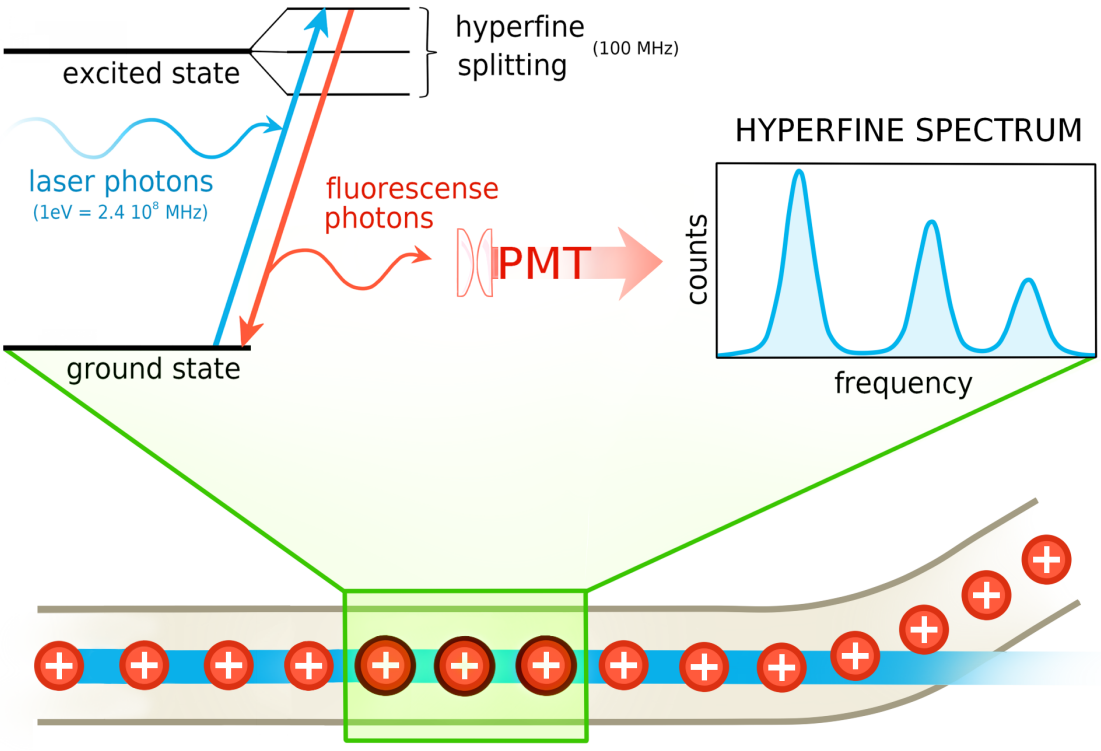

Figure 9: In a collinear geometry, laser (blue) and ion (red) beams are overlapped. The laser excites the ions to an excited state from where they decay back to the ground-state emitting fluorescence photons which then can be detected using a photomultiplier tube (PMT). Also shown is a hyperfine spectrum, where each peak corresponds to one transition from a hyperfine manifold to another, which is obtained when the photon counts are plotted as a function of the laser frequency.

In the reference frame of the ions the laser frequency ν_{REST} experiences a Doppler shift according to the relativistic Doppler effect [55]

$$\nu_{REST} = \nu_{LAB}\frac{1+\beta}{\sqrt{1-\beta^2}}, \tag{29}$$

where ν_{LAB} is the laser frequency measured by the wavemeter and β is the relativistic Lorentz factor

$$\beta = \frac{u}{c} = \sqrt{1 - \frac{m^2c^4}{(qV + mc^2)^2}} \tag{30}$$

where u is velocity of the ions, c is the speed of light, q is the electric charge of the ion, m is the mass of the ion, and V is the total acceleration voltage used. Thus, the frequency in the reference frame of the ions can be altered by applying an additional, tunable acceleration potential to the ions. This is called Doppler tuning, and it allows the locking of a laser frequency to a precise reference frequency. Some advantages from this method are the elimination of the systematic uncertainties associated with frequency scanning and additionally, the acceleration voltage can be changed in a faster and more reliable way than the laser frequency.

When using a collinear geometry, the laser beam (either counter- or co-propagating with the ion beam) interacts with the accelerated ion bunches that experience a velocity compression along their axis of motion. This compression is caused by the acceleration to a well-defined energy E while preserving the original energy-spread δE but reducing the velocity spread

$$\delta v = \frac{1}{\sqrt{2mE}}\delta E, \tag{31}$$

where m is the mass of the ion [13]. The longitudinal velocity spread needs to be reduced as much as possible to obtain narrow linewidths which are crucial for resolving the hyperfine structure. This is done by accelerating the beam with 30-60 keV acceleration voltage before it enters the CLS setup and as a result, the linewidth is reduced to a level similar to the natural linewidth (Doppler compression), which is some tens of MHz [56].

Due to its high accuracy and precision, CLS is a powerful tool that allows access to the nuclear ground-state properties of radionuclides far from stability, and thus provides valuable insight into the nuclear shell structure. Nowadays it is routinely used at RIB-facilities to study properties like the nuclear spin, the electromagnetic multipole moments, and the mean-square charge radius for a wide range of nuclei [13]. These observables can be extracted independently of any nuclear model, and thus provide important insight into the nuclear structure and properties.

The experimental sensitivity is improved by using a cooled and bunched ion beam. The cooling leads to a better laser-ion overlap in the light collection region due to improved beam quality. Another advantage is the possibility of background suppression. As the primary source for background in CLS comes from continuous sources, such as the laser stray light and PMT dark counts [57], it can be reduced significantly by time-gating the signal from the PMTs on the narrow ion bunch.

2.3.1 Spectral lineshapes and broadening mechanisms

The natural linewidth is the minimal linewidth that the resonance peaks in the hyperfine spectrum have due to the Heisenberg's uncertainty principle. It is described by a Lorentzian lineshape and determined from the finite lifetime τ of the excited state

$$\Gamma = \frac{1}{2\pi\tau}. \tag{32}$$

The natural linewidth is extremely difficult to obtain experimentally, as several broadening mechanisms affect the width and shape of the peaks. One of these is the **Doppler broadening**, which is the inhomogeneous broadening often much larger than the natural linewidth when using low beam energies. When an atom is moving with velocity u with respect to the observer, it experiences a non-relativistic shift for frequency

$$v = v_0\left(1 \pm \frac{u}{c}\right), \tag{33}$$

where v_0 is the mean optical frequency and the + sign refers to the emitter moving towards the observer, and the $-$ sign for the emitter moving away from the observer. For atoms with thermal velocity distribution in temperature T, the linewidth resulting from the Doppler effect is described by a Gaussian profile

$$\Delta v_D = \frac{2v_0}{c}\sqrt{2\ln 2\frac{k_B T}{m}}, \tag{34}$$

where k_B is the Boltzmann constant. However, this effect can be eliminated by employing a measurement technique that is insensitive to Doppler broadening. [58]

Another broadening mechanism is a **power broadening** which originates from the stimulated emission induced by the laser photons. This effect decreases the lifetime of the excited state compared to the lifetime with only spontaneous decay. Power broadening can also be described by a Lorentzian lineshape. Yet other mechanisms are a **transit-time broadening** caused if the laser-ion interaction time is small compared to the lifetime of the excited state (negligibly small for CLS), and **pressure broadening** originating from the interaction with other particles (usually negligible for CLS due to vacuum conditions). Taking all these different broadening mechanisms into account, the resulting line-

shape is described by a Voigt profile, which is convolution of the saturated Gaussian and Lorentzian profiles. The Gaussian profile can be described by

$$\Delta v_G = \left(\frac{1}{\sigma\sqrt{2\pi}}\right)^{-(x-a)^2/2\sigma^2}, \tag{35}$$

where σ is the standard deviation, a is the mean, and the Gaussian full-width at half maximum (FWHM) is $\Gamma_G = 2\sigma\sqrt{2\ln 2} = 2.355\sigma$. The Lorentzian profile is

$$\Delta v_L = \frac{1}{\pi}\frac{\Gamma_L/2}{(x-x_0)^2 + (\Gamma_L)^2}, \tag{36}$$

where x_0 is the centre and Γ_L is the Lorentzian FWHM. [59]

The total linewidth of the Voigt profile [60] can be presented as an approximation:

$$\Delta v_V \approx 0.53456\Delta v_L\sqrt{0.2166\Delta v_L^2 + \Delta v_G^2}. \tag{37}$$

A comparison between the lineshapes obtained with the Gaussian, Lorentzian and Voigt profiles is shown in figure 10.

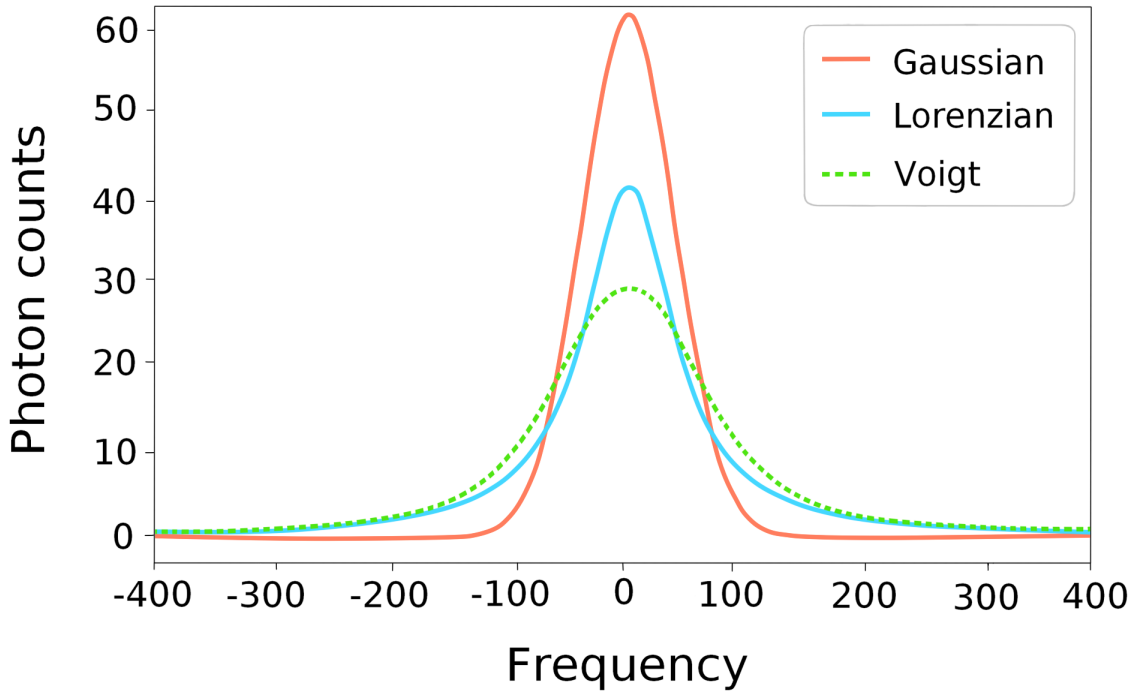

Figure 10: A comparison between Gaussian, Lorenzian, and Voigt lineshapes with the same full-width half-maximum (FWHM) and the same normalized integral area.

2.3.2 Optical pumping

Optical pumping refers to the act of injecting light into some medium to excite it into the higher-lying energy levels. It is used both in laser physics and in fundamental physics, where e.g. several laser cooling methods rely on the optical pumping of the atoms or ions.

In spectroscopic measurements, the intention can be to selectively populate a certain state, like some hyperfine sublevel. The selection rules due to the conservation of the angular momentum play an essential role. This makes it possible to e.g. perform a selective pumping of certain states within a manifold of states. For many cases, such a process involves several optical pumping steps and spontaneous emission before the targeted states are predominantly populated. Additionally, optical pumping can be used for isotope separation as different isotopes have somewhat different transition energies, to resonantly move the population to and from different states, to induce nuclear orientation in radionuclides and thus allow resonance detection when observing the resulting decay anisotropy, to move populations to states which are more efficient or suit better for collinear laser spectroscopy purposes, and sequentially move a population to higher excitation energy until ionization takes place. [13, 58]

Optical pumping can sometimes result in problematic effects, like in the MIRACLS setup (described in the following chapter) where the population is pumped out from the state of interest. This is the reason why the use of radiofrequency is explored to possibly repopulate that state and boost the signal detected in the measurements.

2.4 General concept of MIRACLS

The Multi Ion Reflection Apparatus for Collinear Laser Spectroscopy (MIRACLS) was introduced in 2017 [61] to take better advantage of the exotic radioactive isotopes produced at ISOLDE-CERN, by probing the same ion many times, thus increasing the observation time and therefore the experimental sensitivity. Conventional CLS is typically limited to nuclides whose production yields are relatively high, ranging between 1000 – 10 000 ions per second. The laser-atom interaction time is of the order of microseconds, while the half-life of the ions is tens of milliseconds or more. The most exotic nuclides, residing far from the valley of stability, are produced with low production yields, so new methods are needed to measure their nuclear properties. One example is to detect ions produced in a laser ionization process, rather than the photons which are emitted by the atoms. This method, called Collinear Resonance Ionization Spectroscopy (CRIS), only requires production rates of the order of 10 ions per second [62].

The approach taken by MIRACLS is to utilize the entire lifetime of the exotic radioisotopes by using a Multi Reflection Time-of-Flight (MR-ToF) device to trap a bunched ion beam meanwhile performing CLS on it. When the ions are trapped between the MR-ToF device's two electrostatic mirrors, the laser will interact with them at each revolution and thus effectively increases the interaction time compared to conventional CLS, where the laser only interacts with the ion beam once. Theoretically, the only efficiency limitation for MIRACLS is thus the maximal trapping time and the half-life of the ions. This means the MIRACLS method would allow access to nuclides with very low production yields. A schematic picture of the MIRACLS Proof-of-Principle (PoP) setup is shown in figure 11. The method is especially suitable for studying closed two-level systems, where the ions decay directly from the excited state to the initial state without populating other metastable fine or hyperfine structure states in between. For other systems, this spontaneous decay can populate other states, which leads to a reduction in signal as the number of revolutions increases.

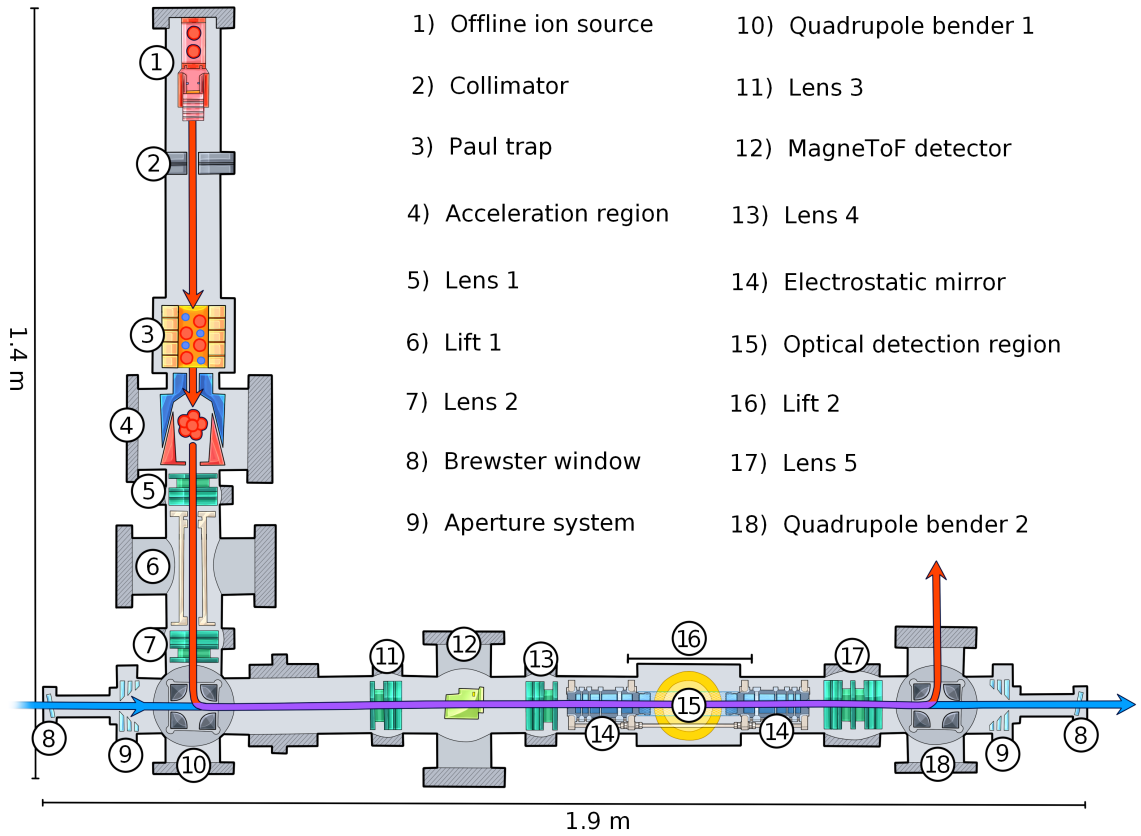

Figure 11: A schematic drawing of the MIRACLS PoP-setup where an offline ion source (1) produces a continuous ion beam, which is injected into a Paul trap (3) and accelerated (4). Then, the ion bunches are trapped in the MR-ToF device (16). The ion beam is depicted by red line and the laser beam with blue. See the text for details.

Typically, CLS is performed at beam energies of about 30 keV to minimize the Doppler broadening. The MIRACLS PoP-setup is being tested at a lower beam energy of 1.3 keV using an offline ion source and an MR-ToF device modified for laser spectroscopy, to demonstrate the feasibility of the method. MIRACLS aims to work with 30 keV kinetic energies after the PoP-stage when an MR-ToF suitable for 30 keV beam energies will be designed and constructed.

As illustrated in figure 11, an offline (magnesium) ion source produces a continuous ion beam which is first collimated and then injected into a buffer-gas (helium) filled linear Paul trap for cooling, accumulation and bunching. After the time-focused ion bunches are released from the Paul trap, they are accelerated with the crown-shaped electrodes towards an electrostatic Einzel lens (lens 1) and a pulsed drift tube (lift 1) which is switched from high voltage (HV) to ground when the ions have reached its centre. The ions gain a kinetic energy of approximately 2 keV and continue travelling towards the second Einzel lens (lens 2) and the first electrostatic quadrupole bender (QPB1), which bends the ion beam 90° onto the MR-ToF axis. Between the QPB1 and MR-ToF, there's a retractable MagneToF detector for beam diagnostics. The ion beam is focused by Einzel lenses 3 and 4 before the injection into the MR-ToF device. In the MR-ToF the ions are trapped for several revolutions, while the laser probes them during each revolution. The laser provides a resonant optical excitation of the ions: when the laser is held in resonance with one HFS component of the optical line it excites the ions to the ionic excited state, from which they will spontaneously decay to several lower levels and emit fluorescence photons. These photons can then be detected by a PMT in the optical detection region of the MR-ToF device's drift tube (also called central drift tube, or lift 2 in figure 11). A more detailed view of the operation of the MR-ToF is illustrated in figure 8. At the end of the beamline, there's another quadrupole bender (QPB2) that bends the beam 90° towards a multichannel plate detector for detection. The laser beam enters and exits the setup through quartz windows installed at Brewster angles (called Brewster windows) in order to minimize reflections. Next to these, sets of aperture systems are installed to minimize the background photon counts.

The MR-ToF device in the MIRACLS PoP-setup consists of two electrostatic mirror electrodes, each composed of four cylindrical electrodes and a central drift tube (two electrodes connected by a fine, conducting mesh). The innermost of the mirror electrode segments are biased to a negative potential to achieve a radial ion refocusing. The three outer electrodes provide reflecting potential walls used to confine the ions.

2.5 Laser-radiofrequency double-resonance method

The laser-radiofrequency double resonance (LRDR) method can be used to either fast or thermal beams of atoms or ions. The general working principle on thermal beams is as follows: The laser beam is split into a weaker probe beam ($\sim$ 1 mW) and stronger pump beam (50 - 200 mW), both of which will intersect the atomic beam orthogonally, as illustrated in figure 12. A PMT can be used to detect the fluorescence produced by the probe laser in the atomic beam. [36]

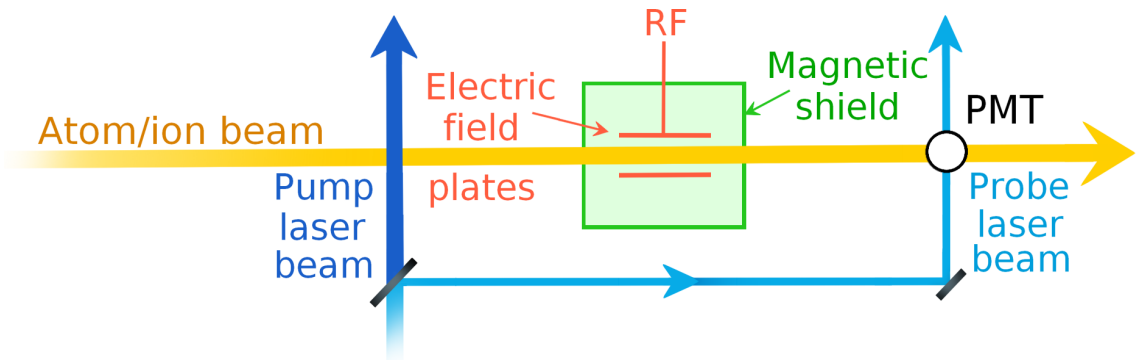

Figure 12: Illustration of a cross-beam LRDR setup, where the atom/ion beam interacts with the pump laser beam, radiofrequency (RF) field, and probe laser beam, respectively. A resonant increase in fluorescence is detected with a PMT giving a direct measurement of the HFS interval of the lower state.

When the pump laser beam is blocked, scanning the laser wavelength through an atomic line results in the observation of the individual hyperfine components of the optical line. Since the residual Doppler broadening is small for a well-collimated atom beam, the components are generally well-resolved and 5 - 15 MHz wide. When the pump laser beam is unblocked and the laser held in resonance with one of the HFS component of the optical line, the atoms in the beam experience an efficient excitation to the upper state from where they will spontaneously decay to several lower levels. This is an example of an optical pumping process, which was described in chapter 2.3.2. To be noted, the lower level of the optical de-excitation is usually not the same level from which the atom was initially excited. Thus, the population of the lower HFS level becomes heavily depleted. The effectiveness of this op-

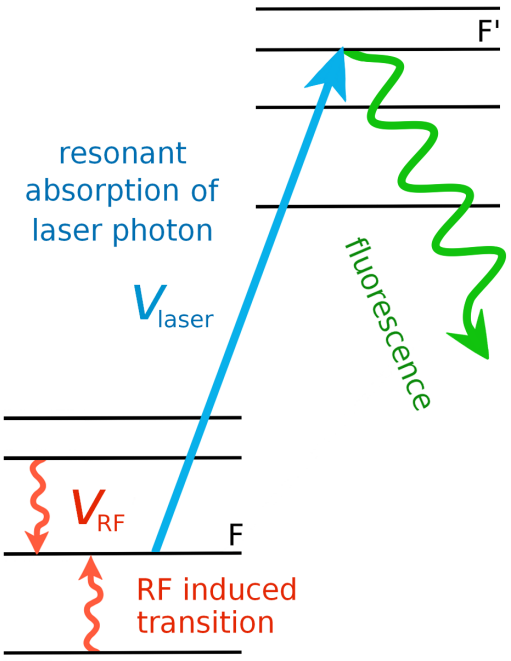

Figure 13: Absorption of the laser photon causes an excitation from lower level F to upper level F' and the population in F becomes depleted. Level F is repopulated by inducing a magnetic transition from $F \pm 1$ level with a suitable RF field. The following laser-excited fluorescence is then observed.

tical pumping is furthermore enhanced if the atoms have a slow (thermal) velocity which results in longer interaction time with the pump beam. So even the atoms that decay back to their initial lower state will have sufficient time to absorb another photon before leaving the pump region. After interacting with the pump beam, the atoms continue until they are irradiated with the probe laser beam. Since the population of the appropriate lower state HFS was already greatly depleted, the probe beam is not able to cause much fluorescence. However, if a suitably chosen radiofrequency (RF) transition is applied to repopulate the depleted level, a resonant increase in the fluorescence can be observed. This process is also illustrated in figure 13. The linewidth of these double-frequency signals depends on the transit-time of the atoms in the RF field and is typically $\sim$ 10 kHz. Nearly every transition which connects the depleted and the populated level satisfying the E1 or M1 selection rules can be used. The transition usually ranges from RF to microwave regimes and arrangement like this allows for the measurement of the lower-state hyperfine intervals to a precision of 1 kHz or better. [36]

Experimentally, an LRDR measurement is executed by the tuning the laser wavelength into resonance with a selected HFS component of an optical line, thus allowing the pump beam to deplete the population in the lower levels. As the laser wavelength is held fixed, can the frequency of RF be swept repeatedly through a range where resonance is to be expected, while the fluorescence is observed as a function of the RF frequency. [63]

2.5.1 Using LRDR in collinear geometry

The use of fast beams for optical spectroscopy is preferred since it reduces the Doppler width and provides excellent overlap between the atom and the laser beam, compared to a cross-geometry experiment on collimated beams. However, since the linewidth of the RF resonance depends on the transit time of the ions travelling through the RF region, and that with a fast beam the transit-time is rather short, the experimental linewidths will be broad. Illustrated in figure 14 is a collinear LRDR setup for slow ion beams, where the interaction region consists of three sections: pump region (A), probe region (B), and RF region (C). To prevent the laser from being in exact resonance with the Doppler-shifted ions along the collinear beam path, small post-acceleration Faraday cages are included in A and B regions. When they are kept at a small potential of around a few hundred volts, the ions and laser are tuned to resonance within these two regions and will not be in resonance in other sections. Apart from this, the arrangement is fully analogous to the cross-beam version described above. [64]

The pump and probe regions can be identically constructed resonant absorption regions where the laser-induced fluorescence occurs. In the pump region, the ions absorb laser photons resonantly, causing a transition from hyperfine level F of lower state to the hyperfine level F' of the upper state. As a result, the level F becomes depleted. It can be

repopulated to some extent by inducing a transition between the neighbouring hyperfine level $F \pm 1$ with the application of a suitable RF field in the C region. The RF resonance can then be detected by scanning the applied RF, and thus the hyperfine splitting in the lower level can be measured with high precision. Typical linewidths achieved in the literature are of the order of 100 kHz. [63, 64]

As compared to the conventional optical collinear laser spectroscopy, the collinear LRDR comes with the distinct advantage that it offers superior resolution, and therefore yields more precise hyperfine constants. This precision, in turn, can allow measuring e.g. hyperfine anomalies or the higher-order nuclear moments. An important disadvantage is the reduced efficiency of the method, due to the inherent inefficiencies of e.g. the optical pumping, the RF excitation process, and the transmission losses due to the larger size of the apparatus. Furthermore, special care has to be taken to avoid light-shifts in the RF spectra, since the laser beam is also present in the RF interaction region. In chapter 4, it will be investigated how to adapt this collinear LRDR geometry into the MIRACLS concept.

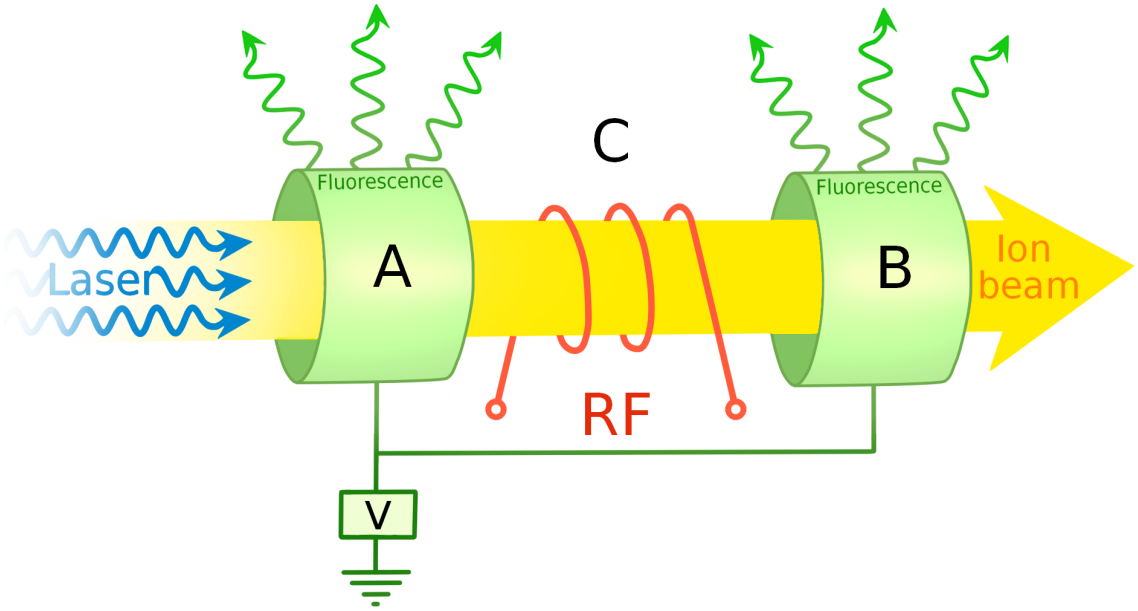

Figure 14: A schematic illustration of a collinear LRDR setup, where A is the pump region, B is the probe region, and C is the radiofrequency region with an RF electrode. A and B consist of similar open-ended cylindrical Faraday cages.

3 Study of the magnetic octupole moment of ^{173}Yb

3.1 Experimental setup at the IGISOL

This chapter will provide a brief introduction to the current IGISOL-4 facility and its collinear laser spectroscopy line and the relevant equipment located at the Accelerator Laboratory in the Department of Physics, University of Jyväskylä (JYFL-ACCLAB). The offline measurements with atomic ^{173}Yb will also be described in detail.

3.1.1 IGISOL-4 facility

The Ion-Guide Isotope Separator On-Line (IGISOL) is a research facility located at JYFL-ACCLAB. The current version of the IGISOL-setup at JYFL is the fourth in order (IGISOL-4) and the research mainly focuses on collinear laser spectroscopy, decay spectroscopy and high-precision mass spectrometry. The IGISOL method was developed in Jyväskylä in the 1980s to produce radioactive ion beams of exotic nuclei and has since then been adapted to other facilities as well. The method allows the primary recoils to be mass-separated on-line and is chemically insensitive allowing the production of radioactive beams from all elements, also including the refractory elements that are usually difficult to produce at the ISOL-facilities. The current layout of the entire IGISOL-facility is presented in figure 15, where most of the equipment is located on the first floor, with the offline ion sources being on the second floor. [65]

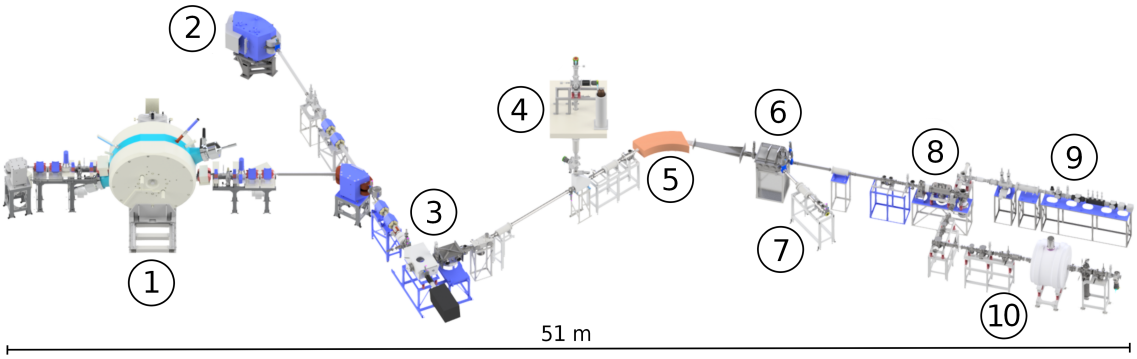

Figure 15: The IGISOL-4 facility beamline consists of the following components:

1) MCC30/15 cyclotron
2) Beamline from K130 cyclotron
3) Target chamber and laser ionization in-gas-cell/in-jet
4) Offline ion sources
5) IGISOL separator magnet
6) Focal plane of switchyard
7) Decay spectroscopy line
8) RFQ cooler-buncher
9) Collinear laser spectroscopy line
10) Mass spectrometry and post-trap spectroscopy

At the IGISOL the primary beam can be provided by two cyclotrons: K130 (heavy ions and high-energy light ions) and MCC30/15 (protons and deuterons). The beam from the cyclotron is delivered to the ion guide, which is also called the front end, where it impinges to a thin target foil and causes the formation of reaction products that scatter out of the target material into a gas cell. In their way out, the reaction products lose some of their energy due to energy-straggling and in the end, they will stop in the target chamber filled with high-purity helium gas. The products will undergo a charge-exchange with the helium gas and thermalize, resulting in a high amount of singly charged ions. The ions are then extracted from the charge-exchange cell (CEC) using a sextupole ion guide (SPIG) and accelerated to 30 keV in the beamline. A dipole magnet of mass resolving power $m/\Delta m = 350$ (high enough to select the mass number) is used for mass separation of the extracted ions. Then the ion beam enters the switchyard, which is a vacuum chamber housing ion optical elements, to be bent to either the decay spectroscopy line or towards the radiofrequency quadrupole (RFQ) cooler-buncher. In the RFQ, the ions accumulated, cooled, and bunched. After the extraction from the RFQ, the ions are passed through a low-energy (800 eV) transfer section, two quadrupole benders each of which deflects the beam by 90°, before being reaccelerated to 30 keV energy. This allows optical access to the central axis of the RFQ by shining laser light through the quadrupole bender [66]. The produced ion bunches are delivered either to the collinear laser line or to JYFLTRAP Penning trap for more precise mass separation, mass spectrometry and post-trap spectroscopy.

Alternatively, the ions of interest can also be produced offline. This happens by replacing the gas cell with a glow-discharge spark ion source. This ion source is based on a phenomenon called glow-discharge, which can be generated by applying voltage into two electrodes inside a gas medium. If the gas pressure, the distance between electrodes, and applied voltage are suitable, a current starts to flow between the two electrodes. When the conditions are favourable, this results in a glow-discharge reaction that can be even seen with the naked eye. However, a small current does not result in any visible effects. The discharge relies on external radiation, such as cosmic radiation or natural radioactivity, to get started by generating the first ions. [67]

3.1.2 Collinear laser line

A schematic view of the collinear laser line at the IGISOL-4 is illustrated in figure 16. The 30 keV ion beam enters the collinear beamline from the right side of the figure and is guided by the XY steerers and focused by the quadrupole triplet before entering the CEC. This cell consists of a cylinder, fillable with a chosen neutralizing element, and is mounted on an electrically insulated platform. The platform can be floated to $\pm$ 10 kV and used to Doppler-tune the atom into resonance with the laser. Heating is provided

electrically with a variable AC power supply while keeping both ends of the cylinder at a constant temperature using an oil circulator. The ions that are not neutralized in the charge-exchange reactions between the gas are deflected from the atom beam using a pair of electrostatic deflector plates immediately after the cell. After the CEC, there is a light collection region (LCR) with a segmented PMT. To reduce the amount of scattered light reaching the PMT, several knife-edge baffles are placed near the LCR. The beamline also has two Faraday cups and a silicon detector for optimizing the transport efficiency. A micro-channel plate (MCP) detector is placed off-axis with retractable MagneToF mini detector for beamtuning and monitoring of the neutralization efficiency. The laser beam enters the setup from the left in the figure through a telescope system (pictured in figure 18) and the overlap of the ion and laser beam is achieved by tuning both of them through a removable 0.9 mm aperture. [68]

The signals from the PMT segments are first amplified and then discriminated with a constant-fraction discriminator. After this, the signals are time-stamped by a time-to-digital converter. The hyperfine structure of the studied isotope can be scanned by applying an acceleration/deceleration potential to the ion beam. This potential needs to be changed with precise reproducibility and short settling time. To do this, a voltage ranging between -4 and 4 V is generated by the analogue output of a data acquisition board and amplified with a high voltage amplifier. Both devices have large slew rate and fast settling time enabling the fast voltage sweeps needed. After each scan, a calibration for the voltage scanning range is carried out by a digital multimeter, which reads out the scanning voltage after a 1:10^3 voltage divider. The voltage of the RFQ cooler platform can be monitored similarly. [68]

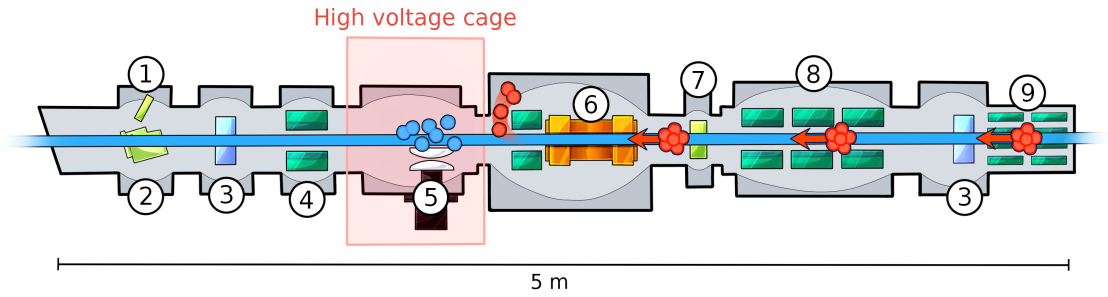

Figure 16: The ion beam arrives from the right and laser beam from the left into the collinear beamline at the IGISOL, which consists of the following components:

1) Micro-channel plate detector
2) MagneToF mini detector
3) Faraday cup
4) Electrostatic deflector
5) Photo multiplier tube
6) Charge-exchange cell
7) Silicon detector
8) Quadrupole triplet
9) XY steerers

3.1.3 Collinear laser spectroscopy of ^{173}Yb

In this work, the Yb ions were produced with the offline glow-discharge ion source, resulting in an intense beam of 10^{10} ions/second. They were extracted from the source with a beam energy of 30 keV, and guided into a dipole magnet for isotope selection. Upon accelerating the Yb ion beam from the room temperature to 30 keV, the kinematic compression of the velocity distribution of the ions enables quasi-Doppler free spectroscopy. The mass resolving power of the magnet was high enough to allow an isobarically pure, separated beam. After this, the mass-selected ions were injected into the gas-filled RFQ cooler-buncher to be cooled through collisions with room-temperature helium gas.

The ions were extracted from the RFQ as a continuous beam with a 30.192(3) keV energy (see chapter 3.2.2 for details) and guided to the collinear laser line, where they were passed through a charge-exchange cell filled with 120 °C potassium vapour, which was used to neutralize the ions in charge-exchange reactions. The neutralization process populates the atomic ground-state predominantly, while a fraction of the atoms exits the charge-exchange cell at metastable $^3P_2^\circ$ state. According to the theoretical calculations presented in [69], a useful fraction of the Yb ions should undergo the neutralization into the selected metastable state as the charge-exchange reaction between K and Yb has a large cross-section and it is non-selective enough to populate several states. Next, the atom beam was overlapped with a counter-propagating laser beam which was produced with a Sirah Matisse TS (Titanium:Sapphire) laser and a frequency locked to a commercial HighFinesse WSU-10 wavemeter to ensure long-term wavelength stability. A Sirah wavetrain external frequency-doubling cavity was used to double the laser's output frequency. More detailed view of the laser system is presented in chapter 3.1.4. The velocity of the atoms could be altered by changing the acceleration voltage applied to the CEC. This acceleration voltage was measured with a 1:10^3 voltage divider, and a digital multi-meter for calibration, correcting non-linearities in the voltage scan.

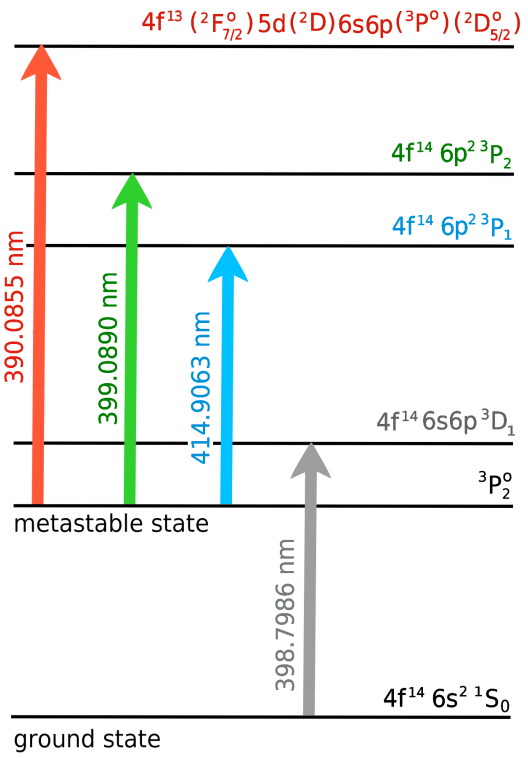

Figure 17: The three optical transitions used in this work, line 1 (390.0855 nm) in red, line 2 (399.0890 nm) in green, and line 3 (414.9063 nm) in blue, and the ground-state line in grey (398.7986 nm).

Table 2: Summary of all the transitions from the initial and final states which were used in this work, including their wavelengths λ, and wavenumbers $\tilde{\nu}$.

Transition	Initial state	Final state	λ [nm]	$\tilde{\nu}$ [cm^{-1}]
[a]	$^3P_2^\circ$	$4f^{14}6p^2\ ^3P_2$	399.0890	44760.370
[a]	$^3P_2^\circ$	$4f^{13}(^2F_{7/2}^\circ)\ 5d(^2D)$ $6s6p(^3P^\circ)\ (^2D_{5/2}^\circ)\ (J=2)$	390.0855	45338.530
[a]	$^3P_2^\circ$	$4f^{14}6p^2\ ^3P_1$	414.9063	43805.420
[b]	$4f^{14}6s^2\ ^1S_0$	$4f^{14}6s6p\ ^3D_1$	398.7986	25068.222
[c]	$4f^{14}6s^2\ ^2S_{1/2}$	$4f^{14}6p\ ^2P_{1/2}^\circ$	369.4190	27061.820

[a] Transition from the metastable state.
[b] Transition from the ground-state.
[c] Reference measurements using $^{171,173}Yb^+$ to calibrate the beam energy.

The hyperfine structure of the atoms was measured by Doppler shifting the laser wavelength that was observed in the atoms' rest frame. The spectroscopy itself was performed using three different optical transitions from the metastable $^3P_2^\circ$ state, and one transition from the ground-state $4f^{14}6s^2\ ^1S_0$, as illustrated in figure 17. These transition lines were at 399.0890 nm, 390.0855 nm, and 414.9063 nm and are detailed in table 2. From these measurements, the ratio of the atoms in the metastable $^3P_2^\circ$ state to the $4f^{14}6s^2\ ^1S_0$ ground-state can be approximated to be 1:10^4. However, this ratio seems to peculiarly disagree with the theoretical estimate presented in [69]. Despite this low number of atoms in the metastable $^3P_2^\circ$ state, a clear hyperfine structure spectrum could be achieved in a few hours. Also, reference measurements of the hyperfine intervals of the ground-states for $^{171}Yb^+$ and $^{173}Yb^+$ were performed to calibrate the beam energy. This is described in more detail in chapter 3.2.1.

3.1.4 Laser system

Collinear laser spectroscopy experiments at the IGISOL are nowadays conducted using a laser laboratory which includes two Sirah Matisse 2 CW lasers pumped by a 20 W Spectra Physics Millenia eV laser, as illustrated in figure 18. These Matisse lasers are the dye laser (model DS) and Titanium:Sapphire laser (model TS), and they are used with WaveTrain 2 frequency doubling units.

In this work, the Matisse 2 TS laser was used and its optical layout is shown in figure 19. It is an actively stabilized Titanium:Sapphire ring laser [70]. The ring laser's resonator has the form of a ring and the ring cavity contains e.g. the Titanium:Sapphire gain medium, etalons, and filters for frequency control, and a unidirectional device. Compared to standing wave (linear) laser resonator, the ring resonator enables two different

propagation directions for the intracavity light. The unidirectional device is an "optical diode" which only allows propagation in one direction around the ring. Once the unidirectional operation is accomplished, there is no standing wave interference pattern in the gain medium, and no spatial hole burning. Thus, a single-frequency operation is achieved with ease. [58, 71]

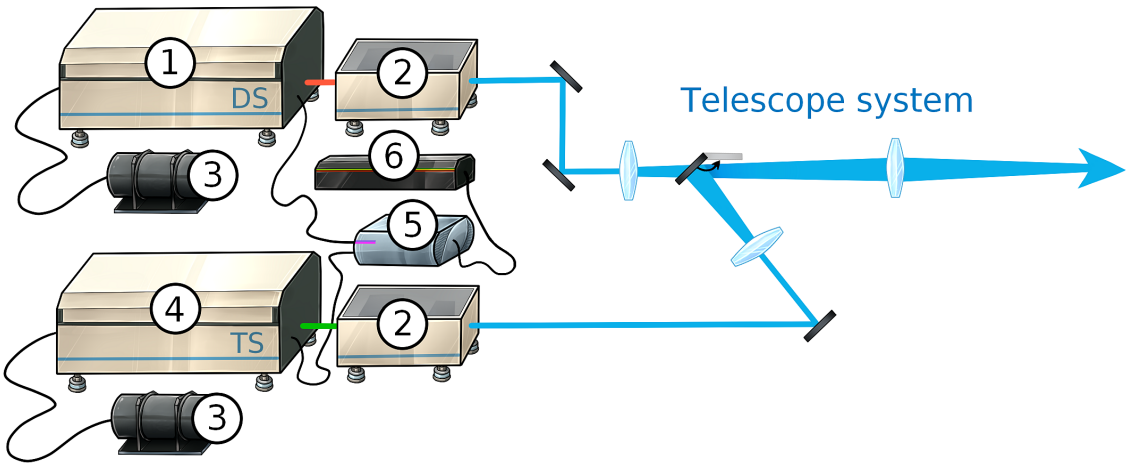

Figure 18: A schematic drawing of the laser system at the IGISOL-4 collinear laser line including the following components:

1) Sirah Matisse DS laser
2) Wavetrain 2
3) Reference cell
4) Sirah Matisse TS laser
5) WSU-10 wavemeter
6) Helium neon (HeNe) laser

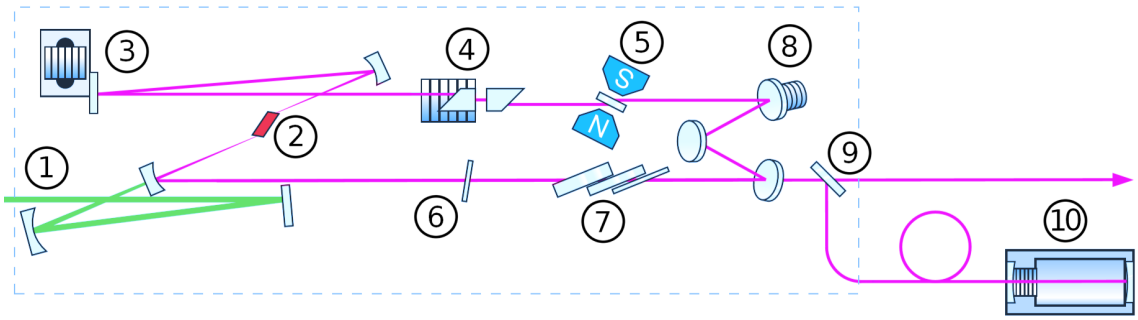

Figure 19: The optical layout of Sirah Matisse 2 TS Titanium:Sapphire laser, figure edited from [70]. The pump beam (green) enters from the left.

1) Pump laser input
2) Titanium:Sapphire crystal
3) Tuning mirror
4) Piezo-driven thick etalon
5) Unidirectional device
6) Motor-driven thin etalon
7) 3-plated motor-driven birefringent filter
8) Fast piezo
9) Output coupler
10) Reference cavity

Each laser has different sets of mirrors coated to correspond to specific wavelength ranges, thus selecting only part of the full emission spectrum of the lasing medium. Selection of a single frequency mode is done by scanning the birefringent filter and the thin etalon. Here the birefringent filter consists of three birefringent plates of varying thicknesses and the frequency can be selected by rotating the plates.

To accomplish a single-mode operation, two etalons are needed. These are the thin etalon (a solid-state etalon) which narrows the frequency range, and the piezo-driven thick etalon to select the final frequency mode. The unidirectional device is used to make sure that the laser is in a clockwise running mode. Finally, the laser frequency can be scanned by altering the cavity length with the fast piezo-driven tuning mirror. To establish short-term stability (i.e. a narrow linewidth), the laser has an external reference cavity that is coupled to the fast piezo-driven cavity mirror with a feedback loop. For long-term stability, the reference cavities can be locked into the WSU-10 wavemeter or to a frequency-stabilized HeNe (helium-neon) laser using a transfer cavity.

For most of the elements studied in this setup, it is required to have frequency-doubled light. This is achieved by using WaveTrain 2 frequency-doubling units which have triangular enhancement cavity that contains a temperature-stabilized nonlinear crystal. The crystal generates the second harmonic of the fundamental frequency from the laser. This frequency-doubled laser light can then be focused into a 1 mm spot in front of the PMT with the telescope system, and typical background rates due to the scattering of the laser light are approximately 100 Hz for each 100 μW of laser light [68].

3.2 Data analysis for the hyperfine constants

The experiment was conducted as described in chapter 3.1.3 and the number of photons was measured with a PMT for each acceleration voltage sweep. A calibrated acceleration voltage V, as described in equation (30), was used and defined as a sum of the acceleration voltage, and the RFQ cooler platform voltage, respectively:

$$V = V_{\text{acceleration}} + V_{\text{cooler}}. \tag{38}$$

An example of the obtained hyperfine spectra is presented in figure 20, where the x-axis is the frequency of the laser in the atom's frame of reference, with a large number subtracted ($\sim 12000\,\text{cm}^{-1}$) to see the differences in the frequencies since the hyperfine structure is about six magnitudes smaller than the frequency of the laser. Each peak corresponds to a transition from one hyperfine manifold to another; the number of peaks is determined by nuclear and atomic spins, and the positions of the peaks correspond to the size of the nuclear moments. The nuclear moments, including the magnetic octupole moment, can be determined by measuring the distance between the peaks.

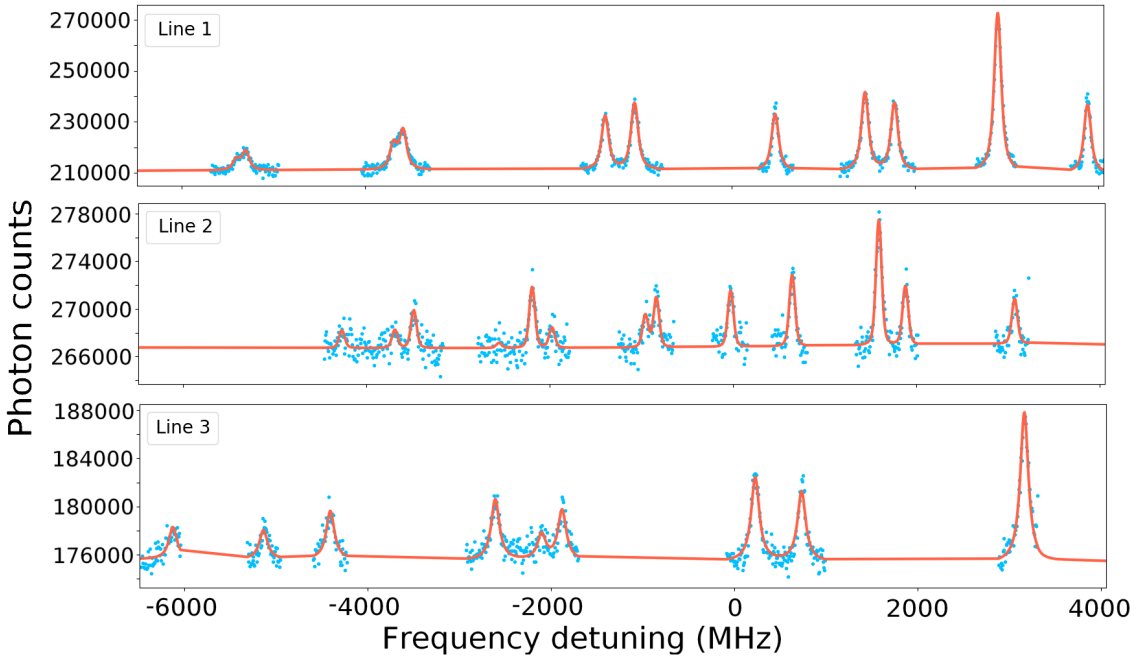

Figure 20: Example of the spectra obtained with the three optical transitions used: line 1 = 390.0855 nm, line 2 = 399.0890 nm, and line 3 = 414.9063 nm. Data points are in blue and red line is the best fit. See the text for details.

One potential source for the systematic uncertainties in this measurement is caused by the determination of the RFQ cooler platform voltage. This will be discussed in more detail in chapter 3.2.1. From the obtained hyperfine spectra, all the hyperfine constants, A, B, and C, can be extracted. This is done by using the Statistical Analysis Toolbox for Laser Spectroscopy (SATLAS) which is a Python package that combines several formulas typically used in the analysis of laser spectroscopy results [72].

The spectra were fitted using Voigt profiles that were centred at the resonance locations. These locations were anticipated with equation (5). By performing a χ^2-minimization, the optimal values were achieved for the hyperfine constants, spectral linewidths, peak heights, and background counts. The uncertainties were then approximated from the inverse of the Hessian matrix and scaled with the reduced chi-square $\sqrt{\chi^2_\nu}$. Here the χ^2_ν was calculated as

$$\chi^2_\nu = \frac{\chi^2}{n_d}, \tag{39}$$

where n_d is the number of degrees of freedom. For more details, see [72]. In this work, the χ^2_ν for was obtained from the best fit procedure and taken into account in the final data analysis for the hyperfine constants.

Each of the performed fits had seven free parameters which were associated with the hyperfine constants: A, B, and C for each upper and lower state, including a centroid wavelength. As there were more than seven resonances in each optical line, the fit was

over-determined. This over-determination reduces the statistical uncertainties, which results in precise values for the hyperfine constants although the signal-to-background ratio was somewhat poor in some of the scans. To determine the final values for each set of extracted hyperfine constants, their weighted mean was calculated including the standard error of the weighted mean as the uncertainty.

To calculate the weighted mean for a data set of elements x_i, the weight w_i for each element can be determined as a reciprocal of the variance σ_i:

$$w_i = \frac{1}{\sigma_i^2}, \tag{40}$$

when the weighted mean itself is defined as

$$\bar{x} = \frac{\sum_{i=1}^{n} w_i x_i}{\sum_{i=1}^{n} w_i}. \tag{41}$$

Typically, there exists some error in the variance of each individual data point, e.g. arising from the fact that experimental errors may be underestimated if some error source is forgotten, or if there is error in the calculation of the variance for each data point. In this case, a correction must be made in the variance of the weighted mean:

$$\hat{\sigma}_{\bar{x}}^2 = \sigma_{\bar{x}}^2 \chi_\nu^2, \tag{42}$$

where χ_ν^2 is the reduced chi-squared and the square root of $\hat{\sigma}_{\bar{x}}$ is the standard error of the weighted mean, while $\sigma_{\bar{x}}$ is defined as

$$\sigma_{\bar{x}} = \left(\sqrt{\sum_{i=1}^{n} w_i} \right)^{-1}, \tag{43}$$

with the variance weights included. [73]

3.2.1 Determination of the RFQ cooler voltage offset

A source for systematic uncertainty of the hyperfine constants arises from the uncertainty of the ion beam energy. If incorrect beam energy is assumed during the analysis, the frequency scale of the hyperfine structure in the rest frame of the atoms experiences a small stretching which might result in some distortion in the extracted hyperfine intervals. Though, not much effect from this is expected for the value of the octupole constant C, as the non-zero C is only manifested as a small perturbation on top of the considerably larger dipole and quadrupole splittings. Regardless, this effect was carefully considered and removed by performing an ion beam energy calibration. This calibration relies

on reference measurements for the hyperfine intervals of the singly-charged $^{171}Yb^{+}$ and $^{173}Yb^{+}$. Since these particular intervals have been measured extremely precisely, could the beam energy calibration be performed [68].

To study this ionic ground-state, the temperature of the charge-exchange cell was brought to room temperature and thus the ion beam no longer experienced neutralization. Thus, CLS could be performed using the ionic 369.4190 nm line from the $4f^{14}6s^2\ ^2S_{1/2}$ state to the $4f^{14}6p\ ^2P^{\circ}_{1/2}$ state at 27061.820 cm^{-1}. In total, three scans were taken for both $^{171}Yb^{+}$ and $^{173}Yb^{+}$.

To understand how much the deviation in the RFQ cooler voltage would affect on the obtained values of the hyperfine constants, the results from the $^{171}Yb^{+}$ and $^{173}Yb^{+}$ data analysis were plotted as in figure 21. On the y-axis is the difference between the weighted mean of the extracted hyperfine constant A_1 and the corresponding literature value, which are presented in table 3. The values for $^{173}Yb^{+}$ were multiplied by three, so the values for both isotopes scale similarly with the cooler voltage offset, accounting for the different nuclear spins of the two isotopes.

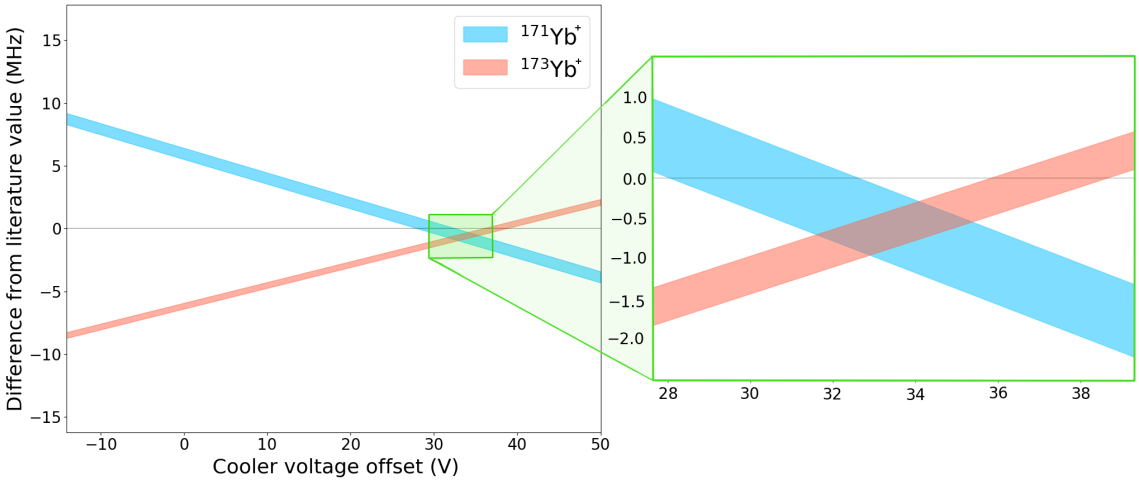

Figure 21: Demonstrated here is how much the different cooler voltage offsets affect the hyperfine constant A_l for $^{171}Yb^{+}$ and $^{173}Yb^{+}$. The red and blue lines include errors, and were calculated as a difference from the corresponding literature values.

Table 3: Summary of the extracted values for the hyperfine constants A_1 with the energy calibration, and their corresponding literature values, which were used to make the figure 21. Note that the error bars here are purely statistical, and do not include a systematic uncertainty due to the acceleration voltage.

Isotope	Weighted mean of A_1 [MHz]	Literature value of A_1 [MHz]	Ref.
$^{171}Yb^{+}$	12641.89(45)	12642.8121184682(4)	[74]
$^{173}Yb^{+}$	-3497.36(23)	-3497.24007985(3)	[75]

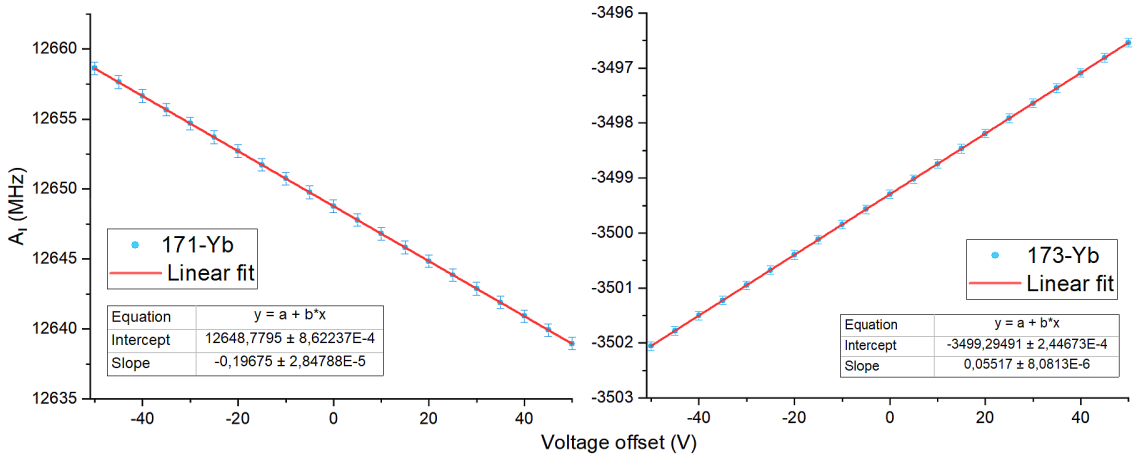

Figure 22: On the left, $^{171}Yb^{+}$ is plotted and on the right is $^{173}Yb^{+}$. Linear fit was done for the datapoints using Origin Pro 2020, and from the resulting equation the values for the voltage offset to obtain the literature value were solved. These offset voltage values were $V_{\text{off}}^{171} = 30.3298$ V and $V_{\text{off}}^{173} = 37.2166$ V.

The hyperfine constant A_1 obtained from each of these as a function of a voltage offset range is plotted in figure 22. This figure also shows the linear fit used to determine the voltage offset required to match the literature values listed in table 3. This procedure was followed for both $^{171}Yb^{+}$ and $^{173}Yb^{+}$. Then, a weighted arithmetic mean was taken, yielding ≈ 35.3 V. Note that the datapoints used in this fit were independent, and thus the errors given by the linear fit are very small and therefore cannot be used. Instead, the uncertainty on the offset voltage was obtained by propagating the mean uncertainty on the experimental hyperfine A_1 constants. This value was further scaled by the reduced chi-square [73]:

$$\chi_\nu^2 = \frac{1}{(n-1)} \sum_{i=1}^{n} \frac{(x_i - \bar{x})^2}{\sigma_i^2}, \tag{44}$$

where $n = 2$ for this case, and σ_i was the the standard error of the weighted mean from table 3. Following this procedure, the final value for the voltage offset was $V_{\text{offset}} = 35.3(34)$, and it was added to the calibrated total ion beam energy for the final data analysis:

$$V = V_{\text{acceleration}} + V_{\text{cooler}} + V_{\text{offset}}. \tag{45}$$

3.2.2 Systematic uncertainties in the experimental setup

The beam energy was assumed to have a 3 V uncertainty whose effect on the hyperfine constants was approximated by refitting the spectra with -3 and +3 V offset to the beam energy. The hyperfine constant values from these spectra were subtracted from the values given in table 6. From the obtained values for $\pm$ 3 V spectra, means were taken to get the final values, which are presented in table 4. It can be concluded that 3 V systematic

uncertainty on the beam energy does not affect the values of the hyperfine constants within our precision (see final results from table 6). Drifts and relative changes in the ion beam energy were monitored and determined to be considerably less than 1 V for the entire duration of the measurement, and thus also affect our results negligibly.

The second-order energy corrections due to the perturbation of the close-lying states $^3P_1^\circ$ and $^3P_0^\circ$ have not been performed, but they were estimated to be much smaller than the experimental precision in this work, according to [12]. Nevertheless, atomic structure calculations of the overlapping matrix elements with both $^3P_1^\circ$ and $^1P_0^\circ$ are currently ongoing, so these effects can be estimated later.

The mass-resolving power of the used mass separator dipole magnet was also carefully optimized to make sure no trace of ^{172}Yb and ^{174}Yb was present in the beam. If not accounted for, e.g. a small resonance due to the even-even neighbouring masses lying close to the ^{173}Yb resonance might affect the hyperfine constants. However, no evidence of such resonances (whose position was well known from previously conducted separate measurements) was observed in the obtained spectra.

Additionally, the photon background was discovered to not be constant over the full scan range as it was dominated by the light resulting from the spontaneous emission of Yb atoms after the charge-exchange reactions. The scanning over broad voltage ranges creates small-scale changes in the atoms' trajectories, thus leading to a change in the number of the photons detected by the PMT. To be able to fit this photon background, a second-order polynomial was employed, scarcely affecting the hyperfine constant values.

Note that if there are systemic effects which influence all three lines equally, these would remain undetected. However, to our knowledge, no such effects should be present.

Table 4: Summarized here are means of differences in the hyperfine constants of each line in MHz when the beam energy was assumed to have a $\pm$ 3 V systematic uncertainty.

	ΔA_l	ΔB_l	ΔC_l	ΔA_u	ΔB_u	ΔC_u
Line 1	-0.0032	-0.0009	6.6E-05	0.0025	-0.0002	-1.8E-05
Line 2	-0.0081	-0.0010	4.6E-05	-1.5E-05	-0.0002	3.0E-05
Line 3	-9.2E-05	0.00050	-1.7E-06	-0.0001	0.0003	–
All lines	-0.0038	-0.0007	5.4E-05	–	–	–

3.2.3 Constraining of the overlapping peaks in the spectra

In some of the spectra partially overlapping resonances were detected. However, for these overlapping peaks their ratio of amplitudes can be constrained by using a ratio of the absolute theoretical intensities [13]:

$$I_{FF'} \propto (2F+1)(2F'+1)\begin{Bmatrix} F & F' & 1 \\ J & J' & I \end{Bmatrix}^2 F_{JJ'}, \tag{46}$$

where the factor in the curly brackets is the Wigner 6-j symbol and $F_{JJ'}$ is the unperturbed fine structure transition. The use of this ensures the convergence of the fit while also preventing the convergence of non-physically small amplitudes for one of the components. The peaks which were constrained are listed in table 5 and visually presented in figure 23.

Table 5: Summary of the constrained peaks for each line used. Depicted on the horizontal lines are the peak pairs whose amplitudes were constrained as they were slightly overlapping, or converging to zero amplitude.

	Peak on left	Location [MHz]	Peak on right	Location [MHz]
Line 1	1.2_1.2	-5405.31	1.2_3.2	-5291.46
	3.2_3.2	-3575.65	3.2_5.2	-3551.65
Line 2	1.2_1.2	-3690.61	3.2_5.2	-3469.40
	5.2_5.2	-944.53	7.2_9.2	-842.785
Line 3	5.2_7.2	-2099.53	5.2_3.2	-1883.53

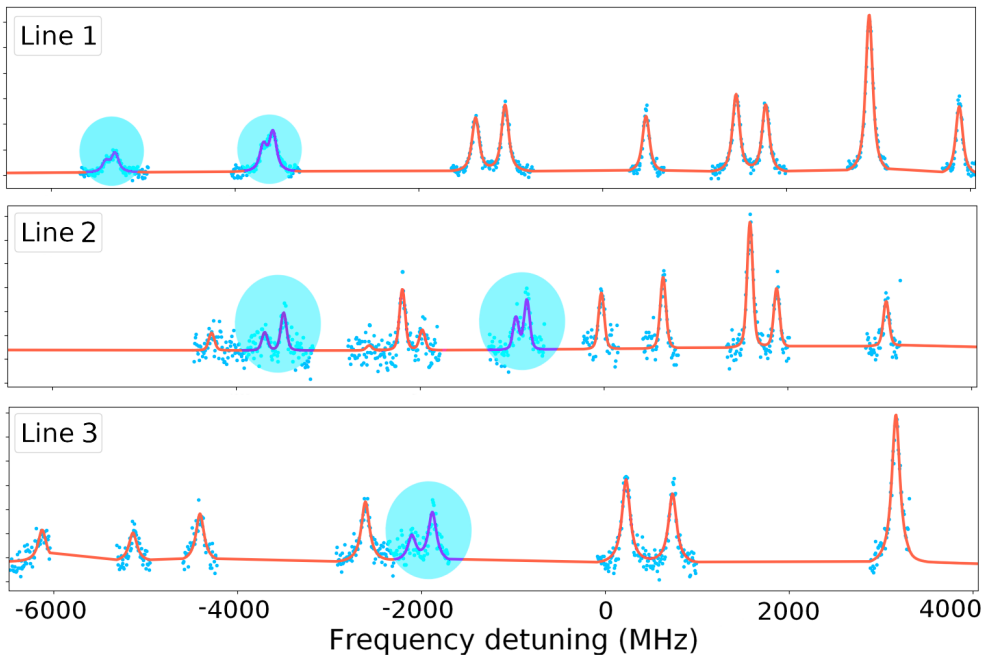

Figure 23: The peaks shaded with blue were slightly overlapping or their amplitudes were converging to zero in some of the scans and thus needed to be constrained. More information about the peaks can be found in table 5.

3.2.4 Stability of the RFQ cooler voltage and the laser frequency

The RFQ cooler platform voltage and the laser frequency were monitored during the measurement, and presented in figures 24 and 25, respectively. As can be seen, the cooler voltage was lowered by about 10 V before the last four scans of the measurement, to optimize the cooler transmission efficiency. To get a hold of the significance of this offset, a 10 V offset in the beam energy would correspond to $\sim$ 2 MHz offset in the extracted values of the hyperfine constants compared to their literature values. However, the laser frequency only experienced very minor fluctuations (maximum of about 1.6 MHz) in frequency during the whole measurement, so the effect from it should be very small.

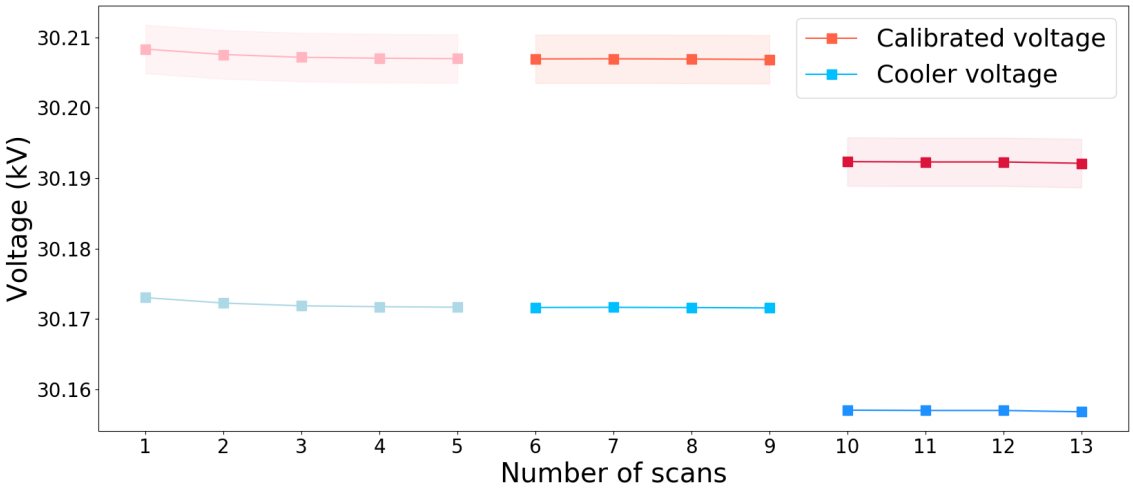

Figure 24: The shaded red area is the error for the calibrated RFQ cooler voltage. There was about a 10 V drop in the RFQ cooler voltage during the last part of the measurement. The calibration of the voltage is explained in chapter 3.2.1.

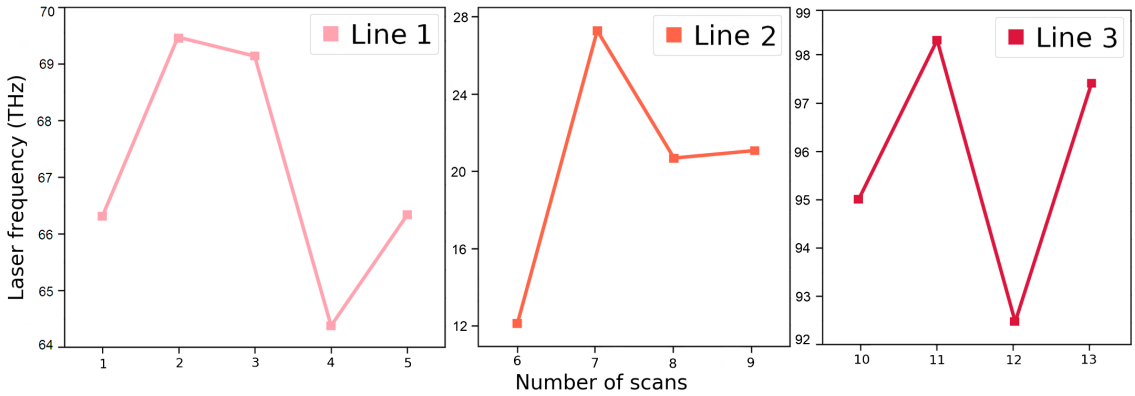

Figure 25: Shown here on the y-axis is the laser frequency in THz with a large number subtracted. These numbers were: line 1 (375.25471 THz), line 2 (383.91566 THz), and line 3 (360.94972 THz).

3.3 Extracted hyperfine constants for the lower and upper states

Data from the used three different lines seemed to provide consistent values, thus presenting a measure of confidence for the final hyperfine constants which are presented in table 6. The constants are also compared to the existing literature values in table 7. The constants of the upper states (A_u, B_u, C_u) have no known literature values the so a comparison there was not possible. The uncertainties of the hyperfine constants are presented in the brackets and are purely statistical.

As it can be seen, a satisfactory agreement for the hyperfine constant A_l is obtained, but the value for B_l has a bit larger deviation and C_l differs greatly from the literature. And as an interesting note, the hyperfine constant A_u of the $4f^{14}6p^2\ ^3P_1$ state would be zero within the uncertainties of this measurement. The hyperfine constants A_l, B_l, C_l are plotted in figures 26, 27, and 28, and the constants A_u, B_u, C_u in figures 29, 30, and 31, respectively. For the metastable $^3P_2^\circ$ state, the hyperfine constant C_l is zero within one standard deviation for each line.

Table 6: Summary of the hyperfine constants extracted in these measurements. The uncertainties (one standard deviation) are given in brackets and they are calculated as the standard error of the weighted mean from the values which were obtained for each measurement scan.

	A_l [MHz]	B_l [MHz]	C_l [MHz]	A_u [MHz]	B_u [MHz]	C_u [MHz]
399.0890 nm	-741.9(3)	1343.9(23)	0.08(17)	-123.3(2)	-628.8(24)	0.10(17)
	-741.7(2)	1346.7(18)	0.16(13)	-123.4(2)	-629.1(17)	0.05(12)
	-742.3(2)	1347.5(19)	-0.06(14)	-123.4(2)	-631.3(18)	0.27(13)
	-742.3(2)	1350.8(23)	-0.19(16)	-123.5(2)	-628.7(20)	-0.07(14)
	-741.7(5)	1346.1(47)	-0.20(32)	-123.7(5)	-631.6(39)	0.01(28)
Weight. mean	-742.0(1)	1347.2(10)	-0.01(7)	-123.4(10)	-629.8(9)	0.08(7)
390.0855 nm	-741.9(3)	1350.3(29)	0.12(22)	-347.7(3)	121.4(26)	-0.15(20)
	-741.7(6)	1346.4(50)	-0.01(35)	-347.9(5)	115.5(45)	-0.35(34)
	-741.6(6)	1351.7(47)	-0.13(26)	-347.6(7)	112.7(66)	0.46(49)
	-741.8(4)	1346.0(39)	0.48(28)	-347.4(39)	122.3(35)	-0.22(28)
Weight. mean	-741.8(2)	1348.9(19)	0.12(13)	-347.6(2)	120.0(18)	-0.15(14)
414.9063 nm	-742.0(4)	1343.8(36)	-0.12(26)	0.06(68)	483.4(18)	–
	-742.1(5)	1346.6(36)	0.21(28)	-0.64(83)	484.1(21)	–
	-742.1(7)	1350.9(61)	-0.38(43)	-0.05(106)	485.8(28)	–
	-741.0(9)	1338.8(75)	0.45(43)	1.51(140)	483.5(37)	–
Weight. mean	-742.0(3)	1345.4(23)	0.01(17)	-0.01(45)	484.0(12)	–
All lines	-741.98(9)	1347.3(8)	0.02(6)	–	–	–

Table 7: Comparison between the weighted mean of the all lines used in this work and two different literature values.

Reference	Year	A_l [MHz]	B_l [MHz]	C_l [MHz]
This work	2020	-741.98(9)	1347.3(8)	0.02(6)
[12]	2013	-742.11(2)	1339.2(2)	0.54(2)
[76]	1991	-742(5)	1342(38)	–

To be noted that at least one peak in the observed HFS spectra was smaller than the background noise but still visible in some of the scans, however constraining it did not affect any of the values of the extracted hyperfine constants within the uncertainties of this measurement.

Using all 13 scans measured, the weighted mean of the constants C_l from the metastable $^3P_2^\circ$ state is zero at the 1σ (68%) confidence level. This value of 0.02(6) MHz considerably differs from the 0.54(2) MHz value obtained by using the 769.9487 nm line in [12]. So far, the cause for this deviation remains unclear. Using our current setup, it was not possible to conduct measurement using this line as the wavelength of the spontaneously emitted light from the atoms lies outside the sensitivity range of the used photomultiplier tube. Thus, further research using the 769.9487 nm line might shed light on this matter.

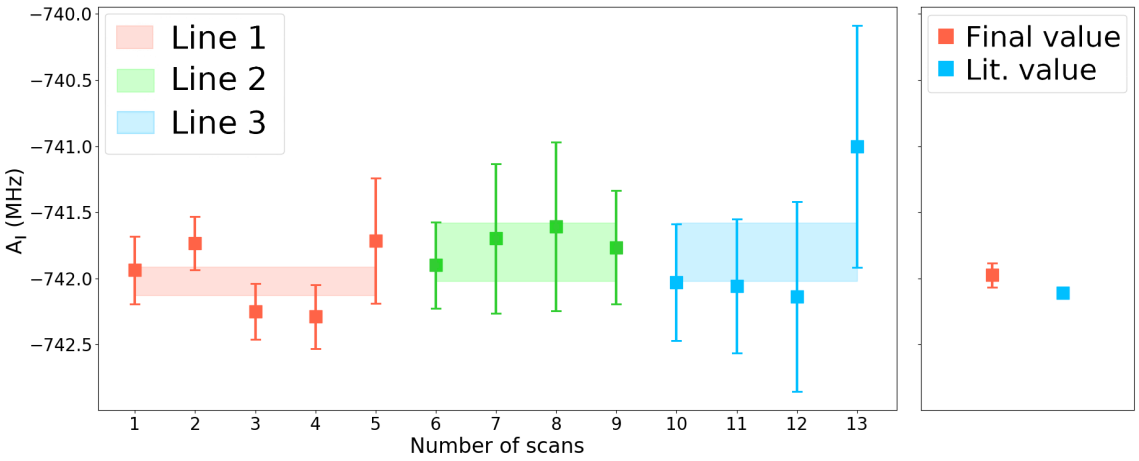

Figure 26: All the values which were extracted for hyperfine constant A_l in this measurement, where the shaded areas represent the weighted mean of each line. On the right, the weighted mean of these 13 scans is compared to the value obtained in [12].

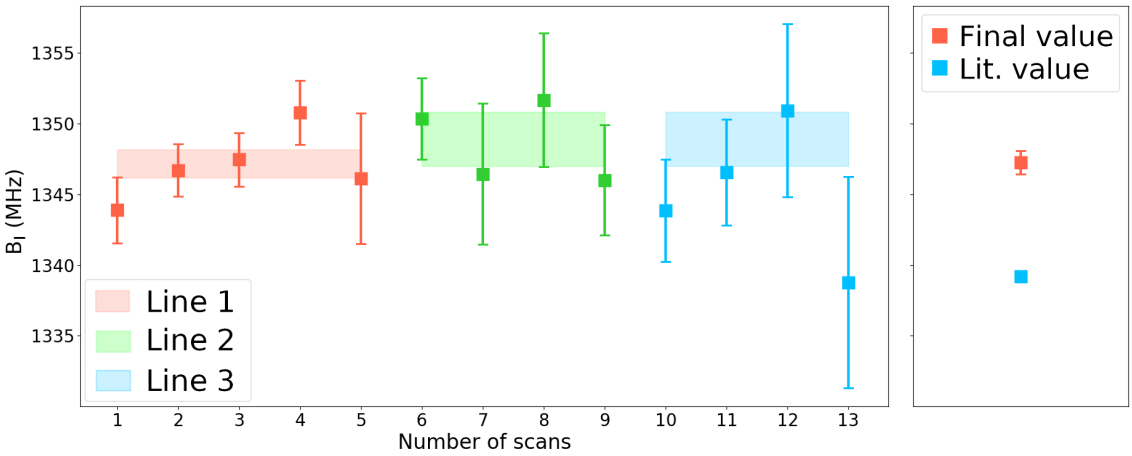

Figure 27: All the values which were extracted for hyperfine constant B_l in this measurement, where the shaded areas represent the weighted mean of each line. On the right, the weighted mean of these 13 scans is compared to the value obtained in [12].

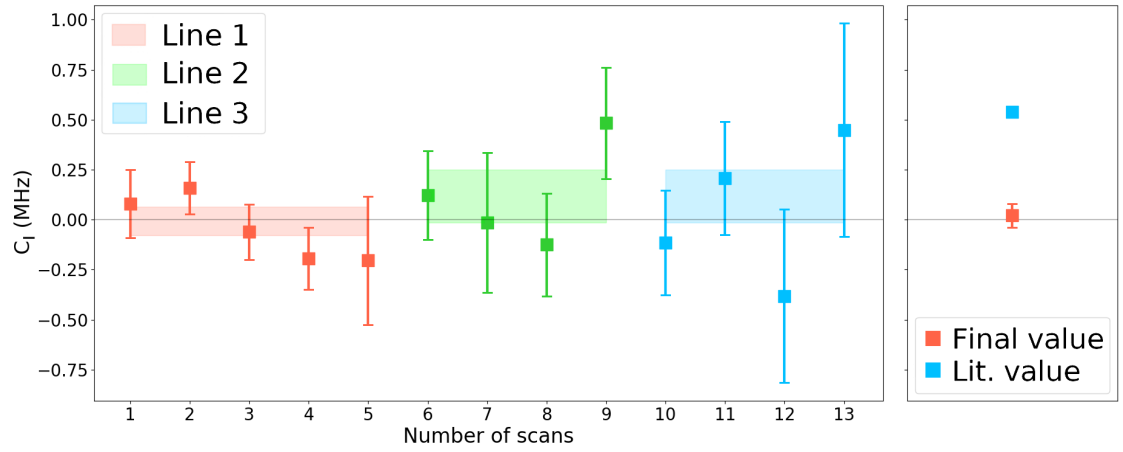

Figure 28: All the values which were extracted for hyperfine constant C_l in this measurement, where the shaded areas represent the weighted mean of each line. On the right, the weighted mean of these 13 scans is compared to the value obtained in [12].

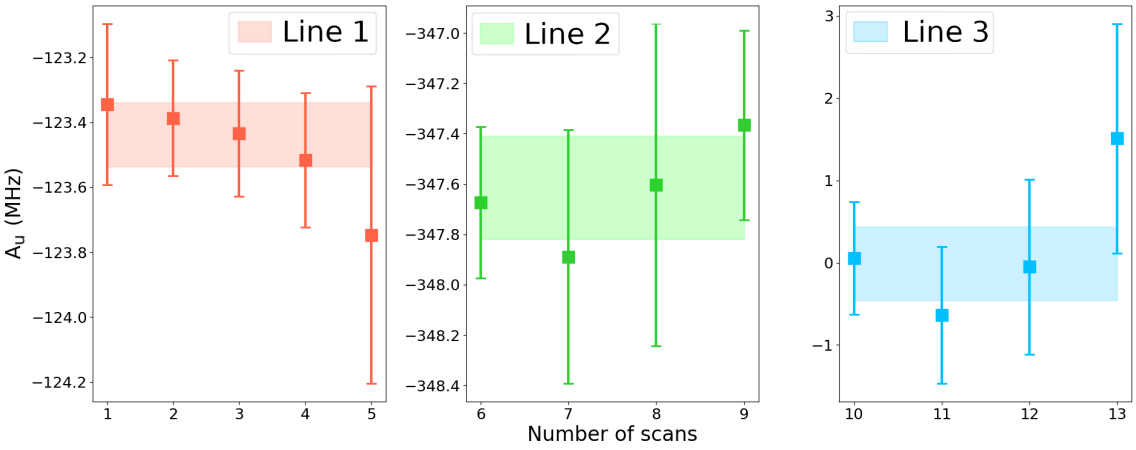

Figure 29: All the values which were extracted for hyperfine constant A_u in this measurement. The shaded areas represent the weighted mean of each line.

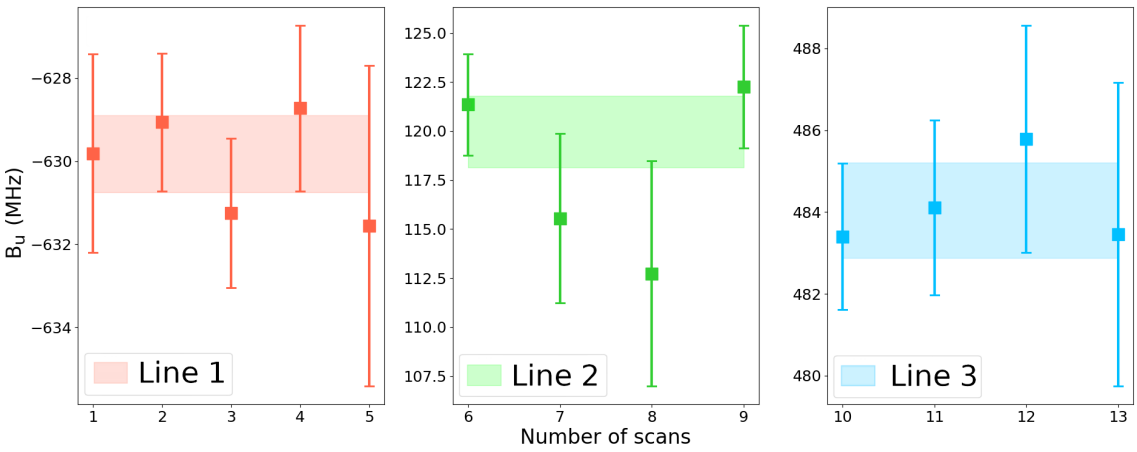

Figure 30: All the values which were extracted for hyperfine constant B_u in this measurement. The shaded areas represent the weighted mean of each line.

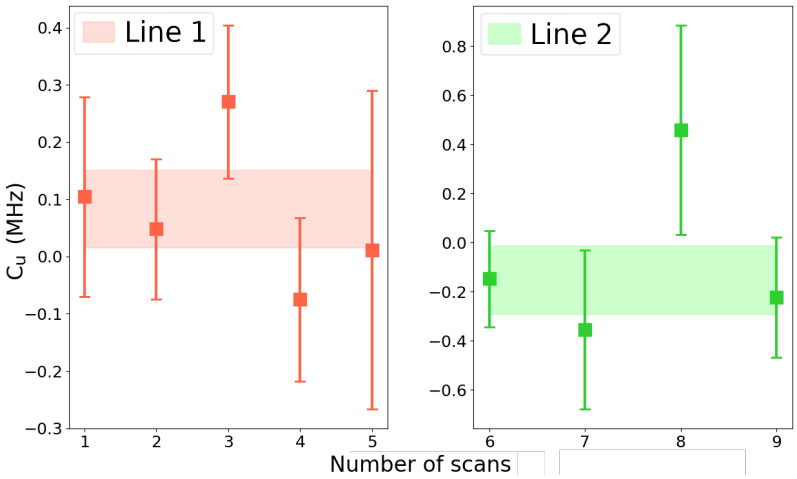

Figure 31: All the values which were extracted for hyperfine constant C_u in this measurement. The shaded areas represent the weighted mean of each line.

3.4 Extraction of the magnetic octupole moment from the experiment

The ratio of C and Ω must be calculated using nuclear theory, and it can then be used to extract the Ω from a measurement of C. As new calculations for this ratio are still currently ongoing, the ratio obtained by [12] was used here. So, Ω is extracted as follows:

$$\frac{C}{\Omega} = \frac{X}{\mu_N \, \mathrm{b}} \qquad \Longleftrightarrow \qquad \Omega = \frac{C}{X} \; \mu_N \, \mathrm{b}, \tag{47}$$

where μ_N is the nuclear magneton, b is barn, and X is the ratio of C and Ω: -15.99 kHz according to [12]. Using this ratio and the value $C = 0.02(6)$ MHz, the octupole moment is determined to be $\Omega = 1.25078 \; \mu_N$ b.

The error for this value is calculated using the propagation of uncertainty [73]:

$$s_f = \sqrt{\left(\frac{\partial f}{\partial x}\right)^2 s_x^2 + \left(\frac{\partial f}{\partial y}\right)^2 s_y^2 + \left(\frac{\partial f}{\partial z}\right)^2 s_z^2 + \cdots}, \tag{48}$$

where s_f is the standard deviation for function f, ∂ is the partial derivative, and $s_{x,y,z,...}$ represents the standard deviation for $x, y, x, ...$ Thus, for octupole moment, the error is calculated as

$$s_\Omega = \sqrt{\left(\frac{1}{X}\right)^2 s_C^2}, \tag{49}$$

where s_C is the uncertainty of the hyperfine constant C. The final value for the experimentally extracted octupole moment from this work is then $\Omega = -1.3(38)\ \mu_N$ b.

3.5 Nuclear theory estimates for the octupole moment

The hyperfine interaction can be represented in terms of the multipole expansion of the field potential when considering the classical electromagnetic interactions between atomic electrons and the nucleus. The magnetic octupole expectation value can thus be calculated using the single-particle model [39]:

$$\frac{\Omega}{\mu_N \langle r^2 \rangle} = \frac{3}{2}\frac{2I-1}{(2I+4)(2I+2)} \times \begin{cases} (I+2)[(I-\frac{3}{2})g_l + g_s], & I = l + \frac{1}{2} \\ (I-1)[(I+\frac{5}{2})g_l - g_s], & I = l - \frac{1}{2} \end{cases} \tag{50}$$

where $\langle r^2 \rangle$ is the mean-squared radius of the valence nucleon orbital, and g_l and g_s are the nuclear g-factors for orbital and spin angular momentum, respectively. The g-factors are defined as [1]

$$g_l = 1, \ \ g_s = \ \ 5.5856912(22) \quad \text{for free protons, and} \tag{51}$$

$$g_l = 0, \ \ g_s = -3.8260837(18) \quad \text{for free neutrons.} \tag{52}$$

However, from the systematics of the magnetic dipole moments, it is known that these g-factor values for free nucleons are not able to provide a sufficient enough approximation for the majority of nuclei. Thus, quenched values are often used and defined as $g_s^q = 0.6\ g_s$. In principle, to obtain values for $\langle r^2 \rangle$, theoretical calculations would be required. As an approximation, data on the total nuclear charge radius was used from [77], where $R = \langle r^2 \rangle^{1/2} = 5.3046(59)$ fm so $\langle r^2 \rangle = 28.1388$ fm^2. This is the mean-squared radius of the valence nucleon, so to make an approximation here the total mean-squared radius is used instead. To obtain the value for only the valence nucleon, nuclear theory calculations will be required but their derivation is currently in progress.

For $^{173}_{70}\mathrm{Yb}_{103}$ ($I = 5/2^-$), according to the single-particle shell model, the unpaired neutron will occupy the $\mathrm{f}_{5/2} = l - 1/2$ orbital as the nuclear spin is of negative parity. Thus, the equation (50) simplifies as

$$\frac{\Omega}{\mu_N \langle r^2 \rangle} = -\frac{g_s}{7} \tag{53}$$

for ytterbium, and results in $\Omega_f = 0.546583$ and $\Omega_q = 0.327950$ for the free and quenched single-particle shell model values, respectively. To convert the result from the equation (53) to the same units with the experimental octupole moment, it must be multiplied with $\mu_N \langle r^2 \rangle$. These values, along with a comparison between all three theoretical models and experimental values used here, are presented in table 8.

The extreme single-particle model described above has limits similar to the Schmidt lines, and does not characterize the octupole moments sufficiently enough. However, by using an axially-symmetric collective model in strong coupling, can the octupole moments of odd-A nuclei with reasonably well-known energy levels be described. To calculate the expectation value of the magnetic octupole moment using the collective model, the following equation can be used

$$\Omega = \frac{2I(2I-1)(2I-2)}{(2I+1)(2I+2)(2I+3)} \times \mu_N \left[\frac{6}{7} g_c \boldsymbol{R}_0^2 + g(3) \frac{\hbar}{w\omega_0} G(I, N, \beta) \right], \tag{54}$$

where g_c depends on the electric charge density and the gradient of mass density, $\boldsymbol{R_0}$ is the radius of a sphere with same volume as the deformed nucleus, $g(3)$ is "total" particle gyromagnetic ratio for the octupole term, $\sqrt{\hbar/m\omega_0}$ is the intrinsic oscillator length, and $G[I, N, \beta]$ is a complicated function of I, N, and β which is given in [78].

3.6 Interpretation of the obtained results

The values obtained for the hyperfine constants are consistent for each scan and also agree with the literature values well regarding to A_l but deviate a little for B_l, as seen in tables 6 and 7. It can also be noted, that for the 390.0855 nm line the values of B_l and C_l seem to vary more compared to other lines, along with the B_u values within that line. This might have something to do with the deviation between the obtained value of B_l and its literature value. However, as the uncertainties are quite large here, at least for C_l the effect would not have been notable and our value is still considerably smaller than the previously obtained one, though here different lines were used. The reason for this deviation is currently unknown.

As it can be seen from figure 32 and table 8, the experimentally determined octupole moment from our measurement agrees with all the theoretical estimates within its error bars which, however, are quite large. Notably, these theory values differ in sign with our

experimental value but as the error on it is large, that is not very significant. The value of C/Ω ratio is by definition essential when extracting the octupole moment. Here the used C/Ω value was taken from [12]. As an additional check of this value, new atomic structure calculations are currently being performed.

The theoretical octupole moment values calculated using the single-particle model included a small approximation in the used mean-squared radius. Instead of the actual mean-squared radius of the valence nucleon orbital, which would require derivation from nuclear theory, the used radius was determined from experimentally obtained total nuclear charge radius. Because of this, the theoretical single-particle values might slightly change later once the theoretical calculations are finished but the difference is not expected to be very notable. All in all, the single-particle model has some limitations when characterizing the octupole moments and hence might not be the optimal model to use. A better option, at least for odd-A nuclei whose energy levels are well-known, is the axially-symmetric collective model where instead of using the nuclear charge radius, the radius is that of a sphere with a volume equivalent to a deformed nucleus.

In the future, more precise experiments, also for different atomic or ionic states, will be very useful for investigating the magnetic octupole moment of ^{173}Yb further.

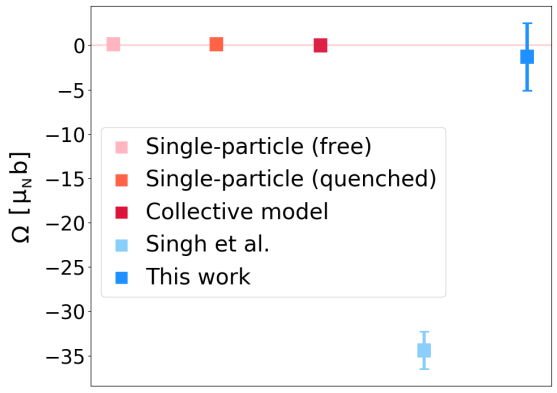

Figure 32: Visual representation of the values from table 8.

Table 8: Comparison of the theoretical and experimental results for the magnetic octupole moment Ω, where μ_N is the nuclear magneton and b is barn (10^{-28}m).

	Ω [μ_N b]
Single-part. (free)	0.1538
Single-part. (quench.)	0.0923
Collective model [78]	0.003
Singh et al. [12]	-34.4(21)
This work	-1.3(38)

4 Study of the radiofrequency excitations with Mg^+

In this chapter, the combination of the collinear LRDR and the MIRACLS method is attempted, and a preliminary test is conducted. Some designs and ideas will be presented to answer the possible challenges and difficulties arising from this kind of project.

4.1 Design of the RF electrode and the new drift tube for an MR-ToF device

This section provides details of the testing of RF penetrability, and the designs for the RF electrodes and modified drift tubes for the MR-ToF device.

The original tube consists of two types of fine conducting mesh to allow the fluorescence photon detection as the PMT is located right above it. This had to be taken into account when designing a new tube to house the desired RF electrodes. Additionally, there is not much extra space near the drift tube area because of the surrounding straylight shield and the three passing support rods, and the electrostatic mirrors and associated cables have high voltage through them. The surrounding area inside the MR-ToF device is shown in figure 37 and the HV cables and drift tube mesh in figure 33.

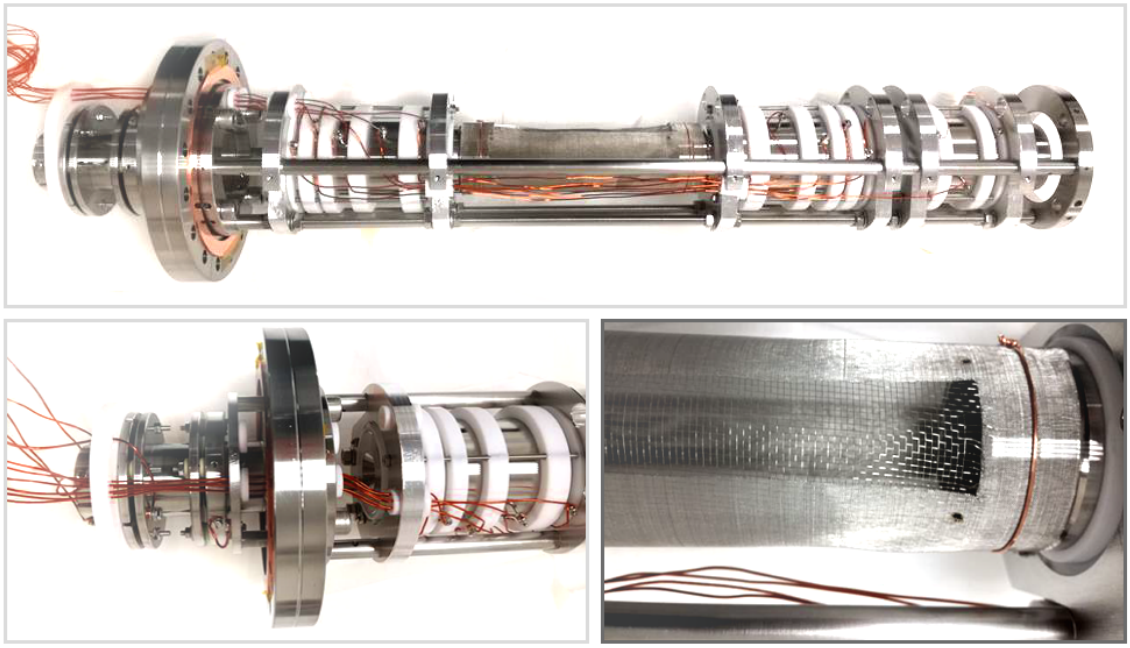

Figure 33: At the top is shown the entire MR-ToF device and the corresponding HV cables. At bottom left is a close-up from the cables leading to the mirror electrodes and at bottom right is a close-up of the two meshes that form the drift tube itself.

4.1.1 RF penetrability through different materials

To understand the behaviour of the RF signal in MR-ToF-like conditions, a simple setup was crafted at JYFL, as seen in figure 35. With this arrangement, the RF penetrability through different materials was tested, mainly through mesh since the original drift tube in the MIRACLS MR-ToF device was constructed of fine mesh, whose purpose was to allow the fluorescence photon detection as the PMT was located right above it. In figure 34 is a picture of the used two meshes: one quite coarse mesh and one very fine mesh. The setup consisted of the DSSG600Pro RF signal generator, 6 dB RF amplifier, 50 Ω terminator, antenna to pick up the signal, coil "electrode" made of copper wire, and an oscilloscope for signal detection. Due to the limited range of the used oscilloscope, the RF generator's signal had to be limited to a couple of MHz to be detected. It was also impossible to pick up any RF signal without the amplifier and a coil-shaped electrode, as the RF signal amplitude was relatively low. The antenna was placed inside a mesh tube to simulate the conditions in the MIRACLS setup. Neither of the used meshes attenuated the RF signal in any detectable way.

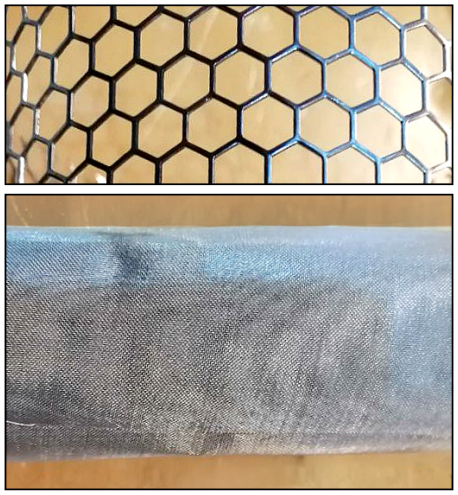

Figure 34: The two types of meshes used in this test, one very coarse and one very fine mesh. The pictures are in scale with each other.

In addition, the RF penetrability was also tested through a steel vacuum tube after noticing it penetrated the coarse mesh and even seven layers of the fine mesh with ease. With the solid vacuum tube, there was no detectable attenuation in the RF signal either. This seemed promising, as picking up the RF did not appear to be a problem.

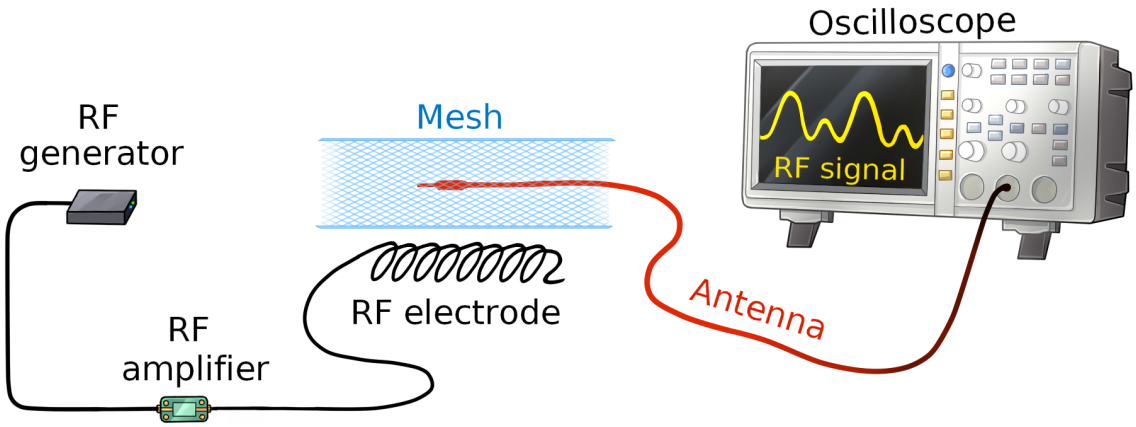

Figure 35: A simplified schematic drawing of the setup where the RF penetrability through two different meshes was tested with a coil-like RF electrode. The circuit was terminated to 50 Ω (not pictured) and RF signal was detected with an oscilloscope.

4.1.2 Modified telescopic drift tube design with conducting mesh

It was decided that a completely new design was needed for the drift tube for it to be able to house the RF electrode. The electrode shape was decided to be kept simple. During other laser-RF measurements at JYFL a small loop was proven to work fine, so that was the plan also here. To be able to slide the drift tube in between the mirror electrode cavities, a design shown in figure 36 was devised. It would consist of two cylinders with slightly different diameters which would partially overlap, thus forming a telescopic design for easy installation. The mesh from the original tube was wanted to be kept as it defined potential in the MR-ToF.

The RF electrode was planned to be placed only in the one end, where the wire would go in and out of the tube through ceramic split bushes. The tube would be long enough to slightly overlap with the mirror cavities, allowing for the tightening with a set of screws through the hole in the tube to the cavity. To achieve magnetic shielding for the RF, it was planned to enclose the whole drift tube system in mu-metal tape (without adhesive), leaving a hole for photon detection. However, as seen in figure 33, there are several HV cables around the area where wrapping was supposed to be done, and the space around the drift tube was very limited having maximum of 2 cm in every direction. Another better option would be to construct the overlapping cylinders out of steel/mu-metal but as mu-metal is easily accidentally magnetized, using it might prove difficult. This shielding was needed as the setup had a magnetically levitated turbopump underneath it, so it was speculated a strong or/and inhomogeneous magnetic field could be generated by it, thus disturbing the RF spectroscopy measurements.

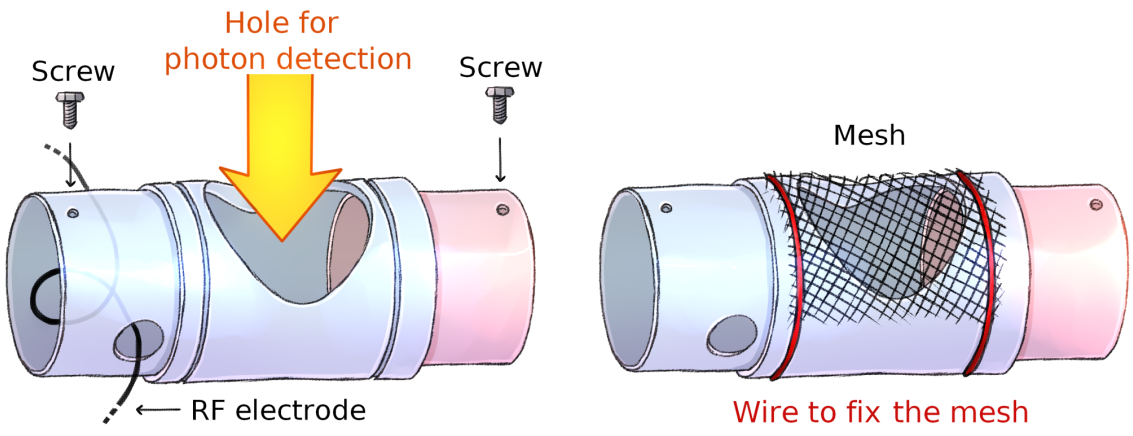

Figure 36: A telescopic drift tube design with two-sized cylinders (blue and red), and a removable mesh and a hole for photon detection. The tube would be fixed around the MR-ToF device's mirror electrode cavities with a set of screws and RF electrode would go in and out from the sides of the tube through a ceramic split bush.

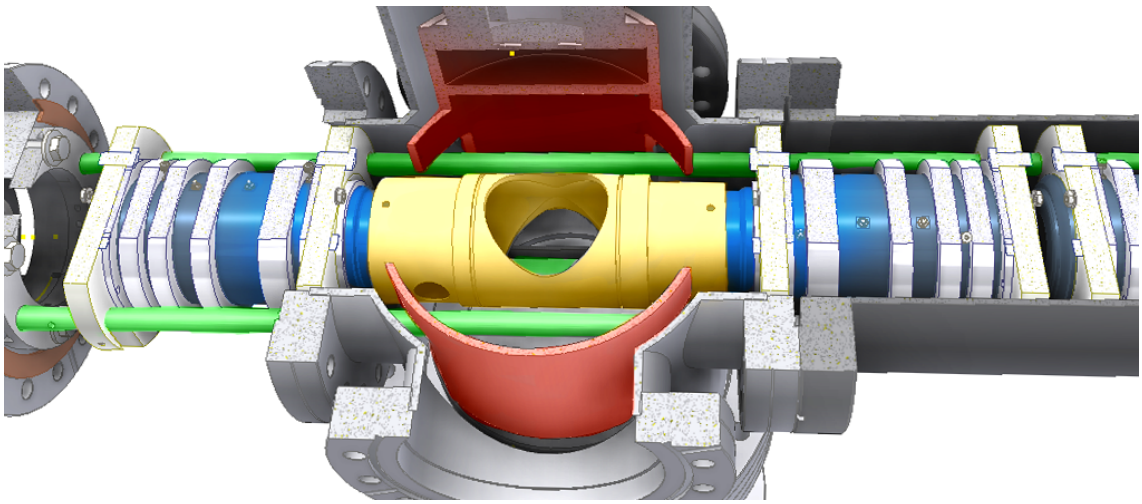

Figure 37: 3D model of the telescopic drift tube inside the MR-ToF device, where the drift tube is yellow, mirror electrode cavities are blue, straylight shield is red, and three support rods are green. In the drift tube design an hole was also added at the bottom for vacuum purposes.

Another important aspect to note were the HV components surrounding the drift tube area. The RF electrode needed to be electrically insulated from the rest of the setup, so a wire with insulating layer would be ideally used (as chapter 4.1.1 detailed, this was not thought to attenuate the RF signal) to avoid accidental contact. One option that was also thought was a fixed electrode inside the drift tube, and an antenna placed on some of the support rods seen in figure 37 to irradiate the electrode. This way the complication arising from the installation of RF electrode on a cylindrical surface could be potentially avoided.

This design was planned to be machined and tested at the MIRACLS setup, but there were some difficulties in getting it machined in time, so it was decided to just test the general idea with a simple RF electrode loop to find out what would be the best way to further develop the drift tube design for the next test phase later. These preliminary tests are detailed in the following chapter. For these tests, I also developed a LabVIEW program to control the RF frequency and power.

4.2 Preliminary tests of the RF excitations at the MIRACLS setup

The first tests concerning the radiofrequency excitations in the MIRACLS MR-ToF device were done at the end of February 2020. For these tests, the DSSG600Pro RF signal generator and 6 dB RF amplifier were used, as previously when testing RF penetrability through different materials in chapter 4.1.1. The RF electrode itself consisted of a bared wire loop (approximate size of 8x3 cm) which was placed inside the vacuum chamber, but outside the MR-ToF straylight shield. The straylight shield had been previously installed to

reduce the background photon counts. This simplified test setup was used to avoid technical complications, such as isolating the electrode from the rest of the setup, disturbing electric fields and voltage switching complications, associated with placing the RF electrode inside the actual drift tube. A simplified schematic drawing of this placement and the relevant measurement setup is illustrated in figure 38.

BNC and SMA cables were used to connect the RF electrode and the RF generator outside the vacuum. A LabVIEW program I wrote at JYFL was integrated into the existing MIRACLS laser scanning program and was proven to work as expected. After optimizing the ion beam transport and the operational parameters of the MR-ToF, the first resonances on ^{24,25,26}Mg could be obtained.

Once this was achieved, an RF signal with frequency of 1788.763 MHz was applied. However, after several measurements, no evidence of an enhancement in the photon rate due to the RF excitation could be observed, as seen in figure 39. In this figure, there are bursts of photons when the ions are in front of the PMT and then the signal drops due to the optical pumping into the other HFS level. The purpose of the RF signal is to excite the ions back to the HFS level of interest as explained in figure 13 and therefore it was expected that the red (RF on) signal's height wouldn't have decayed away as fast as it did.

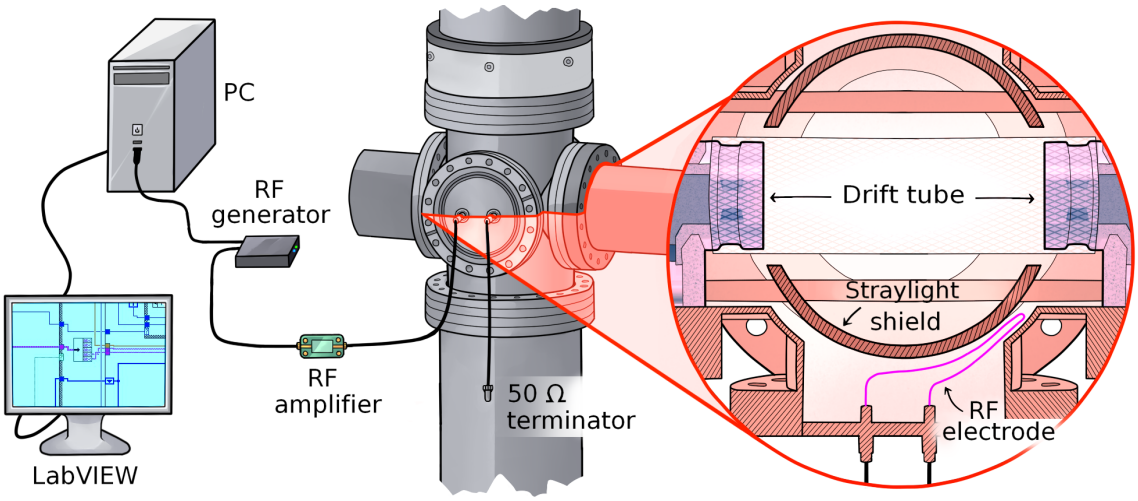

Figure 38: A simple schemetic drawing of the setup and RF electrode (pink) placement at the MIRACLS setup, where controlling of the RF was done with a LabVIEW program integrated into the existing laser frequency scanning program.

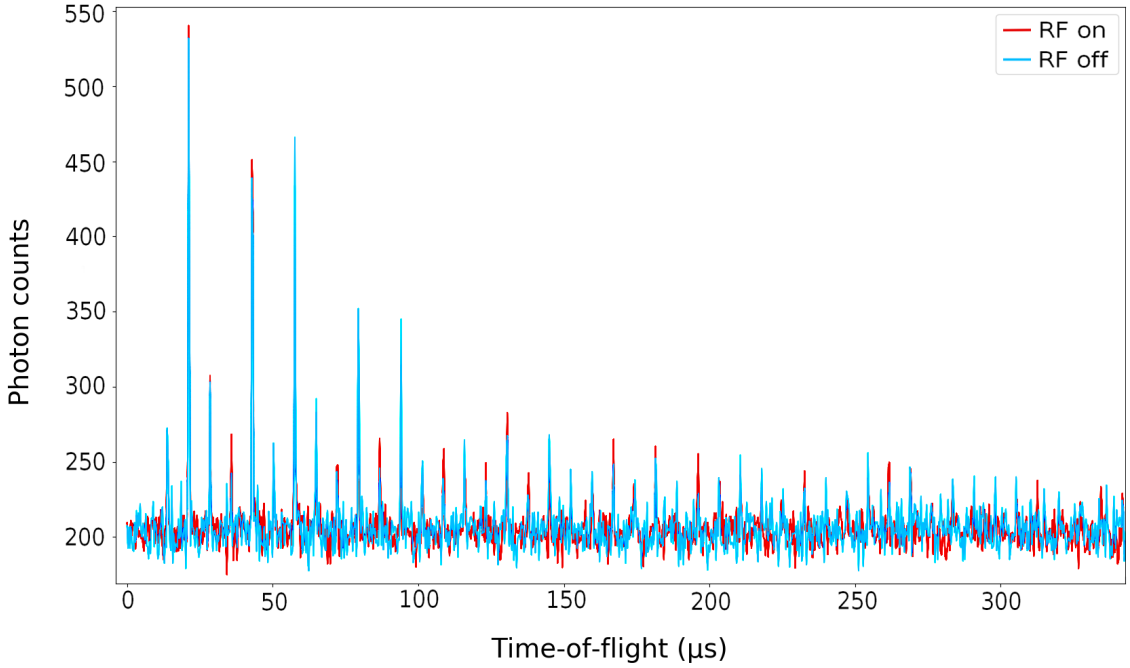

Figure 39: Presented here is the the sum on 4 measurements with RF on (red) and sum of 4 measurements with RF off (blue), with RF frequency of 1788.763 MHz. As it can be seen, there seems to be no clear RF enhancement visible.

Various additional checks and tests were performed. The loading time of the MR-ToF was increased to enhance the signal strength. The RF frequency was changed to a Doppler-shifted value. After still having not observed any signal, the RF generator and amplifier were replaced by a Rohde & Schwarz triggerable generator, which allowed for a frequency-modulation of the RF signal. This was done in case the exact RF frequency was missed or an external magnetic field had shifted the transition frequency. The RF output was triggered on after 300 μs from switching down the lift 2. The results from the measurements with the modulated RF signal and 300 μs triggering can be seen in figure 40.

An additional step that could have been taken would have been to modulate the laser intensity using a Pockels cell, but there was no time to investigate this option. Another option would have been to take out the whole RF electrode in hopes of trying to make it better, which would have required breaking the vacuum, all while also having to impedance-match it to 50 Ω. Furthermore, a larger-gain amplifier might have helped in case the RF-field was too small to induce significant excitations. However, no such amplifier was available at the time.

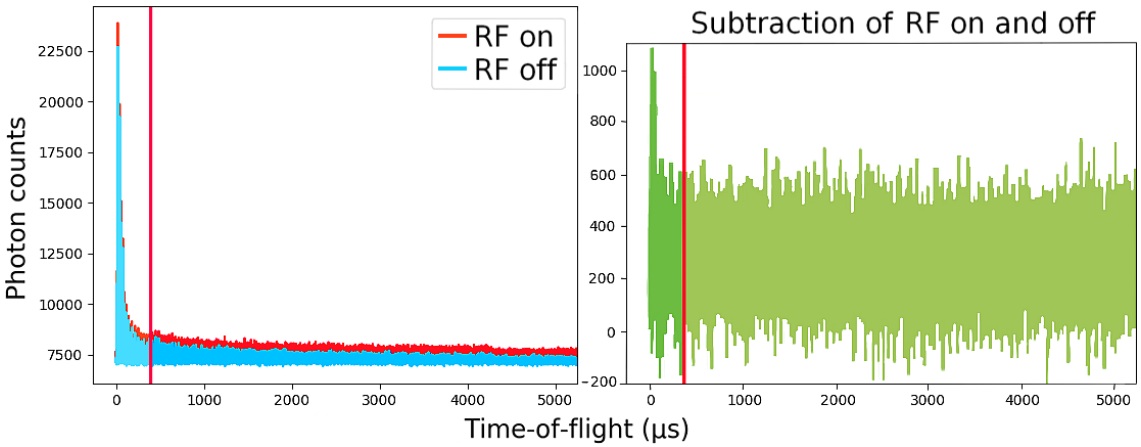

Figure 40: Here the RF was triggered exactly 300 μs (red line) after switching lift 2 down while also modulating the RF signal over the range of 1.5 MHz to cover all the magnetic substates. On the right, the green is the subtraction between the RF on and off measurements. There's a small offset in the background, most likely due to the laser power dropping after two hours of measuring. However, it seems there is no signal enhancement at 300 μs as it was expected.

4.2.1 Laser cooling as a detection method

As an alternative approach to realizing in-trap RF spectroscopy, an RF signal was applied to one of the segments of the linear Paul trap (see figure 5) which cools and bunches the ions prior to their injection into the MR-ToF. The CW laser beam was, in this case, directed also into the Paul trap. For even-even isotopes, tuning the frequency of the laser to a few 100 MHz below the transition frequency leads to laser cooling, which dampens the ion motion in all directions.

When the laser frequency is tuned slightly below the resonant frequency of the ion, it absorbs more photons when it moves towards the laser beam than it does when moving away from it due to the Doppler effect. In the frame of the moving ion, when a counter-propagating laser beam with a frequency below the ion's resonance frequency is applied, it leads to a Doppler shift that increases the frequency of the laser beam as observed by the ion. This Doppler shift then causes the laser light to come closer to resonance with the ion, and thus increases the rate of absorption from the beam. When these ions de-excite, they emit photons isotropically, thus resulting in a net momentum kick which slows down the ions. To cool the ions' motion in all three directions, the radiative force must have a component along with the direction corresponding to each degree of freedom, that is the laser beam must not get through the trap along any of the axes of symmetry. Since the ions will return from the excited hyperfine state to the ground-state after a time of some nanoseconds, this absorption-emission process is repeated very quickly and results in effective cooling of the ions. [40, 79]

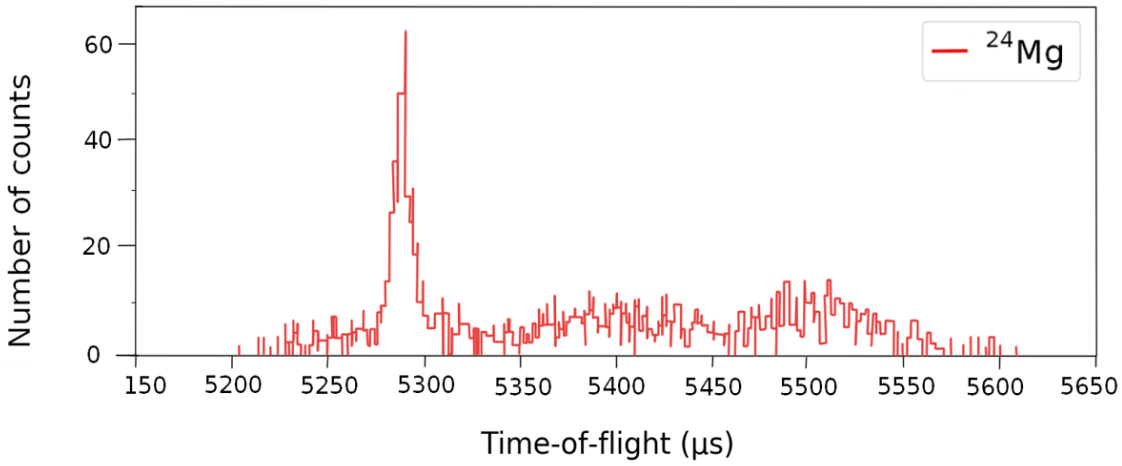

Figure 41: The ^{24}Mg cooling peak is visible with 770 counts in the whole peak, measured using 220 sweeps and 50 ms cooling time. The signal was already very strong without applying any RF.

At first, the laser-cooled signal was verified for ^{24}Mg and ^{26}Mg. The first segment of the Paul trap was not used since it serves as the RF antenna for the RF spectroscopy tests on ^{25}Mg. A strong signal was found with 50 ms of laser cooling, showing 770 counts in 220 sweeps in the cooling peak of ^{24}Mg, as seen in figure 41. For ^{25}Mg, detection of the RF resonance here relies on monitoring the bunch length when tuning the laser frequency to the cooling frequency for ^{25}Mg. In absence of an RF excitation which brings atoms back into the desired hyperfine level, ^{25}Mg cannot be laser-cooled due to optical pumping from one hyperfine level to the other one.

The presence of hyperfine structure enables multiple ways to emit a photon from the upper state which leads to a de-excition into a dark state and therefore removing it from the cooling process. In case of ^{24}Mg, after a few cycles, almost every ion would have been de-excited into the other hyperfine level - practically stopping the absorption and emission of the photons. By introducing an RF excitation, those ions would then be re-excited back to the correct hyperfine levels, continuing the absorption and thus hopefully resulting in laser cooling.

The advantages of this approach should be many: a longer interaction time with the RF is easily achievable. The ions occupy a smaller region in space, which helps to avoid the possible inhomogeneities in the magnetic field. Introducing the RF field also did not require breaking vacuum, since the RF could be easily applied to one electrode in the trap - crucially, allowing the tests to be carried on right away without making other changes to the setup which would have taken several days.

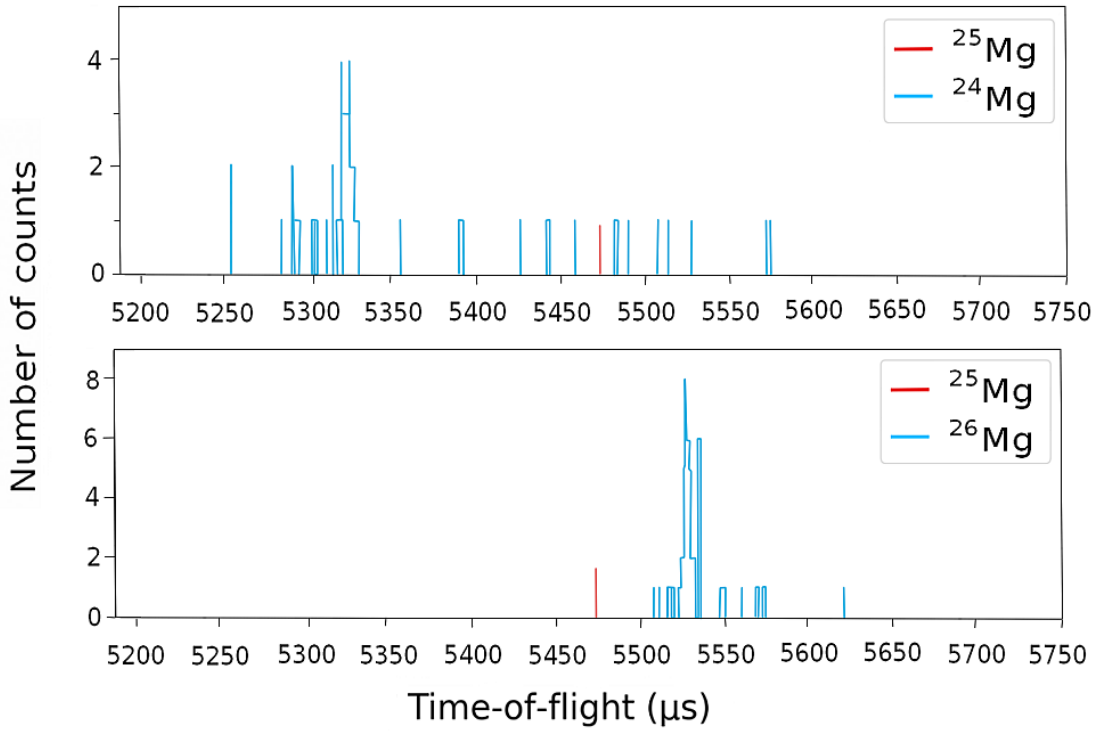

Figure 42: The laser cooled peaks of ^{24}Mg (upper) and ^{26}Mg (lower) can be seen in blue, and red colour indicates the place where ^{25}Mg peak should have shown up. As it can be seen, the count rate was very low and ^{25}Mg was conspicuously absent.

Now the RF generator was floated to the DC voltage of the Paul trap's segment and lasers were tuned to cool ^{25}Mg after a reference measurements on ^{24}Mg and ^{26}Mg to calibrate the time-of-flight. After a very long measurement with a low count rate, where the RF frequency was tuned to the resonance frequency of 1778 MHz, no signal was observed at the time-of-flight of ^{25}Mg, as seen in figure 42.

4.3 Redesigned drift tube with a coaxial geometry

From the preliminary tests, it became clear that a more complex drift tube modifications are needed in order to obtain a detectable RF signal and cause the excitations. It has been previously demonstrated in collinear laser-radiofrequency literature [80] that coaxial geometry is often used, thus it could be adapted to the MR-ToF device as well. This could be done as follows: the drift tube itself would serve as the outer part of the coaxial electrode geometry, and an inner conductor would be added along the whole length of the drift tube, as envisioned in figure 43. This just a rough idea though, as there are numerous aspects to this design that need careful consideration and planning, so they are not discussed in this thesis.

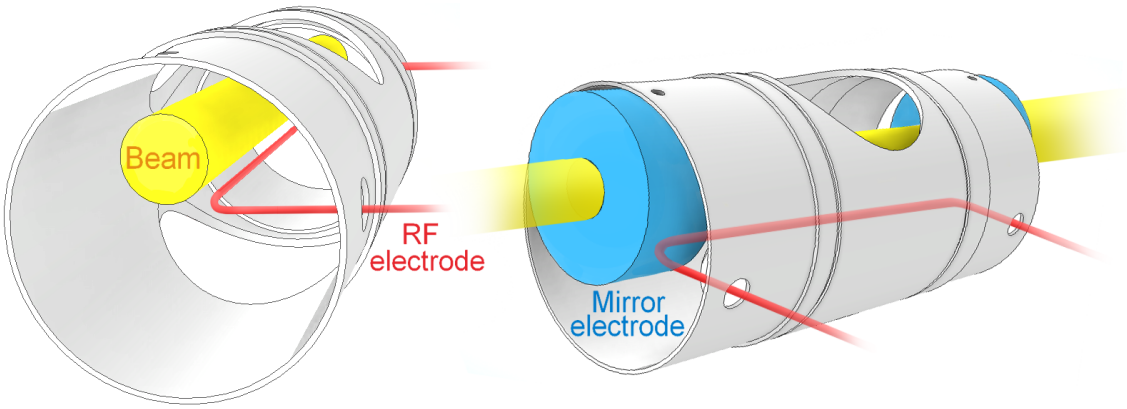

Figure 43: A rough idea for the coaxial drift tube, where the RF electrode (red) is located in the centre of the tube and the ion beam (yellow) goes through slightly off axis. The drift tube would lie on the mirror electrode cavities (blue) and be fixed from above with a set of screws as detailed in chapter 4.1.2.

For example, here the diameter of the drift tube had to be enlarged to be able to overlap with the mirror electrode cavities while also keeping the RF transmission line at the centre of the drift tube to achieve proper impedance matching. Here the beam diameter was assumed to be 14 mm, and the RF line had to be placed under the beam to avoid blocking the PMT. The resulting large gap between the drift tube and the mirror electrodes also needs to be covered somehow, maybe using the mu-metal tape would be an option here. The RF could be guided through the holes in the tube wall via e.g. ceramic split bushes as envisioned already in chapter 4.1.2. However, there is one clear flaw rising from this design as-is: the drift tube diameter is now too large to fit inside the straylight shield in the setup and it also overlaps with the support rods, as seen in figure 44. This problem can likely be resolved with a more elaborate design but will not be explored further here.

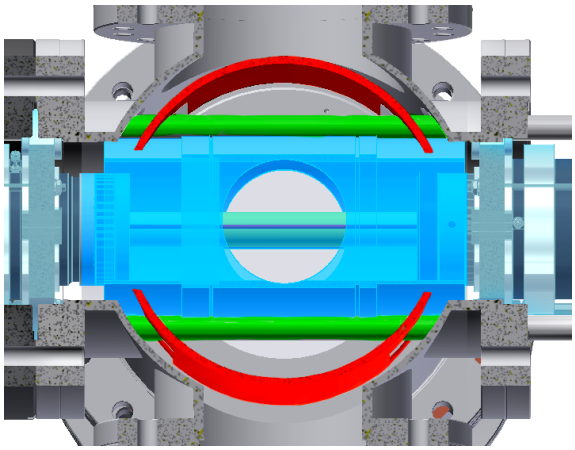

Figure 44: Shown here is the problem caused by the larger diameter of the coaxial drift tube (blue): it overlaps with the straylight shield (red) and the support rods (green).

Usually, in designs like these, the coaxial transmission line is quite long which results in some advantages such as a more uniform magnetic field in the entire RF interaction region. Additionally, the Earth's magnetic field could be minimized using three pairs of Helmholz coils, or carefully placed mu-metal shielding [80]. The former likely would not fit in the setup, which leaves only the mu-metal option. Mu-metal would be a great

candidate for magnetic shielding due to its highly permeable properties. To shield from high-frequency (> 100 kHz) RF fields, materials such as copper, aluminium, and metallized plastics could be used.

However, due to the current situation with the pandemic and the arisen technical difficulties in the integration of the RF, no detailed study of the feasibility of this design was undertaken but is planned for the future.

4.4 Conclusions about the laser-RF method in an MR-ToF

Due to the pandemic situation, final tests with a fully constructed drift tube design were not possible so it remains unclear if this would have worked. However, the RF integration into the MR-ToF device was deemed a more complicated task than initially thought, so perhaps some simulations about the RF field in the MR-ToF-like conditions would also prove beneficial in the future. The MR-ToF could also be used in mirror switching mode instead of the in-trap potential lift to potentially help with the technical complications associated with the voltage switching in the drift tube. To make sure the RF-field was sufficient enough, a large-gain amplifier should also be tested along with the suitably modified drift tube.

As it has been previously described in the literature, a coaxial drift tube geometry might also be the best option here, since it would provide a more uniform magnetic field in the RF interaction region. The effect from Earth's magnetic field also needs to be considered, and the RF region appropriately shielded from it. Shielding this region fully might prove somewhat challenging, as the optical detection region with the PMT is located right above the centre of the drift tube and thus cannot be blocked.

As demonstrated in [37, 38], the use of RF spectroscopy is possible in at least Paul and Penning traps, and that it is possible for complicated species such as singly-charged europium even when the species are not cooled beyond simple buffer-gas cooling. Many of the advantages of working in these traps will hopefully also translate into the use of the MR-ToF device in the future, opening new exciting possibilities for high precision spectroscopy.

5 Discussion

Currently, there are only 18 elements with an experimentally measured magnetic octupole moment. More measurements for a larger variety of elements would thus prove beneficial to understand the higher-order effects in different nuclei. A very large value of the hyperfine C constant of ^{173}Yb reported in the literature was interesting for two reasons. Firstly, if correct, it would indicate a severe problem in our understanding of the magnetic octupole moments. Secondly, the value is such that experimental studies on radioactive ytterbium isotopes would have been possible with currently available methods at the IGISOL. The measurements presented in this thesis do not confirm the strikingly large value of the ^{173}Yb octupole moment reported in the literature but instead yield a value which is zero within the experimental uncertainty, and closer to the typical values obtained for other elements. This work shows that higher-precision methods will be needed for further octupole moment studies in the future.

This work brings the experimental value in agreement with both free and quenched single-particle model, and the collective model. This thesis will, in any case, serve as a motivation for future octupole measurements and theoretical investigations for stable and radioactive elements. From the analysis process, it also can be concluded that careful analysis and peak constraining are crucial for the final values of the hyperfine constants, as they can have a significant effect on especially for the octupole constant if not done in a thorough manner. No earlier measurements of the upper state hyperfine constants A_{u}, B_{u}, and C_{u} of the lines used here were found in the literature. This thesis thus provides the first values for these constants as well.

This thesis has also made the first steps in a bigger project which aims to implement the laser-RF techniques in an MR-TOF device. While no positive results could be obtained, several important lessons were learnt while constructing and using the first rudimentary setup. It is clear, that the combination of MIRACLS and LRDR needs more work and there are several complications which need to be addressed in the future. Some simulations could be useful here, and it would help to know if there is some magnetic field present inside the MR-ToF as this would induce a wide range of splittings in the m_F levels which cannot be easily covered. If the combination of these two methods succeeds in the future, it will undoubtedly have great potential to improve our understanding of the atomic nucleus and its properties due to the superior resolution typical to LRDR. The more precise determination of the hyperfine constants will enable measurements of e.g. the hyperfine anomalies or the higher-order nuclear moments. All things considered, perhaps it would be most effective to construct an entirely new MR-ToF with the RF excitation region in mind in order to avoid the multiple complications encountered here. Nevertheless, many obstacles need to be overcome before a successful result is obtained, as is often the case when trying new things.

References

[1] Kenneth S. Krane. *Introductory Nuclear Physics*. Wiley, 1988.

[2] R. Paschotta. Lasers: Understanding the basics. *RP. Photonics Encyclopedia*. `https://www.photonics.com/Articles/Lasers_Understanding_the_Basics/a25161`, accessed 15.5.2020.

[3] H. J. Andra. Proceedings of the Fourth International Conference on Atomic Physics. *Atomic Physics*, 4:635, 1975.

[4] William H. Wing, George A. Ruff, Willis E. Lamb, and Joseph J. Spezeski. Observation of the infrared spectrum of the hydrogen molecular ion HD^+. *Phys. Rev. Lett.*, 36:1488–1491, 1976.

[5] S.L. Kaufman. *High-resolution laser spectroscopy in fast beams*. Optics Communications, 17(3):309 – 312, 1976.

[6] R. Neugart, J. Billowes, M. L. Bissell, and K. Blaum et al. Collinear laser spectroscopy at ISOLDE: new methods and highlights. *Journal of Physics G: Nuclear and Particle Physics*, 44(6):064002, 2017.

[7] T.E. Cocolios, R.P. de Groote, J. Billowes, and M.L. Bissell et al. High-resolution laser spectroscopy with the Collinear Resonance Ionisation Spectroscopy (CRIS) experiment at CERN-ISOLDE. *Nuclear Instruments and Methods in Physics Research Section B: Beam Interactions with Materials and Atoms*, 376:284 – 287, 2016.

[8] Simon Sels, P. Fischer, and H. Heylen et al. First steps in the development of the multi ion reflection apparatus for collinear laser spectroscopy. *Nuclear Instruments and Methods in Physics Research Section B: Beam Interactions with Materials and Atoms*, 2019.

[9] T.J. Mertzimekis, K. Stamou, and A. Psaltis. An online database of nuclear electromagnetic moments. *Nuclear Instruments and Methods in Physics Research Section A: Accelerators, Spectrometers, Detectors and Associated Equipment*, 807:56–60, 2016.

[10] Vladislav Gerginov, Andrei Derevianko, and Carol E. Tanner. Observation of the nuclear magnetic octupole moment of ^{133}Cs. *Phys. Rev. Lett.*, 91:072501, 2003.

[11] Nicholas C. Lewty, Boon Leng Chuah, Radu Cazan, B. K. Sahoo, and M. D. Barrett. Spectroscopy on a single trapped $^{137}Ba^+$ ion for nuclear magnetic octupole moment determination. *Opt. Express*, 20(19):21379–21384, 2012.

[12] Alok K. Singh, D. Angom, and Vasant Natarajan. Observation of the nuclear mag-

netic octupole moment of ^{173}Yb from precise measurements of the hyperfine structure in the $^3P_2$ state. *Phys. Rev. A*, 87:012512, 2013.

[13] P. Campbell, I.D. Moore, and M.R. Pearson. Laser spectroscopy for nuclear structure physics. *Progress in Particle and Nuclear Physics*, 86:127 – 180, 2016.

[14] R. P. de Groote, J. Moreno, J. Dobaczewski, I. Moore, M. Reponen, B. K. Sahoo, and C. Yuan. Measurement of an unusually large magnetic octupole moment in ^{45}Sc challenges state-of-the-art nuclear-structure theory. 2020.

[15] W. J. Childs, O. Poulsen, L. S. Goodman, and H. Crosswhite. Laser-rf double-resonance studies of the hyperfine structure of ^{51}V. *Phys. Rev. A*, 19:168–176, 1979.

[16] R. T. Daly and J. H. Holloway. Nuclear magnetic octupole moments of the stable gallium isotopes. *Phys. Rev.*, 96:539–540, 1954.

[17] Howard Howland Brown and John G. King. Hyperfine structure and octopole interaction in stable bromine isotopes. *Phys. Rev.*, 142:53–59, 1966.

[18] W. L. Faust and L. Y. Chow Chiu. Hyperfine structure of the metastable $(4p)^5(5s)^3p_2$ state of $_{36}$Kr^{83}. *Phys. Rev.*, 129:1214–1220, 1963.

[19] T. G. Eck and P. Kusch. Hfs of the $5^2p_{\frac{3}{2}}$ state of In^{115} and In^{113}: Octupole interactions in the stable isotopes of indium. *Phys. Rev.*, 106:958–964, 1957.

[20] V. Jaccarino, J. G. King, R. A. Satten, and H. H. Stroke. Hyperfine structure of I^{127}. nuclear magnetic octupole moment. *Phys. Rev.*, 94:1798–1799, 1954.

[21] M. J. Amoruso and W. R. Johnson. Relativistic one-electron calculations of shielded atomic hyperfine constants. *Phys. Rev. A*, 3:6–12, 1971.

[22] W. L. Faust and M. N. McDermott. Hyperfine structure of the $(5p)^5(6s)^3p_2$ state of $_{54}$Xe^{129} and $_{54}$Xe^{131}. *Phys. Rev.*, 123:198–204, 1961.

[23] Vladislav Gerginov, Andrei Derevianko, and Carol E. Tanner. Observation of the nuclear magnetic octupole moment of ^{133}Cs. *Phys. Rev. Lett.*, 91:072501, 2003.

[24] Nicholas C. Lewty, Boon Leng Chuah, Radu Cazan, Murray D. Barrett, and B. K. Sahoo. Experimental determination of the nuclear magnetic octupole moment of ^{137}Ba$^+$ ion. *Phys. Rev. A*, 88:012518, 2013.

[25] W. J. Childs. M1, e2, and m3 hyperfine structure and nuclear moment ratios for ^{151,153}Eu. *Phys. Rev. A*, 44:1523–1530, 1991.

[26] P. J. Unsworth. Nuclear dipole, quadrupole and octupole moments of ^{155}Gd by

atomic beam magnetic resonance. *Journal of Physics B: Atomic and Molecular Physics*, 2(1):122–133, 1969.

[27] T. Brenner, S. Büttgenbach, W. Rupprecht, and F. Träber. Nuclear moments of the low abundant natural isotope ^{176}Lu and hyperfine anomalies in the lutetium isotopes. *Nuclear Physics A*, 440(3):407 – 423, 1985.

[28] W. G. Jin, M. Wakasugi, T. T. Inamura, T. Murayama, T. Wakui, H. Katsuragawa, T. Ariga, T. Ishizuka, and I. Sugai. Laser-rf double-resonance spectroscopy of ^{177,179}Hf. *Phys. Rev. A*, 52:157–164, 1995.

[29] Arthur G. Blachman, Donald A. Landman, and Allen Lurio. Hyperfine structure and g_J value of the $^2d_{\frac{3}{2}}$ and of the $^4f_{\frac{9}{2}}$ states of Au^{197}. *Phys. Rev.*, 161:60–67, 1967.

[30] Mark N. McDermott and William L. Lichten. Hyperfine structure of the 6^3p_2 state of $_{80}$Hg^{199} and $_{80}$Hg^{201}. properties of metastable states of mercury. *Phys. Rev.*, 119:134–143, 1960.

[31] Donald A. Landman and Allen Lurio. Hyperfine structure of the $(6p)^3$ configuration of Bi^{209}. *Phys. Rev. A*, 1:1330–1338, 1970.

[32] Robert J. Hull and Gilbert O. Brink. Hyperfine structure of ^{209}Bi. *Physical Review A*, 1(3):685, 1970.

[33] C. M. Olsmats, S. Axensten, and G. Liljegren. Hyperfine structure investigation of ^{205}Po and ^{207}Po. *Arkiv Fysik*, 19, 1961.

[34] Gladys H. Fuller. Nuclear spins and moments. *Journal of Physical and Chemical Reference Data*, 5(4):835–1092, 1976.

[35] I. I. Rabi, J. R. Zacharias, S. Millman, and P. Kusch. A new method of measuring nuclear magnetic moment. *Phys. Rev.*, 53:318–318, Feb 1938.

[36] W. J. Childs. *Overview of Laser-Radiofrequency Double-Resonance Studies of Atomic, Molecular, and Ionic Beams*. PHYSICS REPORTS (Review Section of Physics Letters) 211. No. 3(1992) 113—165., 1992.

[37] O. Becker, K. Enders, G. Werth, and J. Dembczynski. Hyperfine-structure measurements of the ^{151,153}Eu$^+$ ground state. *Phys. Rev. A*, 48:3546–3554, Nov 1993.

[38] Trapp, S., Tommaseo, G., Revalde, G., Stachowska, E., Szawiola, G., and Werth, G. Ion trap nuclear resonance on 151eu+. *Eur. Phys. J. D*, 26(3):237–244, 2003.

[39] Charles Schwartz. Theory of hyperfine structure. *Phys. Rev.*, 97:380–395, Jan 1955.

[40] C.J. Foot. *Atomic Physics*. Oxford Master Series in Physics, OUP Oxford, 2005.

[41] G. Drake. *Springer handbook of Atomic, molecular and Optical physics*. Springer, 2005.

[42] M.L. Bissell et al. Model independent determination of the spin of the ^{180}Ta naturally occurring isomer. *Phys. Rev. C*, 74:047301, 2006.

[43] C. Schulz, E. Arnold, W. Borchers, W. Neu, R. Neugart, M. Neuroth, E. W. Otten, and et al. Resonance ionization spectroscopy on a fast atomic ytterbium beam. *Journal of Physics B: Atomic, Molecular and Optical Physics*, 24(22):4831–4844, 1991.

[44] Jenny E. Rosenthal and G. Breit. The isotope shift in hyperfine structure. *Phys. Rev.*, 41:459–470, 1932.

[45] Aage Bohr and V. F. Weisskopf. The influence of nuclear structure on the hyperfine structure of heavy elements. *Phys. Rev.*, 77:94–98, 1950.

[46] J.R. Persson. Table of hyperfine anomaly in atomic systems. *Atomic Data and Nuclear Data Tables*, 99(1):62–68, Jan 2013.

[47] Daniel E. Murnick and Michael S. Feld. Applications of lasers to nuclear physics. *Ann. Rev. Nucl. Part. Sci. 29: 41 1-54*, 1979.

[48] Wolfgang Paul. Electromagnetic traps for charged and neutral particles. *Rev. Mod. Phys.*, 62:531–540, 1990.

[49] F. Herfurth and H. K. Blaum. *Trapped Charged Particles and Fundamental Interactions*. Springer, Berlin Heidelberg, 2008.

[50] Donald J. Douglas, Aaron J. Frank, and Dunmin Mao. Linear ion traps in mass spectrometry. *Mass Spectrometry Reviews*, 24(1):1–29, 2005.

[51] V.N. Gheorghe F.G. Major and G. Werth. Charged particle traps: Physics and techniques of charged particle field confinement. *Springer Series on Atomic, Optical, and Plasma Physics*, 2006.

[52] D. Zajfman, O. Heber, L. Vejby-Christensen, I. Ben-Itzhak, M. Rappaport, R. Fishman, and M. Dahan. Electrostatic bottle for long-time storage of fast ion beams. *Phys. Rev. A*, 55:R1577–R1580, 1997.

[53] F. Wienholtz, S. Kreim, M. Rosenbusch, L. Schweikhard, and R.N. Wolf. Mass-selective ion ejection from multi-reflection time-of-flight devices via a pulsed in-trap lift. *International Journal of Mass Spectrometry*, 421:285 – 293, 2017.

[54] Wolfgang Plaß, T. Dickel, and Christoph Scheidenberger. Multiple-reflection time-of-flight mass spectrometry. *International Journal of Mass Spectrometry*, 349-350:134–144, 2013.

[55] Klaus Blaum, Jens Dilling, and Wilfried Nörtershäuser. Precision atomic physics techniques for nuclear physics with radioactive beams. *Physica Scripta Volume T*, T152, 10 2012.

[56] B. Cheal and K. T. Flanagan. TOPICAL REVIEW: Progress in laser spectroscopy at radioactive ion beam facilities. *Journal of Physics G Nuclear Physics*, 37(11):113101, November 2010.

[57] W. Nörtershäuser and C. Geppert. Nuclear Charge Radii of Light Elements and Recent Developments in Collinear Laser Spectroscopy. . *Scheidenberger C., Pfützner M. (eds) The Euroschool on Exotic Beams, Vol. IV. Lecture Notes in Physics, vol 879*, 2014.

[58] R. Paschotta. *Encyclopedia of Laser Physics and Technology*. 1. edition , Wiley-VCH, ISBN 978-3-527-40828-3, 2008.

[59] P.F. Bernath. *Spectra of Atoms and Molecules*. Oxford University Press, 2016.

[60] J.J. Olivero and R.L. Longbothum. Empirical fits to the Voigt line width: A brief review. *Journal of Quantitative Spectroscopy and Radiative Transfer*, 17(2):233 – 236, 1977.

[61] Blaum K. Nörtershäuser W. Schweikhard L. Wienholtz F. Malbrunot-Ettenauer, S. Benchmarking of a multi ion reflection apparatus for collinear laser spectroscopy of radionuclides. *Letter of Intent to the ISOLDE and Neutron Time-of-Flight Committee*, 2017.

[62] R. P. de Groote, Jon Billowes, Corry L Binnersley, Mark L. Bissell, Thomas Elias Cocolios, T. Day Goodacre, Gregory James Farooq-Smith, and et al. Measurement and microscopic description of odd–even staggering of charge radii of exotic copper isotopes. *Nature Physics*, pages 1–5, 2020.

[63] Wolfgang Demtröder. *Laser Spectroscopy: Vol 2: Experimental Techniques*. Springer, 4 edition, 2008.

[64] A. Sen, L. S. Goodman, and W. J. Childs. Collinear laser and slow-ion-beam apparatus for high-precision laser-rf double-resonance spectroscopy. *Rev. Sci. Instrum.; (United States)*, 59:1, 1 1988.

[65] Tommi Eronen, V. Kolhinen, V.-V Elomaa, Dmitry Gorelov, Ulrike Hager, and et al. JYFLTRAP: a Penning trap for precision mass spectroscopy and isobaric purification. *Three Decades of Research Using IGISOL Technique at the University of Jyväskylä*, pages 61–81, 2014.

[66] Bradley Cheal and D. Forest. Collinear laser spectroscopy at the new IGISOL-4 facility. *Hyperfine Interactions*, 223, 2012.

[67] Yuri P. Raizer. *Gas Discharge Physics*. Springer, 2001.

[68] R.P. de Groote, A. de Roubin, P. Campbell, B. Cheal, C.S. Devlin, T. Eronen, S. Geldhof, and I.D. Moore et al. Upgrades to the collinear laser spectroscopy experiment at the IGISOL. *Nuclear Instruments and Methods in Physics Research Section B: Beam Interactions with Materials and Atoms*, 463:437 – 440, 2020.

[69] A.R. Vernon, J. Billowes, C.L. Binnersley, M.L. Bissell, and T.E. Cocolios et al. Simulation of the relative atomic populations of elements $1 < Z < 89$ following charge exchange tested with collinear resonance ionization spectroscopy of indium. *Spectrochimica Acta Part B: Atomic Spectroscopy*, 153:61 – 83, 2019.

[70] Sirah. *Datasheet Matisse 2 TS*. `http://www.sirah.com/wp-content/uploads/pdfs/Matisse-2-TS.pdf`, accessed 18.5.2020.

[71] Anthony E. Siegman. *Lasers*. University Science Books, 1990.

[72] Wouter Gins, Ruben P. de Groote, and M. L. et al. Bissell. Analysis of counting data: Development of the SATLAS Python package. *Comput. Phys. Comm.*, 222:286–294, 2018.

[73] John R. Taylor. *An introduction to error analysis*. University Science Books, 2 edition, 1997.

[74] Piyaphat Phoonthong, Michiaki Mizuno, Kohta Kido, and Nobuyasu Shiga. Determination of the absolute microwave frequency of laser-cooled $^{171}Yb^{+}$. *Applied Physics B: Lasers and Optics*, page 135, 2014.

[75] A. Münch, M. Berkler, Ch. Gerz, D. Wilsdorf, and G. Werth. Precise ground-state hyperfine splitting in ^{173}ii. *Phys. Rev. A*, 35:4147–4150, May 1987.

[76] Kischkel C. S. Maier, J. and M. Baumann. Hyperfine structure and isotope shift of some even parity levels in the YbI spectrum, 1991.

[77] I. Angeli and K.P. Marinova. Table of experimental nuclear ground state charge radii: An update. *Atomic Data and Nuclear Data Tables*, 99(1):69 – 95, 2013.

[78] S. A. Williams. Magnetic octupole moments of axially symmetric deformed nuclei. *Phys. Rev.*, 125:340–346, 1962.

[79] W.D. Phillips and H.J. Metcalf. Cooling and trapping atoms. *Scientific American*, page 50, 1987.

[80] Silverans Roger E. Van Hove, Marleen E. Fast beam collinear laser-rf double resonance. *Hyperfine Interactions*, 38:773–792, 1987.